TU Delft

DELFT UNIVERSITY OF TECHNOLOGY

MASTER THESIS

Development of an experimental method to study residual stress effects on fatigue crack growth

T. Lotz

January 2014

DEVELOPMENT OF AN EXPERIMENTAL METHOD TO STUDY RESIDUAL STRESS EFFECTS ON FATIGUE CRACK GROWTH

MASTER OF SCIENCE THESIS

For obtaining the degree of Master of Science in Aerospace Engineering
at Delft University of Technology

Tom Lotz

January 8, 2014

Faculty of Aerospace Engineering · Delft University of Technology

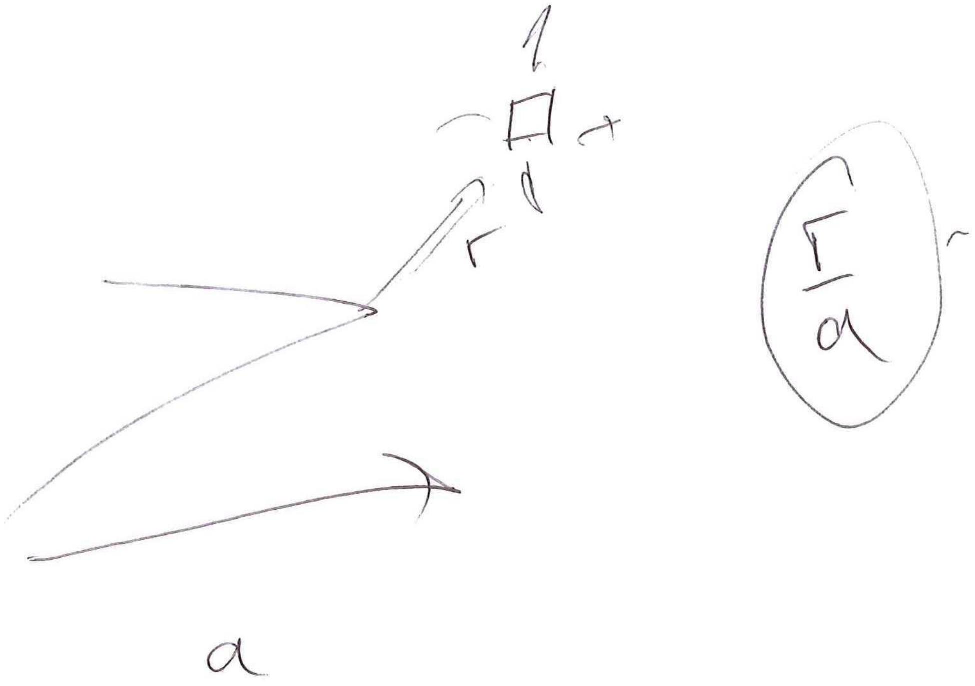
1
r
a
r
a

- plastic zone → vs residual stress.
- crack growth along grain boundaries? → how
- stress = tensor ??

10.08
10.43
35

Delft university of technology
Faculty of aerospace engineering
Department of aerospace structures and materials

Graduation committee

Dated: January 8, 2014

Prof. Dr. Ir. Rinze Benedictus
(chairman)

Dr. Marcias Martinez
(supervisor)

Dr. Ir. René Alderliesten
(supervisor)

Dr. Christos Kassapoglou

Abstract

In the aircraft industry residual stresses have been utilized for long time to increase the fatigue performance of structural elements by cold hole expansion and shot peening. Next to these intentional stresses, residual stresses are also present in the structure as a result of the manufacturing process and aircraft assembly. It is well-known that tensile residual stresses decrease fatigue life, while on the other hand compressive residual stresses increase fatigue life. Despite of this, the aerospace industry still does not give credit to residual stress as a design parameter, mainly because of the poor correlation between experimental and predicted crack growth rates. It is believed that this is mainly due to confounding factors like heat affected zones in welding, two-dimensional crack fronts, sub-surface initiation, multiple cracking and an inaccurate residual stress estimation in the experiments. Therefore, the research objective of this thesis is to:

> **Develop a methodology to introduce a well-known and consistent residual stress field in a laboratory coupon such that crack growth predictions through residual stress can be validated.**

Based on a literature study, four point bending was used to introduce residual stresses into rectangular aluminum coupons. Residual stress measurements were performed on multiple coupons by the slitting method and from strain history. Both methods agreed very well in the fully elastic domain and to a lesser extent in the plastically deformed area. Additionally, the four point bending operation was mimicked by finite element (FE) methods. The residual stresses from the FE model were in good agreement with the test data.

Crack growth tests were performed in the SEN(T) configuration at different applied stress ratios. A significant increase in growth rate was found in the tensile residual stress zone, while compressive stresses retarded crack growth.
Linear elastic crack growth predictions were made by using a weight function and superpostion. The R-shift between baseline crack growth data was calculated by the Harter-T method. The predictions did follow the experimental data well at R=0.05 and R=0.7 but to a lesser extent at R=-1. In addition, a FE prediction was made based on the J-integral which yielded similar results to the LEFM predictions.

It was concluded that the employed method is an effective way to make crack growth predictions through a one directional and constant through-thickness residual stress field. More research is required to model the effect of multi directional residual stresses on crack growth. Two dimensional crack front shapes must be accounted for in such a prediction. It is believed that for this analysis the FE method will be indispensable.

Keywords: **residual stress, fatigue, slitting, finite element analysis**

Contents

Introduction

Despite the fact that metal fatigue has been studied intensively in the past six decades, still many aircraft incidents are related to fatigue issues. Recent examples are Southwest Airlines flights 2294 and 812 whose fuselages suddenly depressurized due to widespread fatigue damage. A study of 6000 case histories from the Second World War until 2002 shows that 55% of the aircraft failures have occured due to fatigue problems [1]. These problems mainly occur because of insufficient understanding of different fatigue degradation mechanisms and their interconnectivity [2]. A major component of the uncertainty in fatigue assessment is believed to be the influence of residual stresses on fatigue crack growth [3, 4, 5]. For this reason this thesis aims at generating a method to introduce well-defined residual stress fields in standardized coupons. Thereafter, crack growth tests will be performed to study the effects of residual stresses on crack growth behaviour.

In the aircraft industry there is an ever increasing demand for cost reduction in the production process and a reduction of aircraft operational costs. As consequence of this, design stresses tend to increase which together with the nature of aircraft loading (mainly in the high cycle fatigue regime) often limits aircraft components in fatigue [6]. This has lead to the development of the damage tolerance design philosophy in the 1970s which is nowadays widely adopted in the aerospace industry [7]. The damage tolerance concept is based on the fundamental assumption that initial defects will always be present in the structure. Subsequently extension of the defects into cracks is also likely to occur and will continue until a critical crack length is reached if no action is undertaken. If the inspection interval of this component is, however, shorter than the crack growth period it is argued that the affected aircraft part can be repaired before failure occurs. Consequently increasing the aviation safety level requires thorough understanding of the relevant degradation mechanisms and crack growth parameters to refine the damage tolerance concept.

To increase this understanding, the holistic structural integrity process (HOLSIP) was launched in the 1980s. This process is primarily based on the idea that all integrity degrading mechanisms of a structure must be seen as an integrated process and not merely as a sum of separate mechanisms. HOLSIP aims at predicting the remaining useful life of a structure by creating a physics based fatigue model which takes initial conditions of the structure and applied loads during service life into account. To achieve the integrated approach to structural integrity many inputs are required to provide the outputs that are needed for the calculation of useful remaining structural life time (Figure 1).

The inputs of the model can be divided into initial conditions of the structure (green boxes) and the usage and environmental condition (blue boxes). Together, the initial aircraft condition and the accumulated fatigue damage at a certain moment in time are used to determine the remaining component life (red box). The work in this thesis will be part of the green 'Initial Structural Condition' box.

The initial condition of a structure mainly depends on the structural geometry, joints, materials, initial damage, surface treatments and residual stresses. The influence of the geometrical effects like notches and thickness steps on the fatigue life are well-known [7], whereas the effect of internal stresses is less pronounced, predominantly because of historical difficulties in measuring residual stresses [3]. In addition, the effect of residual stresses on crack growth and nucleation must also be well understood from a deterministic point of view before it can be integrated into a physics based model [9].

Residual stresses are caused by internal forces that auto-equilibrate in a component or structure without the presence of any external forces or thermal gradients [10]. The internal stresses are called residual

Figure 1: The HOLSIP process flow chart [8].

because they are often a residue of inhomogeneous plastic deformation of a component [7]. Compared to external loads, residual stresses have received relatively little attention in fatigue assessments because of the historical difficulties associated with their measurement and prediction in aircraft structures [3]. Measurement of residual stresses is hampered by the fact that they leave no outward sign. Moreover, their prediction *a priori* is difficult because they are a product of almost every processing stage of manufacturing components [11] and in addition they evolve during aircraft service life.

Of importance for a fundamental explanation of residual stress effects are the different categories of residual stress that can be present in a component. Residual stresses can be categorized in three different groups with characteristic length scales [12]. Long range stresses (Type I) equilibrate over macroscopic scale which is roughly equal to the size of the structure. Type II stresses equilibrate over several grain dimensions while Type III stresses balance within a grain.

Macro (Type I) residual stresses are the most well-known and are a result of manufacturing and assembly. Due to the different manufacturing processes that occur during aircraft manufacturing and assembly residual stresses are introduced in the structure as a result of plastic deformations and misfits [13]. Production techniques like rolling, forging, welding and bending are some sources of residual stresses due to inhomogeneous plastic deformation. Moreover misfits during assembly also introduce residual stresses, although they can be completely in the elastic domain. Macro stresses are able to cause geometrical distortion of structures and are therefore the most well-known.

Type II residual stresses nearly always exist in polycrystalline materials from the misorientation between grains. The elastic properties of grains are dependent on the crystallographic direction so that grain misorientation leads to local elastic discontinuities [14] and stress fields which equilibrate over several grain dimensions. Atomic scale residual stresses (Type III) are caused by point defects, dislocations or interface thermal mismatches [12].

With respect to crack propagation usually only macro Type I stresses are seen as a contributing factor [13]. Crack growth can only occur if the material in front of the crack tip is plastically deformed; if the crack tip plastic zone is larger than the characteristic length the strains causing type II and III stresses will tend to be drowned out by the crack tip plastic strain [3]. As a result micro residual stresses are asumed to alter micro crack growth alone and thus only type I stresses are considered from a macro crack growth point of view.

Crack nucleation together with micro and macro crack growth are the fundamental principles of metal fatigue. Metal fatigue is caused by repetitive loading of a structure below the static failure strength leading to nucleation of small cracks, followed by crack growth and ultimately complete failure of the structure. The fatigue mechanism is influenced by many phenomena like stress concentrations, corrosion and fretting acting in combination of the in-flight loading conditions.

Although the impact of aforementioned is investigated thoroughly on labratory specimens and can be designed for by knock-down factors; influence of residual stress on crack growth however has mainly been studied from an experimental point of view and it is well-known that compressive stresses can increase the fatigue life by reducing crack initiation and retarding crack growth. On the contrary, tensile stresses decrease the fatigue life by promotion of crack nucleation and growth [7]. Despite of this, satisfying model-based explanations based on fracture mechanics are not satisfying [6, 9] and the industry does not give credit to life improvement due to residual stress as design parameter [15].

The approaches that have been used to quantify residual stress effects on crack growth can be classified in two main models being (1) superposition techniques and (2) the crack closure approach [4, 16]. The first is based on the principle of superposition of the crack tip stress intensity factors, which is valid provided that both bodies behave in a linear elastic fashion [17]. The second model incorporates crack closure by means of an effective stress range ΔK_{eff}. It is believed that these models have not been very succesful in correlating experimental and predicted crack growth rates through residual stresses because of several confounding factors like heat affected zones in welding, two-dimensional crack fronts, sub-surface inititation, multiple cracking and an inaccurate residual stress estimation [9].

In order to systematically investigate the residual stress effect on crack growth and ultimately come to a satisfying physical model, the residual stress distribution throughout the test specimens must be accurately known. One way to achieve this is by designing a dedicated and repeatable set-up for which residual stress fields are generated and measured. With these well-understood specimens, fatigue tests at different load levels and load ratios can be performed to systematically investigate residual stress effects on crack growth.

Many principles are available to introduce residual stresses in laboratory coupons from which mechanical and thermal methods are seen as the most practical to generate well-reproducable residual stresses [18]. Paramount in the development of reproducable residual stress coupons is the consistency of the test procedure. Bending, cold hole expansion, shot peening, laser shock peening, welding and hole yielding are the most common mechanical methods in the literature [19, 20, 11]. The key aspect in these processes is an uneven distribution of plastic deformation throughout the specimen volume.

The introduced residual stress field can subsequently be measured by comparing the specimen contours prior and after the deformation such as by digital image correlation [21], slotting [22], hole drilling [23], stress induced density variation measurements like ultrasonics [24] or by techniques which relate atomic distance directly to stresses like neutron and X-ray diffraction [25].

The different techniques can be classified as either destructive or non-destructive. In contrast to the aerospace industry where non-destructive methods are preferred to not damage an aircraft, on lab coupons both can be used. This gives rise to the use of destructive measurement methods that often require less dedicated and expensive equipment.

A literature study revealed that a consistent residual stress field is best introduced by plastic bending. Therefore in this thesis four point bending is used to generate residual stresses in rectangular coupons. Residual stress measurements are then performed by the slitting method and from strain history on mulitple coupons. Thereafter, crack growth tests are performed trough tensile and compressive residual stress to generate experimental data and superposition will be used to make crack growth predictions. Additionally, the four point bending operation is mimicked by finite element (FE) analysis. Residual stress effects on crack growth will be predicted with this model and validated against test results. In the end, this will show that superposition is an effective means of accounting for residual stress in predictions. FE analysis is at least as accurate as classical weight function solutions and more versatile.

Chapter 2 explores the origin and different types of residual stress and reviews what work has been done on the influence of residual stress on fatigue crack growth. Chapter 3 reviews different measurement techniques and methods to introduce residual stress in laboratory coupons. At the end of this chapter the best options are selected by a trade off. Chapter 4 provides a detailed description of the experimental test that are carried out, while Chapter 5 reports the test results. The results are analysed and discussed in Chapter 6 and conclusions can be found in Chapter 7. Finally, recommendations on the used procedure together with proposed future work is given in Chapter 8.

Chapter 2

Residual stress effects on fatigue crack growth

To model the residual stress effects on crack growth fundamental understanding is needed about the behaviour of cracks through residual stress fields. Therefore this chapter first introduces residual stress and its nature in Sections 2.1 and 2.2. The phenomena of crack initiation, crack growth and fracture parameters K and J are introduced in Section 2.3. Thereafter a literature review on residual stress effects on crack growth is presented in Section 2.4. Based on this review Section 2.5 derives the research objective on which the experimental procedure will be based.

2.1 What are residual stresses?

Residual stresses are caused by internal forces that auto-equilibrate in a component or structure without the presence of any external forces or thermal gradients. The background of the terminology residual stress is that a residual stress distribution in a material is often left as a residue of inhomogeneous plastic deformation [7]. When combined with external loading, the residual stresses may lower or increase the resulting internal stresses in a structure. Residual stresses are often regarded as a negative effect during prodution since out of plane deflections (warpage) can be a result of residual stresses. From a fatigue point of view they can be an effective tool to increase the performance of structures.

The most well-known applications of residual stress are reinforced concrete and pretensioned bolts. The former makes use of the excellent tenslile properties of steel by tensioning the steel rods which consequently loads the concrete in compression. The latter results into a smaller tensile stress range in the bolt with an increased fatigue performance as a result.

The name residual is subjective and dependent on the standpoint of the observer. If for example two riveted plates are seen as one structure, the rivet forces within the structure are internal and can be categorized as residual. If however one plate is considered solely the rivet forces can be treated as external and therefore do not contribute to the residual stress field.

Regardless of the point of view, external forces and residual forces may be summed up to obtain the final internal stress state in a structure. Yielding (either tensile or compressive) is therefore reached earlier as external forces are increased. The maximum applied forces on structures can therefore be limited if plastic deformation is prohibited.

In the meatime, the ultimate properties are only affected to a limited extent. If inhomogeneous residual stress is superimposed with an external loading, areas with maximum residual stress will yield first. This yielding leads to a more uniform distribution of stress throughout the structure. When the yield stress is exceeded througout the complete cross section, the nearly homogeneous stress distribution (number 5 in figure 2.1) is obtained. Just before failure the stress distribution is almost homogeneous and the strength of the material will not be affected by the original residual stress distribution [7].

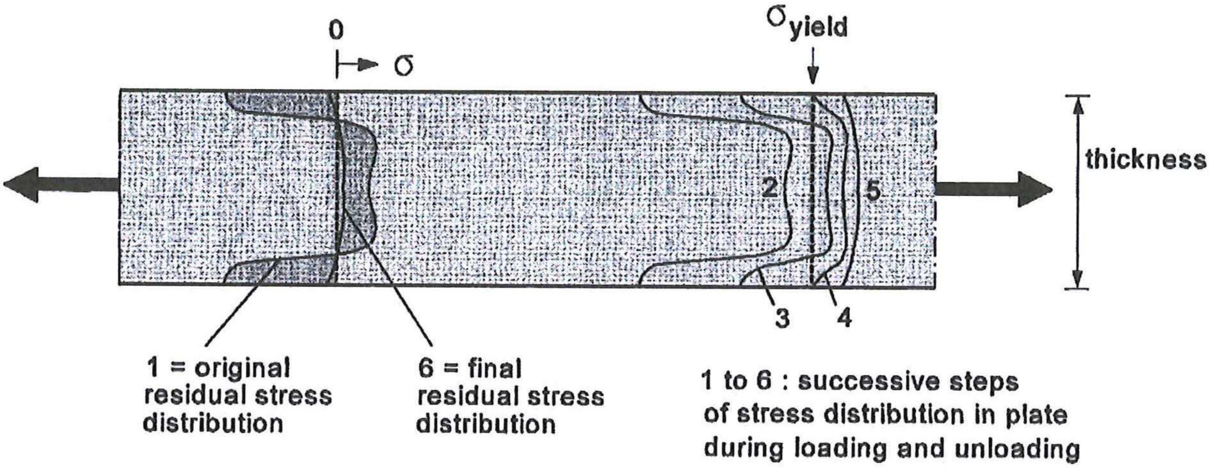

Figure 2.1: Residual stress redistribution due to in-plane stretching [7].

In contrast to the ultimate properties the fatigue behaviour of metals is influenced by residual stresses considerably. Fatigue crack nucleation is a function of the applied stress range so residual stresses do not have a large influence on crack nucleation. However, if small cracks are present in a structure, compressive residual stress can slow down micro crack growth or can even force cracks to arrest, leading to a significant increase in fatigue life. Tensile stresses are known to promote crack growth by loading the crack faces in positive mode I opening direction and thereby reduce the fatigue life of a structure.

2.2 Types and origins of residual stresses

Residual stress in a material are a result of Eigenstrains [26] and can be categorized in three different scales with different origins [12]. The origins and properties of the different types of residual stress are discussed in this section.

2.2.1 Eigenstrains

Eigenstrain was defined by Mura [26] as the non-elastic strain which is not caused by externally applied loads but by initial strains, plastic strains, phase transformations, thermal loading or misfits. Eigenstrains are uneven distributed strains within a body that cannot satisfy internal compatibility and create eigenstresses in the body, which are in the engineering world called residual stresses [26].
A real life example of initial strains are stretched steel bars in reinforced concrete; here the incompatibility between the prestrained bars and the unstrained concrete gives rise to residual stresses. Similarly, by plastic expanding a hole in a sheet, the elongated hole egde does not match with the original surrounding material and (compressive) residual stresses are created around the hole because of the elastically constraining surroundings.

If the Eigenstrain distribution throughout a certain structure is known the complete 3D residual stress field can be calculated [26]. Eshelby [27] developed a general formulation which describes the residual stress arising from the inclusion of misfitting particles in a material. This concept integrates the stress field distribution of infinitesimal point sources to obtain the full stress field. With this still being an analytical solution, more complicated Eigenstrain distributions cannot be solved analytically any more. The ongoing increase in computing power is enabling researchers to solve residual stress fields from more complicated Eigenstrain distributions by finite elements analysis. One of the tricks that can be used to insert an Eigenstrain distribution in a model is to assign a fictious thermal gradient over a volume. Lately, attempts are even made to model the polycrystalline behaviour of metals by means of an Eigenstrain approach [28]. This can be of interest to better understand the effect of micro residual stress on micro crack growth.

2.2.2 Macro residual stresses

Macro (type I) residual stresses are continuum level stresses that equilibrate over component or structural dimensions. These so called macro residual stresses neglect the microstructure of the material in where completely different stress states can be present (see section 2.2.3). Since macro residual stresses equilibrate over complete part dimensions they can lead to part deformations during production. This makes these Type I residual stresses most often undesirable.

Macro stresses are caused by inhomogeneous plastic deformations, misfits in the structure, chemically treated surfaces or thermally loaded structures. Plasticity induced residual stresses in aircrafts are often a residue of bending and rolling operations during part production. Misfit stresses can either be introduced on purpose by presfitting rivets or can be an unwanted result of tolerances during production and manufacturing. Chemical surface treatments like nitriding dope the outer material with atoms which increases the volume of the outer layers. As a result, compressive stresses are created in the surface layers and tensile stresses in the core material. However, it is important to note that macro residual stress can be removed from products by annealing or by homogeneous in plane stretching.

2.2.3 Micro residual stresses

Residual stresses which equilibrate over several grain dimensions (Type II) or less (Type III) are called micro stresses [12]. In contrast to macro stresses which are often caused by externally applied deformations, these stresses are often captured in the bulk material because of the heterogeneous build-up of crystalline metals.

Metals are build up from atoms which are packed together in repetitive formations. Materials with such an orientation are called crystalline. This phenomenon is a result of the solidification process after melting the ore to produce metal or after alloying processes [14]. At the beginning of metal solidification small solid nuclei grow inside the liquid with a random crystal orientation. When these nuclei grow further, areas with different orientation and size grow against each other and grains are formed. Upon completion of solidification the grains maintain their relative misorientations and since the elastic properties of grains are heterogeneous, elastic mismatches are stored in the material during fabrication. These mismatches and the presence of grain boundaries give rise to Type II residual stresses. Type III stresses arise from line defects (dislocations), point defects such as from radiation damage or doping with atoms of a different size [3]. These small stresses can give rise to larger scale stresses from their cumulative presence in a material. For example the doping of a glass surface with one K atom creates a type III microstress, but multiple ion exchange using molten salt baths introduces many atoms into the near surface region leading to substantial long-range Type I stresses [3].

Some residual stress measurements such as X-ray diffraction measure very small sampling areas typically close to a single grain size [29]. In these cases one must be sure that not Type II stresses are measured if bulk stresses are required.

2.3 Fatigue crack initation and crack growth

The fatigue life of a component or structure is the time between first crack initation and final fracture of the material as result of a crack surpassing the critical crack length. The crack initiation phase and the subsequent crack growth are fundamentally different phenomena. Therefore life prediction often differentiates between these two phases. The following section discusses crack initiation and growth and their life time prediction models. Additionally, the fracture parameters on which most of these models and founded are briefly described.

2.3.1 Crack initiation

Crack inititiation is the formation of micro cracks in a metallic structure which is repeatedly loaded and unloaded. The process is a result of atoms sliding relative to each other over the slip bands which are driven by a shear force. When a material is loaded, the macro shear stresses can be constant over an area while the micro shear stresses can vary over different grains because of local elastic anisotropy. Some grains will be positioned in such a way that slip will occur more easily than at other grains, so that crack initiation will begin at those favourable positions. Crack nucleation is also most likely to occur at free surfaces, since here the material is not constrained on one side. As load is introduced and slip occurs, a new surface will be exposed to the environment (Figure 2.2a) and oxidates immediately [7].

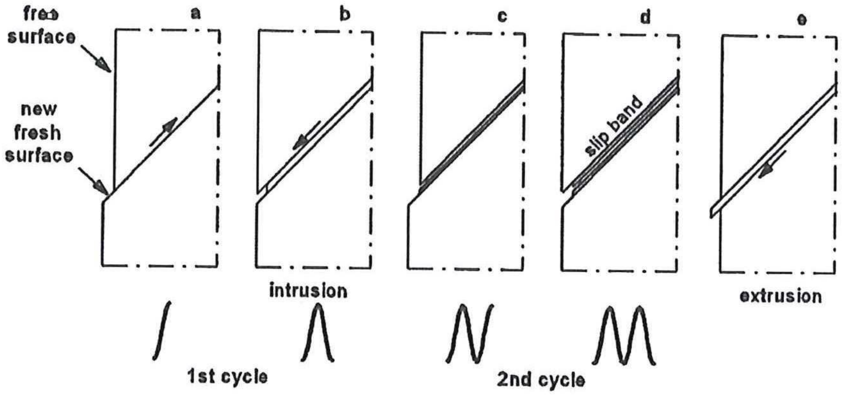

Figure 2.2: Cyclic loading leading to slip bands [7].

This oxide layer, together with an amount of strain hardening at the slip band, leads to an increased shear force in the other direction with reversed slip as consequence (b). If now the loading pattern is repetitive, cyclic slip can occur with several inclusions next to each other (d) which is actually a micro crack, which can grow to a macro crack. Crack initation is thus strongly dependent on the surface conditions like roughness and corrosion.

After the crack has grown through several grains the crack growth rate becomes more stable and dependent on bulk material properties. Crack growth is now considered to be independent of surface conditions. This moment is often regarded as the transition from crack initiation to crack growth [7]. Further growth is now solely dependent on the bulk material properties.

2.3.2 Crack initiation predictions

The fracture mechanics behind micro crack growth are believed to be well understood as indicated in the previous section. To predict the behaviour of this failure mechanism from a fracture mechanics point of view is, however, much more complicated due to the unpredictable nature of surface quality, material scatter etc.

Fatigue crack initiation predictions are therefore done in an empirical way. By analyzing crack growth results of specimen with known geometry, crack initiation times can be obtained for a specimen of a certain material, surface quality, chemical treatment and so forth. If now the data is obtained for many tests at many different stress levels, SN-curves can be drawn which relate the cyclic stress amplitude to the number of load cycles at which fatigue cracks initiate.

2.3.3 Crack growth

The phenomenon of interatomic slip is a result of cyclic shear stress and the growth direction is therefore parallel to the shear direction. If the crack is growing into the material through more grains, the slip will be more constrained due to the presence of neighbouring grains oriented differently and the macro crack will grow further perpendicular to the main tensile loading direction.

In continoum solids the stresses around notches are calculated by using stress concentrations. It could be argued that for sharp cracks a similar principle can be used to determine the stress state around the crack tip, which is in essence a very sharp notch. By looking at the crack tip which is 'infinitely' sharp, the stress concentration principle would then predict infinite stresses in front of the crack tip. Clearly, this concept is not applicable for cracks.

In the literature different concepts are used as 'loading severity' parameter which are the stress intensity factor [7], the strain energy release rate [30] and the Rice integral [31]. The first two concepts are linear elastic concepts which are equivalent because they are related to each other via the material stiffness. While the former is most often used for simple tensile tests on metal specimens the latter is more practical in situations where anisotropy or bonded structures are tested [32]. Since this thesis focusses on relatively simple metal specimens the stress intensity concept will be more practical than the energy release rate.

The J-integral method is a concept which calculates the energy release rate of a cracked body by integrating the dislocation density around a crack tip [33]. The J-integral is difficult to solve analytically and is therefore most often calculated by means of FE methods. The K and J concepts are reviewed briefly in the following sections.

2.3.3.1 The stress intensity factor K

The stress intensity factor K was introducted by Irwin [34] and is an indication of stress intensity around a crack tip. The general equation for K in a flat plate is

$$K = \beta S \sqrt{\pi a} \tag{2.1}$$

in where β is a dimensionless geometry factor, S is the far field stress and a is the crack length. Equation 2.1 states that the stress intensity factor is linearly related to the applied far field loading such that the applied stress ratio equals the K ratio

$$R = \frac{S_{min}}{S_{max}} = \frac{K_{min}}{K_{max}} \tag{2.2}$$

and the stress intensity range becomes

$$\Delta K = \beta \Delta S \sqrt{\pi a} \tag{2.3}$$

This concept is illustrated in Figure 2.3

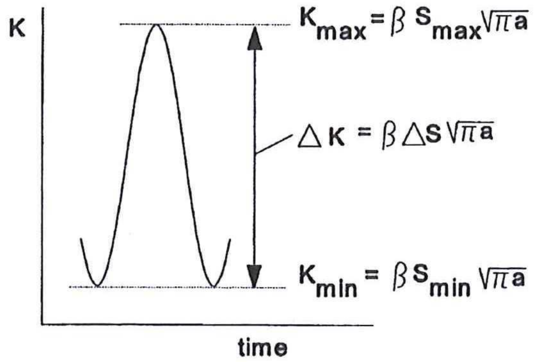

Figure 2.3: The stress intensity as a function of time during one load cycle [7].

The stresses around the crack tip can be uniquely described as function of the stress intensity factor by equation 2.4

$$\sigma_{i,j} = \frac{K}{\sqrt{2\pi r}} f_{i,j}(\theta) \tag{2.4}$$

with the coordinate system as shown in Figure 2.4. These equations are derived using elastic stress field equations for a stressed element near the tip of a sharp crack in an infinite body.

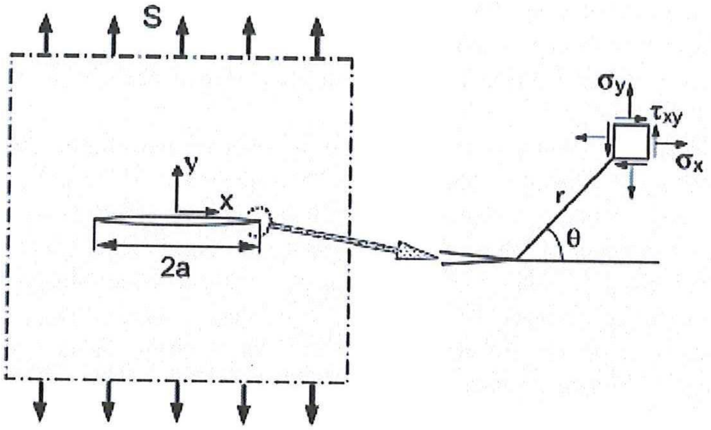

Figure 2.4: Definition of coordinates for an opening crack mode [7].

This single set of equations implies that the stress fields around different cracks are similar in shape. The occurance of the crack tip distance r in the denominator of the equations would predict singularity at the absolute crack tip. In reality the stesses at the crack tip are relieved by plastic deformation so that infinite stresses at the crack tip do not occur. Although the stress intensity is a linear elastic concept crack tip plasticity does not contravene the limits of validity, the reason for this is the small scale yielding (SSY) criterion. Small scale yielding is assumed true when the plastic zone in front of the crack tip is much smaller (typically 10 times [32]) than the K-dominated field. This K-dominated field is the area -about half the crack size- in which the elastic strains are higher than the nominal strains in the specimen or structure, see Figure 2.5. If the plastic field is much smaller than the K-dominated field it will hardly influence the stress state at the boundary of the K-field and thus the stress distribution around the crack tip. This makes the stress intensity factor a valid linear elastic concept.

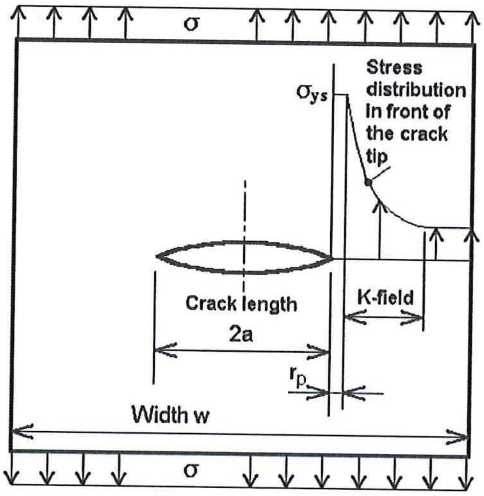

Figure 2.5: Stress distribution in front of a crack. K-field is the elastic region with elevated stresses [32].

2.3.3.2 Similitude

If two cracked specimens or structural parts of the same material and thickness are loaded in such a way that K is equal, the K-dominated fields will also be identical (Equation 2.4). This implies that the same stresses are present around the crack tip, which results into similar plastic deformation and crack extention. This leads to an equal amount of crack growth in both structures although loading conditions can be completely different. This so called similitude approach can be used to relate labratory specimen crack growth data to crack growth predictions in real structures [7].

2.3.3.3 Thickness effect

The similitude concept can be used if the conditions for crack growth in the lab specimens and real structures are similar. It turned out, however, that the stress state in thin and thick specimens do not correlate if the same stress intensity factor is applied [35]. The underlying principle of this difference is the plane-strain state of the thick specimens, while the thin specimens are in plane stress. In these thin specimens it is assumed that in-thickness contraction is not constrained such that the thickness direction is stress free. Under plane-strain conditions, contraction in the thickess direction is prevented by the surrounding material so that through tickness stresses develop. Together with the tensile in-plane stresses, through-the-thickness stresses create hydrostatic stresses. Hydrostatic stresses increase the yield strength of a material such that the plastic deformation in the core of a tensile loaded specimen are smaller, compared to these at the free surfaces.

In thin specimens the contraction in thickness direction as a result of the poisson effect is possible over (almost) the complete thickness so that no stresses are present in z-direction. This effect makes it possible for the crack tip material to yield to a greater extent. It can be concluded that different plastic zone sizes are present between specimens of different thickness. The similitude concept thus cannot be applied between a specimen in plane-strain and a specimen in plane-stress or vice versa.

Next to the plastic zone, also the crack front can have different shapes under plane-stress or plane-strain which invalidates the similitude concept. Whereas under plane-stress the crack front is usually straight, plane-strain conditions will often show curved crack fronts. Futhermore, shear lips can be formed on the crack surface by plastic shear deformation [7]. As a conclusion, the similitude concept must be preferably applied to specimens and structures with equal thickness.

2.3.3.4 The J-integral

The J-integral is a fracture parameter which represents the energy release rate of non-linear elastic cracked bodies [33]. The energy release rate is defined as the decrease of potential energy per unit area of crack extension. The J-integral can be expressed as [36]

$$J = \int_{\Gamma} (W dy - T \frac{\delta u}{\delta x} ds) \tag{2.5}$$

Here Γ is a curve surrounding the crack tip, $T = \sigma_{ij} n_j$ is the traction vector defined according to the outward normal along Γ, u is the displacement vector and ds is an element of arc length along Γ.

The J-integral is proven to be path independent for residual-stress-fre bodies so that every chosen contour gives the same J-integral. If residual stresses are present in a body, the J-integral shows different values for different paths chosen. Path independency can be obtained by treating the residual stresses as initial strains [31, 37].

2.3.4 Crack growth predictions

Predicting the crack growth rates is an important part of damage tolerance calculations. If crack growth can be predicted accurately aircraft inspection intervals can be such that aircraft failure due to fatigue issues are minimized. This section discusses some of the most used crack propagation equations that are used.

If cracked bodies are subjected to an external loading the stress intensity factor determines the whole stress field around the crack tip (section 2.3.3.1). If the same K_{min} and K_{max} are applied to different specimen the same stress, strain and thus fatigue process should then happen at the crack tips in both specimens. Therefore it was reasoned by Paris [38] in 1963 that a function of K should control the rate of crack extension. The calculated stress intensity factors for multiple test configurations were plotted against the crack growth rate. From these plots an emperical relation was proposed which is now known as the Paris relation

$$\frac{da}{dN} = C\Delta K^m \tag{2.6}$$

with C and m as material constants. This relation predicts a log-log linear relation between crack growth rates and the stress intensity range, see region II in Figure 2.6.

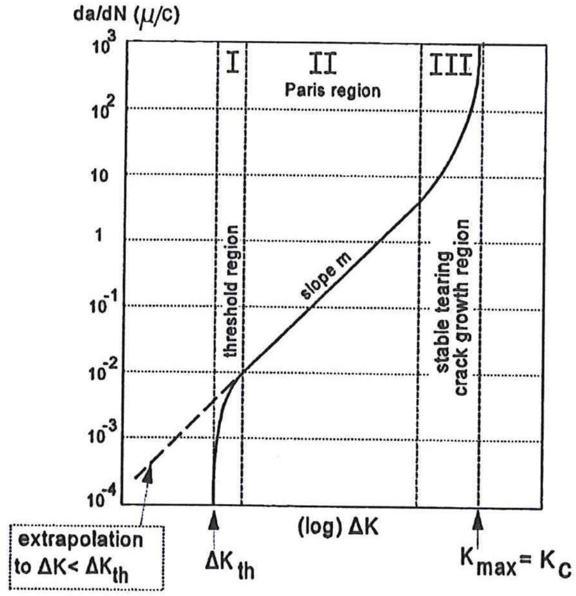

Figure 2.6: Crack growth rates as a function of ΔK showing the threshold (I), Paris region (II) and stable-tearing region (III) [7].

This equation however does not account for the lower left and upper right asymptotes and also the R effect is not included. The lower left asymptote is known as the fatigue threshold under which an existing crack does not grow any further. This ΔK_{th} is believed to be dependent on the load ratio R and decreases for higher R. This statement however contradicts results from fatigue crack growth tests in vacuum, where the ΔK_{th} was found to be R independent.
When the critical K_C at the right side of Figure 2.6 is reached the material starts to fracture.

A few years later, to account for the oversimplicity of the Paris equation regarding the stable tearing limit, Forman [39] proposed the following equation

$$\frac{da}{dN} = \frac{C\Delta K^m}{(1-R)K_c - \Delta K} \tag{2.7}$$

in where K_c is the maximum K before fracture occurs. This equation accounts for the R-effect and also the upper asymptote is taken into account. This equation however does not account for the lower asymptote.

Both the lower and upper asymptote and the Paris region are incorporated in the NASGRO [40] model which is widely used nowadays

$$\frac{da}{dN} = C\left[\frac{1-f}{1-R}\Delta K\right]^n \frac{\left(1-\frac{\Delta K_{th}}{\Delta K}\right)^p}{\left(1-\frac{K_{max}}{K_{crit}}\right)^q} \tag{2.8}$$

where C, n, p and q are emperically derived and f is K_{op}/K_{max} which is described by fit functions for different ranges of R.

As an alternative to this, the effective stress intensity range, ΔK_{eff} can be used. During fatigue tests on aluminum sheet material Elber [41] found that fatigue cracks were already closed during unloading before the tensile load was back to zero. This closure effect was attributed to crack tip plasticity in the wake of the crack tip. If a cracked body is loaded in tension, the material in front of the crack tip elongates plastically. Therefore, after crack extension the elongated crack surfaces make contact during unloading at a certain positive stress level S_{op}. Consequently the crack is only opened during a part of the load cycle. Elber stated that crack growth will only occur during the open part of the load cycle and proposed an effective stress range S_{eff} as

$$\Delta S_{eff} = S_{max} - S_{op} \tag{2.9}$$

and the ratio of effective stress range U as

$$U = \frac{\Delta S_{eff}}{\Delta S} \tag{2.10}$$

which represents the percentage of the applied load range during which the crack tip is open. The crack growth rate is then predicted by using a relation of the form

$$\frac{da}{dN} = f(\Delta K_{eff}) \tag{2.11}$$

in where the function f is the closure-free crack growth ralation for the material of interest. This relation is found by performing crack growth test at high loads and high stress ratio. At high R-ratios (>0.7) crack growth is often regarded as closure 'free'. The effective stress range U is dependent on the stress ratio. Based on crack growth tests, several emperical equations have been proposed that relate U to R (e.g. by Schijve [42] and Newman [43]).

2.3.4.1 Effect of plastic prestraining

As stated before, in this work the residual stresses are introduced in the coupons by plastic deformation of the outer fibers. Tensile plastic prestraining increases the material yield stress and thereby affects the crack growth rate through the coupons. It can be expected that the misfit between the crack tip plastic zone size and the surrounding material will be smaller, thus producing less crack face closure. On the contrary, compressive plastic prestraining decreases the tensile yield stress which would increase the crack tip plastic zone size and subsequently retard crack growth.

Kang [44] observed an increase of crack growth rate by a factor 2 in tensile prestrained aluminum 2024 plates. Schijve [45] later repeated the experiments by Kang and found the same results. He attributed the increase in growth rate to a reduced plastic zone which decreased the crack opening stress. Furthermore, the plastic zone size ahead of the crack tip was smaller because of the increased yield strength of the material which led to higher stresses in front of the crack tip.

In contrast to these results, Rubaie et al. [46] recently concluded that tensile prestraining of Al-7475 has no effect on crack growth in the Paris region. However, fatigue tests on R=0.5 were conducted; crack closure effects were thus probably not taken into account because of the relative high load ratio. No data is found in the literature on the effect of compressive prestraining on crack growth.

2.4 Residual stress effects on crack growth

It is well-known that residual stresses affect macro crack growth by either promoting or retarding the growth, depending on the residual stress state (e.g. [17], [6], [3]). Many experiments have been carried out where crack growth was measured in specimens containing residual stresses (e.g. [47], [48]). Crack growth relations such as the Paris equation were then adjusted to the test results by parameter fitting. These investigations are proven to be useful for the tested configuration, but are limited to this configuration only.

Many researchers have tried to model residual stress effects by using superposition [49, 9]; crack closure predictions have been done by means of a modified Dugdale strip model [50] or Finite Element analysis [51]. A literature study is given in this section.

2.4.1 Modeling residual stress effects by superposition

A general applied method throughout the literature is the superpostion principle [52, 17, 16, 53, 54]. In this section the theoretical background is briefly discussed first, whereafter the use of superpostion in the literature is reviewed.

2.4.1.1 Theory

Bueckner [55] was the first to recognize that the stress intensity factor for a crack inserted in such a linear elastic body can be computed from the internal stresses in the uncracked body along the crack line. Later it was shown that this principle is also valid for bodies containing residual stresses [56]. Therefore the residual stress intensity factor K_{res} may be calculated by applying the residual stress distribution in the uncracked body as crack face pressures as shown in Figure 2.7

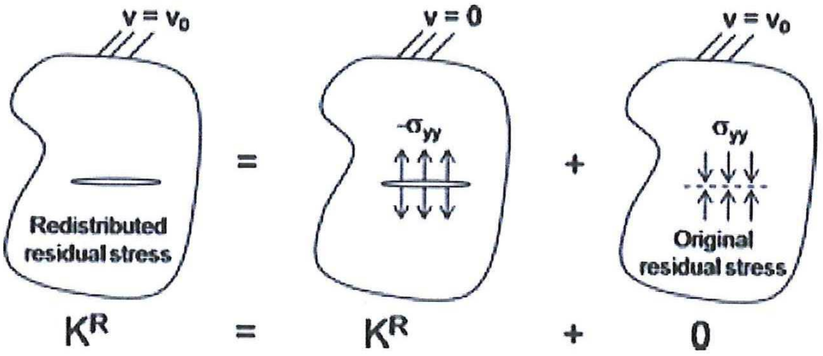

Figure 2.7: Principles of the superposition method to calculate K_{res} from crack face pressure in the unloaded body [49].

This linear elastic approach employs a weight function to obtain the residual stress induced intensity factor K_{res} from the uncracked residual stress distribution. For a particular crack geometry and loading system 'A', a weight function $m(x,a)$ (available for many geometries in [57]) may be defined as

$$m(x,a) = \frac{H}{2K_I^A}\frac{\partial v(x,a)}{\partial a} \tag{2.12}$$

where H is the modulus of elasticity, K_I^A is the stress intensity factor and v is the crack surface displacement. Using this weight function, the stress intensity factor at crack length a from residual stresses in the same geometry for any other loading system can be calculated by solving

$$K_{res} = \int p(x)m(x,a)(x)dx \tag{2.13}$$

where $p(x)$ is the residual stress crack-line loading. The obtained K_{res} is now superimposed on the applied stress intensity factor K_{app} such that K_{total} and R_{total} can be inserted in one of the crack growth equations in Section 2.3.4.

A little used property, noted by Rice [58] is that once Equation 2.13 has been solved for K_I^B, this solution can be inserted back into Equation 2.12 to reconstruct the crack surface displacements. Care must be taken to not slavishly apply this feature since it can produce negative crack surface displacements which does not make sense. Parker [17] noted that this problem can be solved by using an iterative scheme in where crack face pressures are applied at the overlapping portion of the crack faces.

2.4.1.2 Literature

In general, two variants of the superposition principle have been used most often. The first and most simplistic is called the *superposition method* where K_{res} is added to the maximum and minimum applied intensity factors $K_{app-max}$ and $K_{app-min}$:

$$\Delta K = K_{tot-max} - K_{tot-min} = (K_{app-max} + K_{res}) - (K_{app-min} + K_{res}) = \Delta K_{app} \tag{2.14}$$

which shows that the stress range is not affected by residual stresses. By acknowledging that

$$R_{tot} = \frac{K_{tot-min}}{K_{tot-max}} = \frac{K_{app-min} + K_{res}}{K_{app-max} + K_{res}} \neq R_{app} \tag{2.15}$$

it can be seen that the stress ratio R does vary with residual stress, see Figure 2.8a.

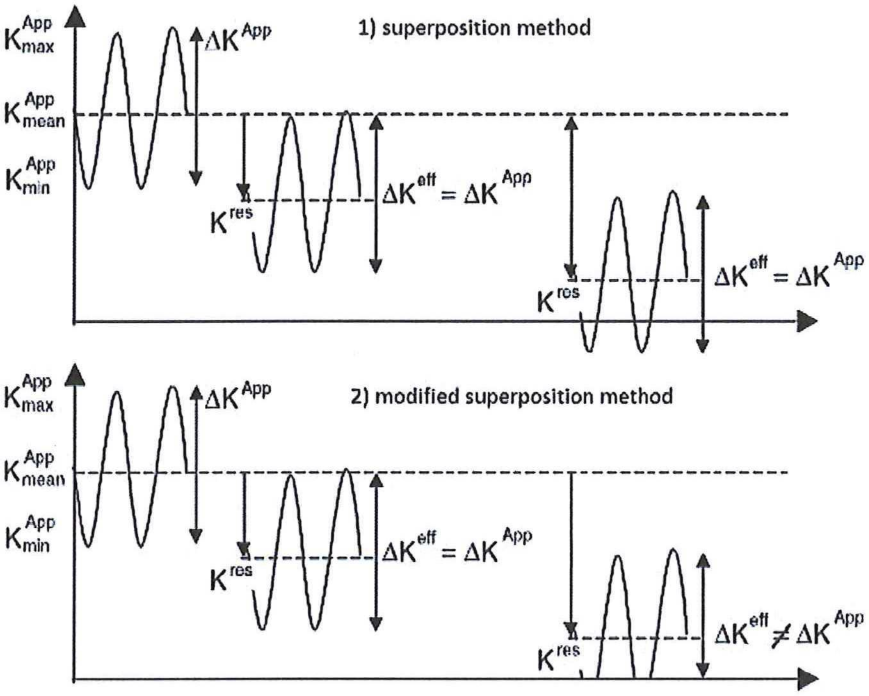

Figure 2.8: A schematic of the *superposition method* and the *modified superposition method.*

The second approach is called the *modified superposition method* (Figure 2.8b) and is similar to the first method but omits the compressive part ($K_{tot-min}$<0) of the load cycle by setting $K_{tot-min}$=0 such that $\Delta K = K_{app-max} + K_{res}$ and consequently $R = 0$ for all negative stress ratios [17, 54]. This means that every negative load ratio is set to zero and crack growth retardation or promotion is fully attributed to ΔK-effects.

This would, however, imply that for all negative R-ratios, crack growth rates are equal to the rate at R=0. By plotting K-max versus delta K, Jones [59] concluded that this tempting concept (only R=0 data is required for all negative load ratios) is oversimplified and produces non-conservative predictions.

The applicability of superposition has been studied by Stuart et al. [9] on one-dimensional cracks in cold-expanded open holes under constant amplitude loading. Long dogbone coupons made of 2.03mm thick 7075-T6 sheets were cold-expanded up to 3% with a final hole diameter of 7mm. Center crack tension tests were performed from the centrally located hole.

Care was taken to accurately control the test set-up to ensure one-dimensional crack growth, determine residual stress variability, measure crack growth and calculate stress intensity factors to eliminate side-effects. Contour measurements showed a variability of 10% in residual stress between similarly prepared coupons.

Crack growth predictions were done by using Newman's opening stress function with plane-stress/plane-strain factor 2 and $S_{max}/S_o = 0.3$. This latter is a simplification for residual stress bearing material, since a clear S_{max} is not available here. Baseline crack growth data ($\frac{da}{dN}$ vs ΔK) was collapsed into $\frac{da}{dN}$ vs ΔK_{eff} by

$$\Delta K_{eff} = \Delta K \left(\frac{1 - S_o/S_{max}}{1 - R} \right) \tag{2.16}$$

For coupons without residual stress, the LEFM predictions compared very well to the experimental results at R=0.1 and R=0.5, having a maximum error in lifetime of 2.5%. For residual stress bearing coupons tested at R=0.1, LEFM predicted 74,000 cycles while test results varied between 29,000 and 160,000 with an average lifetime of 86,000 cycles. At R=0.5 the LEFM prediction was 223,000 cycles, while test lifes ranged from 128,000 to 261,000 cycles with an average of 192,000.

The variations in lifetime were attributed to variations in residual stress; at R=0.1 a 10% variation in K_{res} gave prediction bounds of 36,000 and 163,000, which is in agreement with the experimental scatter. Concluded was that LEFM with superposition is an effective model for predicting fatigue crack growth in cold-expanded coupons under CA loading.

The same conclusion was drawn by Ghidini and Donne [60] who used *superposition* to predict crack growth on overloaded compact tension specimens made from 2024-T3 and 7475-T7351. The overload resulted into high compressive stresses at the starter notch tip and tensile stresses further inwards.

The AFGROW code was employed to run the predictions. Residual stresses were measured by means of slitting and the obtained σ_{res} distribution (although slightly modified to correct for predictions above the material yield stress) served as input for the model.

The fatigue tests were conducted at constant applied ΔK at R=0.6, for which the applied forces were constantly reduced. Although residual stresses became tensile at large crack lengths, the residual stress intensity factor kept subzero for the complete crack length range. The predicted crack growth rates correlated well to the experimental data for both 2024 and 7475 aluminum specimens.

Jones and Dunn used the *superposition principle* and the *modified superposition principle* to predict crack growth through plastically bent beams [49] and pre-yielded holes [61].

Aluminum 2024-T351 beams were 4-point-bent up to an outer fiber strain of 1,1%. The residual stress distribution was obtained from the strain history during the test and verified by slitting measurements (Figure 2.9 a). The stress intensities from the applied loading and the residual stresses were calculated with the ABAQUS J-integral method and were input to a LabVIEW script to apply a constant $\Delta K = 10 Mpa\sqrt{m}$ and R=0.1. Because crack growth was initiated at the compressive side of the coupon, the applied loading was high and a constant amplitude loading would have lead to large scale yielding at large crack lengths.

The ABAQUS model showed that at the transition from compressive into tensile residual stress remote crack closure could be expected. Therefore, for cracks in this region, K_{min} was calculated with the J-integral and the *superposition method* was updated with these K-results. This method was named the *superposition contact method.* Crack growth was predicted by interpolation between baseline crack growth data with the Harter-T method. Results of the three prediction methods and the experimental results can be found in Figure 2.9 b.

It can be seen that the crack growth rate was almost constant for the coupons without residual stress (square data points), as expected. The *superposition* method (dashed line) overpredicted growth rates throughout, while the *modified superposition method* underpredicted crack growth rates. This proved that

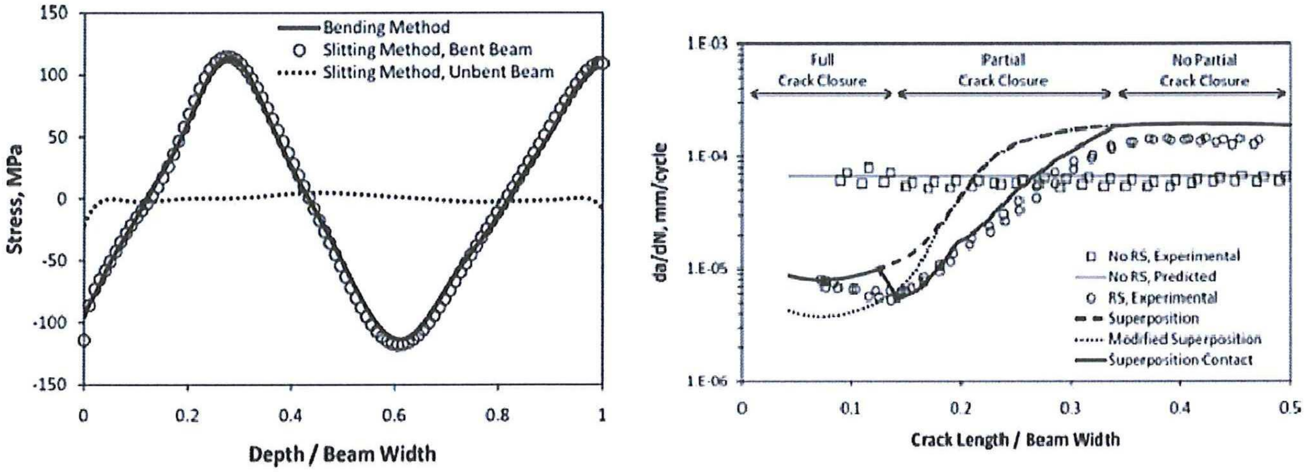

Figure 2.9: Residual stresses from strain history (called 'Bending method') and slitting (left). Predicted and measured crack growth rates through an initially compressive (a/w <0.1) and tensile (0.1 <a/w<0.45) residual stress field (right) [49].

the often applied assumption that R=0 for negative K_{min} is not accurate, as also reported in [62, 63]. The best predictions were obtained from the *superposition contact method* (solid line) and showed that partial crack closure correction can effectively be made by FEM calculations.

Similar conclusions were drawn from predictions on pre-yielded holes [61]. Here finite element predictions were employed to calculate the residual stresses from pre-yielded center-hole sheets. Superposition overpredicted the crack growth rate at the transition from compressive to tensile residual stress. The contact correction showed good correlation to the experimental data.

A slightly different approach was chosen by Itoh et al. [64]. Rectangular steel center-crack-coupons with a longitudinal weld were subjected to constant load fatigue tests at various stress ratios. In addition, residual stress free coupons were subjected to equal loadings. For all coupons the crack opening load was determined at various crack lengths by means of strain gauges bonded at the crack edge (no partial crack closure was observed). From this data, a single curve was fitted that related the crack opening ratio U against total stress ratio R_r, as depicted in Figure 2.10.

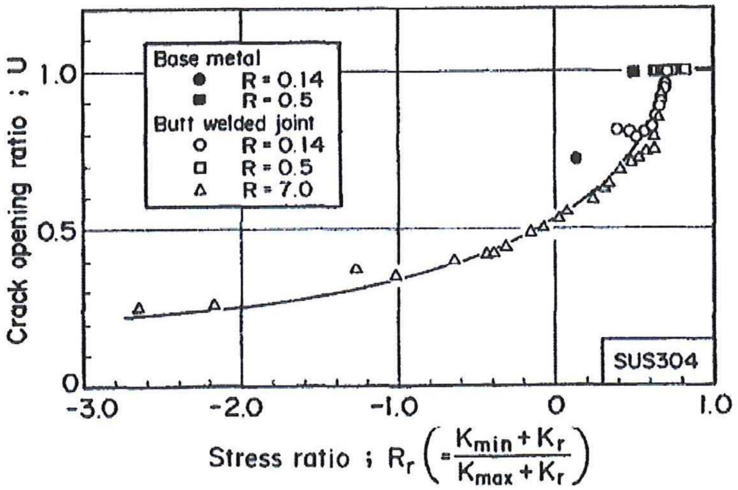

Figure 2.10: Effect of stress ratios on crack opening ratios [64].

Residual stresses were measured by slitting, from which K_{res} was found by FE analysis. This K_{res} was thereafter added to both K_{max} and K_{min} to obtain the total stress ratio R_r. Crack growth prediction through the residual stress field was now done by first calculating R_r, then finding the opening stress from the curve in Figure 2.10 and calculate K_{eff} with this data and finally relate K_{eff} to $\frac{da}{dN}$ using effective crack growth data.

Since all crack growth test were performed with center-crack-specimens test initially grew in a tensile stress field switching to compressive at about 20mm crack length. Crack growth predictions were good, showing a decreasing $\frac{da}{dN}$ versus ΔK curve as the crack approaches the compressive stresses. Concluded was that this concept of using crack opening loads and ΔK_{eff} is an effective way to predict growth through residual stresses. This conclusion is similar to that drawn by Jones and Dunn [49], Beghini and Bertini [54] and Nelson [16].

2.4.1.3 Criticism

The use of superposition has been criticized by some researchers because it considers only the initial residual stress field that exists in the uncracked structure, with no acknowledgement of the redistribution of residual stress that occurs as the propagating fatigue crack penetrates the residual stress field with its free or partially free surfaces [53, 48]. Here it was argued that the superpostion principle seems correct for shallow cracks relative to the sample dimensions and residual stress field. For other than shallow cracks, residual stress redistribution in the basic material invalidates the superpostion principle. Other researchers however have argued, based on Bueckners superpositon principle, that the redistribution of residual stress is of no consequence [17, 65], given that no plasticity effects occur during redistribution. Recently Wang [66] compared the weight function method to a finite element model and found very good correlation between the two models throughout the complete crack length; the maximum difference in $K_{residual}$ was 1%.

2.4.2 Modeling residual stress effects by the crack closure model

Since the superposition principle is founded on linear elastic analysis, the earlier mentioned crack tip plasticity effects cannot be accounted for. The crack closure model, however, employs crack tip plasticity to incorporate residual stress effects on the crack opening stress. This section shortly discusses the theoretical background and thereafter reviews literature in which the crack closure model has been employed.

2.4.2.1 Theory

The crack closure approach accounts for residual stresses by altering the crack closure stress level which changes ΔK_{eff}. Figure 2.11 shows schematically that if a crack grows through a compressive residual stress field the crack opening stress S_{op} will be higher and consequently the ΔK smaller and crack growth retarded. On the other hand, if the residual stress field is tensile the opening stress is lowered and ΔK will increase.

2.4.2.2 Literature

Newman et al [50] enhanced the FASTRAN [43] crack-closure model to simulate the introduction of compressive residuals tresses due to overloaded and cold-worked holes. The experimental data from Liu [67] and LaRue [68], who measured crack growth from overloaded open hole specimen and cold-worked holes respectively, was taken and compared to FASTRAN predictions.

Baseline crack growth data from tests at R=0.1-0.7 was collapsed into a single ΔK_{eff} curve to generate tabulated input data for the FASTRAN model and the model was partly rewritten to account for starter notch induced stress redistribution.

CA loading at R=0.1 on 7075-T6 showed an overestimate of the crack growth life, partly due to mismatches between the measured R=0.1 crack growth rates and the baseline ΔK_{eff} data. For a starter notch of 1.83mm the model was slightly conservative. For smaller starter notches, being 1.03mm and 0.24 the predictions became more unconservative (i.e. more cycles were predicted). This indicates that errors are

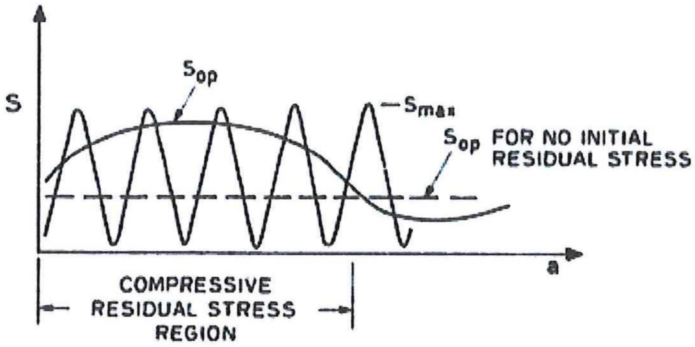

Figure 2.11: Variation of crack opening stress for growth initially through residual compression and on into residual tension [16].

present either because of a faulty calculated stress redistribution from notching or that crack closure close to the hole (there where the highest compressive stresses are present) is not captured accurately.
In order to predict crack growth from the cold-worked holes (from [68]) an overload was found by trial and error that gave similar residual stresses as compared to an FE model.

Non-cold-worked holes were used to varify the model and showed very good correlation to the test data. Crack growth from the cold-worked holes was also predicted accurately, except at the high rate regime. Overall, the FASTRAN model performed well on predicting crack growth rates through initially compressive residual stress fields.

Beghini and Bertini [54] used FE analysis to predict crack openings stresses and to compare the crack closure model to the weight function method (WFM). The residual stress profile on crack growth parallel to a weld was obtained by using the slitting method and served as input to the FE program. By using an iterative scheme, crack face tractions were included in the WFM solution. Here it was assumed that when crack closure occured, the crack face tractions were equal to (but opposite in sign) as the initial internal stresses.

Crack wake plasticity was modeled by deleting crack tip nodes at every load cycle thereby increasing the crack length. The J-integral was used to determine the stress intensity factor. Crack opening loads including residual stress effects from the FE model were compared to experimental values and agreed well. The weight function method underestimated the opening stresses slightly. From crack opening observations it appeared that, when the crack is partially closed the effective stress intensity factor tends to vary only slightly with external load. Neglecting the variation in stress opening due to partial closure was found adequate. It was conclued that both FE and the WFM provided accurate values of crack opening stress.

Choi et al [51] used an elastic plastic FE model to predict crack opening loads of rectangular C(T) and SEN(T) specimen. The residual stresses were introduced by a vertical weld and measured by slitting. The stresses were tensile around the weld line and (equilibrating) compressive outwards.

Crack growth was simulated by removing contact of one tip element after every load cycle; surface node displacement was monitored continuously to determine crack opening loads.

Through tensile and uniform compressive residual stress fields, the FE model predicted opening stresses somewhat lower than the experimental values. On uploading the crack opened inward from the crack-mouth-side towards the tip continuously, while on unloading the crack closed outwards from the tip to the mouth. Furthermore, the crack opening stress was slightly higher than the closing stress, which is in accordance with conclusions in [69].

Problems arose if the crack grew through a decreasing compressive residual stress or at the transition between compressive and a tensile field. The crack opening and closing behaviour through a compressive residual stress seems to be influenced by the relative magnitude of the applied load to the compressive residual stress distribution and the stress gradient in the transition region from residual compression to residual tension. Different partial crack opening and partial closure behaviour was found upon loading and unloading.

2.4.2.3 Critisism

The crack closure approach as used by the researchers above has been criticized because the method is founded on plastic deformations in the *wake* of the crack. According to Vasudevan et al [6] it is more naturally to expect stresses and strain history in *front* of the crack tip to determine crack growth, because here cracks grow. They also claim that this is the missing link between micro crack growth and macro crack growth, which is generally believed to be governed by different concepts (i.e. K-concept is not valid for micro cracks). Residual stress effects would then also be a function of the residual stress distribution in front of the crack tip. The reportings are based on fatigue threshold experiments in vaccuum, which showed that the fatigue threshold is independent of R in vaccuum and dependent of R under lab conditions what led to the conclusion of crack tip plasticity being not significant.

Predicting residual stress effects following the proposed analogy would be very challenging, because both finite element and the Dugdale strip method will require a very fine mesh to capture (reversed) crack tip plasticity effects and material behaviour is often not well-defined at very large strains and strain rates. Furthermore, experimental validation of the crack tip strains will give difficulties very close to cracks. By the author's knowledge, no attempts have been made yet to model crack growth in such a way.

2.5 Conclusions and research objective

Both the superposition principle and the crack closure model have been used extensively to account for residual stress and give reasonable crack growth predictions. Superpostion is usually used because of its simplicity. Weight function solutions are mostly limited to simple configurations and constant through-thickness residual stress. Remote crack closure effects can be significant but cannot be modeled by superposition. The method seems to suffer from high residual stress gradients were sharp drops in da/dN vs. ΔK are present, probably due to wake plasticity effects that cannot be accounted for.

K_{max} and K_{min} values can also be obtained directly from FEM. This requires a model in which the residual stress distribution is present either by directly modeling the stress introduction process or indirectly by inserting the measured residual stress distribution via Eigenstrains.

The crack closure model on the other hand has been applied by determining crack opening stresses via strip models and FEM. Direct experimental validation by crack tip opening measurements has proven to be difficult and sensitive to the chosen setup.

By looking at the aircraft industry needs, residual stresses need to be included into damage tolerance calculations for (cold expanded) riveted holes, shot peened or laser shock peened surfaces and thick sections which are milled from large blocks. From the authors perspective, the finite element method will be indispensable in the analysis of these complicated structures and 3D residual stress states. Therefore crack growth predictions through residual stress by means of FE must be validated extensively by experiments before implementation in damage tolerance calculations. Based on this, the following research objective is established:

> **Develop a methodology to introduce a well-known and consistent residual stress field in a laboratory coupon such that crack growth predictions through residual stress can be validated.**

To maximize the robustness of the validation crack growth test through various residual stress fields including sign transitions and at different R-ratios should be carried out. To validate the stress introduction as much as possible validation parameters must be measured such as full field strain distribution, applied forces, welding parameters, peening intensity and specimen curvature depending on which method is chosen. In order to validate FEM predictions, crack growth rates, crack opening displacements, crack tip opening stresses and crack front shape data is highly desirable. Furthermore, a LEFM prediction should be included to assess the performance of FE predictions against this widely used method. In the next chapter, various methodologies to introduce and measure residual stress are reviewed and the most appropriate method is chosen for use in this thesis.

Chapter 3

Residual stress measurement and introduction

According to the research objective a laboratory coupon in which residual stresses can be introduced and measured should be designed. The introduction of residual stress must be done in a controlled and consistent way such that multiple coupons can be obtained with similar residual stress distributions. The residual stress measurements must be accurate enough to verify the consistency between coupons. Based on these requirements, in this chapter a literature review will answer the following research questions:

> **1) What is the best method to introduce constant through-thickness residual stresses into a laboratory coupon in a consistent and well-defined way such that subsequently a crack growth test can be performed on this coupon with the crack growing through a compressive and tensile residual stress field?**
>
> **2) What is the most accurate method to measure the macro residual stress distribution in a metallic laboratory coupon?**

In order to answer these questions this chapter reviews the methods that have been used in literature to measure residual stresses (Section 3.1) and introduce residual stresses into coupons (Section 3.2). Finally in Section 3.3 the research questions are answered by selecting the most appropriate measurement and introduction technique.

3.1 Measuring residual stresses

In this section residual stress measurements are reviewed to assess the accuracy of each method.

3.1.1 Introduction

Residual stress measurement methods can be classified as destructive, semi-destructive and non-destructive [70, 71]. Non-destructive methods allow for further use of the inspected part, while destructive methods make further applications impossible. The coupons that will be designed in this thesis will be subjected to fatigue tests after the residual stresses are introduced. The use of destructive methods now gets problematic: destructive measurements prohibits subsequent fatigue testing.

This problem can be overcome if residual stresses can be introduced in specimens either in a very consistent manner and all coupons will assumably have equal residual stress or if both non-destructive and destructive methods are employed in cooperation. This latter can be achieved by first validating non-destuctive against destructive measurements (strain gauge data against hole drilling for example). If the non-destructive measurement is found satisfying, it can be employed on coupons such that these can be used for fatigue testing later.

From initial research it has been decided that neutron diffraction and sychrotron methods are omitted from this review because these methods are only available to specialist labs and are expensive to aquire [13]. The remaining techniques that are reviewed riquire equipment that is widely available.

3.1.2 The slitting method

The slitting method, often referred to as the crack compliance method, is based on the deformation of residual stress carrying specimens when slots are incrementally made in the specimen. As result of stress redistribution the specimen contour will change. This contour deformation is measured at a convenient position from which the original residual stress field in the specimen can be calculated by compliance techniques [22].

The compliance function is obtained from finite element calculations by calculating the strain which would be present at the measurement point for each slot depth when a dummy load is applied on the slitting surfaces. Lee and Hill [72] provide ready to use compliances for the back face strain reading at a beam specimen. Secondly, a least squares calculation is required to fit the theoretical set of strains to the observed strain changes. The result of the least squares fit is a set of slot face stresses which could theoretically reproduce the observed strain changes [73].

A typical measurement set-up of the slitting method is shown in Figure 3.1. The changes in strain due to successive extension of the slot length a is measured at the back side of the coupon by means of a strain gauge.

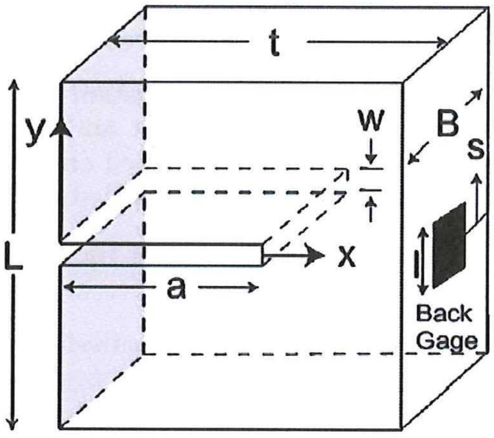

Figure 3.1: A slit is made to measure residual stress in y-direction along the slit. A strain gauge is used to measure strains at the specimen back side [74].

Other configurations are possible as well, for example two slits can be made next to a surface mounted strain gauge to determine surface stresses more accurately. This section focusses on through the thickness slits which enable residual stress measurement along the slit. In this way, stresses normal to the intended crack plane (y direction in Figure 3.1) can be measured. These stresses are important to know because they determine residual stress intensity factors. The remainder of this section reviews work performed by researchers to assess the applicability, accuracy and limitations of the slitting method.

Ritchie et al. [73] used the slitting method to evaluate its accuracy by comparing residual stress measurements to analytical predictions. Rectangular beams were stress relieved after which four point bending was applied to the specimens to introduce residual stresses. Before the tests were performed one stress relieved specimen was used to do a zero check of the slitting method to equantify experimental errors. From six measurements it was concluded that the maximum error of the slitting method in this configuration was 20MPa.

Next to the slitting measurements, the residual stresses were directly calculated from the bending strains from strain data on the top and bottom of the specimen. The solid dots in Figure 3.2 depicts the results for these readings. The averaged residual stress results for all strain gauges are represented by the + data points, while the solution from the back face strain gauge is given by the open squares.

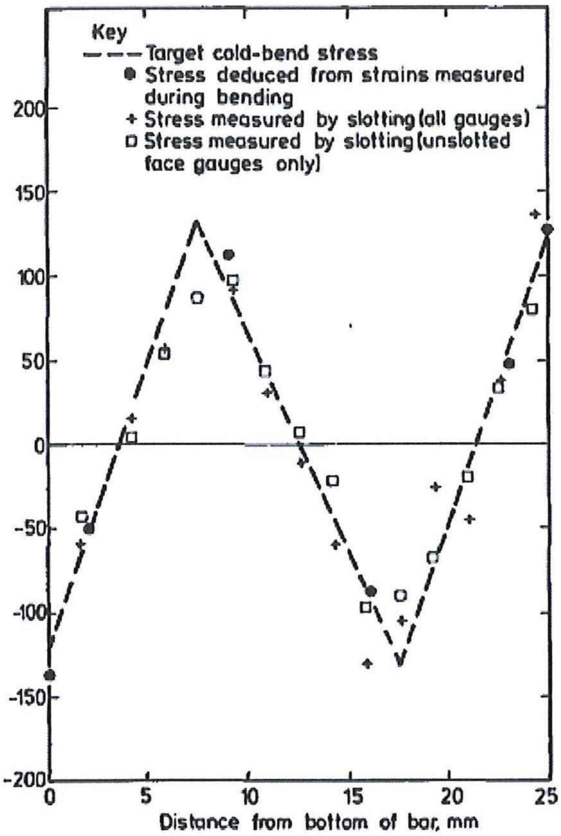

Figure 3.2: Development of stress in a cold-bent bar: results from the slitting measurements, results directly from strain readings and the theoretical stress distribution [73].

Concluded was that the results from the slitting method agree very well with the predicted values. The average result of all the gauges agreed well with those from the back side mounted gauges; this means that the latter can be used as stand-alone measurement which is particulary handy if acces to the side of the specimen is limited or if optical methods are used to measure surface strains (like digital image correlation).

A similar experiment to that of Ritchie et al. was performed by Lee and Hill [74]. Here the slitting method was used to measure through the thickness residual stress profiles on laser peened specimens. The purpose of the measurements was to quantify the repeatability of the slitting method on coupons with uniform residual stress.

A set of residual stress bearing samples was prepared by uniformly laser peening one surface of a single large stainless annealed steel plate and subsequently cutting this plate into small blocks. Laser peening was applied uniformly across the full surface of one side of the plate such that constant residual stresses between the different coupons was ensured.

After the specimens were cut from the plate, gauges were installed at the back side of the blocks precisely opposite to the cut and a total of six specimens were used. Wire EDM was used to cut the slots up to 17mm depth. Strain measurements at the aforementioned positions for the six slitting coupons are shown in Figure 3.3.

For each coupon the latest data point was omitted from stress computations because the measured strains departed abruptly from the trend. This effect was attributed to the decreased rigidity of the uncut ligament at large slit depth. This shows that the method can be applied up to about 90% of the specimen depth. The calculated stresses, standard deviations and maximum deviations are shown in Figure 3.3. The resulting residual stresses had the most variability near the start of the slit, where the standard deviation was 15 MPa. This translates to a relative error of 2% when normalized to the maximum measured stress at that location.

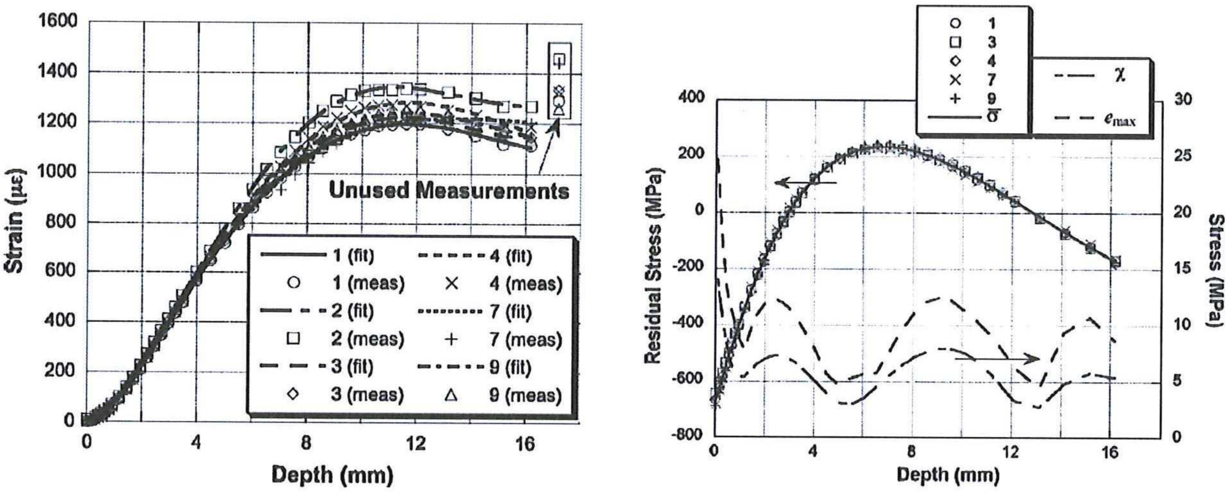

Figure 3.3: Measured strain data and strain fits for all coupons (left) and residual stress distributions for all coupons together with standard and maximum deviations. [74].

Concluded from the literature can be that the slitting method is a highly consistent and practical method to determine through the thickness residual stresses normal to the cut plane. Only one strain gauge is needed to generarate a 1D stress profile. Especially when cutting through compressive stresses, wire EDM can be used best to cut the slots. A difficulty with this method can be to cut the specimen at exactly the desired depth due to overcutting. The measurements proved accurate over a depth of 91% of the specimen width. The maximum point-wise error can be as small as 2% with a standard deviation of about 1% of the maximum residual stress.

3.1.3 Digital image correlation

Digital Image Correlation (DIC) is an optical method that can provide full-field displacements and strains by comparing the digital images of the specimen surface in the un-deformed and deformed states (e.g. [21],[75]). For 2D in plane deformations the method requires a digital camera, a light source and a computer only, whereas 3D measurements can be done with 2 cameras. This section first describes the basic principles of DIC and thereafter investigates the applicabililty to measuring residual stresses by reviewing existing literature.

DIC is based on the comparison between a reference image and a deformed image to determine strains and displacements in the latter, relative to the reference image. A digital camera is focussed on the test specimen and white light sources are pointed at the specimen to increase the clarity of the picture. The camera is positioned normal to the specimen surface and after the specimen has been deformed a second image can be taken. Imporant during these specimen deformations is that the specimen surface remains normal to the camera [21].

After taking the images the first step in the software processing is to divide the natural structure of the surface into grayscales. Now every pixel of the picture has its grayscale and by clustering several pixels together into unique combinations of pixels (which are called segments) a reference is made [75]. In the deformed picture again all pixels are given a grey intensity value. The software now scans this picture to find the same segments as in the reference picture and assigns a correlation coefficient to every subset of the deformed picture. The subset with the highest correlation coefficient is the one with the highest possibility of matching the reference subset. The difference in subset position between the reference and deformed image is finally displacement. Strains are computed from the relative displacement between two subsets.

If discontinuities such as crack or notches are present in the specimen or if large deformations are applied, the inital guess of the next point will not be reliable and possibly errornous [21]. Also the method cannot determine strains close to specimen edges. Usually for larger deformations larger speckle patterns must be painted on the specimen so that the original subsets do not get lost in the deformations. On the contrary, if small deformations are applied a finer speckle pattern can lead to higher accuracy.

To maximize the reliability and accuracy of the DIC method several practical issues must be considered. First, the out of plane movement between specimen surface and camera cannot be avoided completely because of possible specimen secondary bending, non flat specimen surface, poisson effect, loading device imperfections and camera vibrations. This error in 2D measurements can be reduced by positioning the camera *further* away from the test object so that out-of-plane displacements lead to smaller magnifications in the captured image. A telecentric imaging system can be used to compensate for these effects [21]. Second, the applied speckle pattern must have a maximum contrast and optimal speckle size (3 pixels per dot is often advised). Finally the noise in the measurement system can be reduced by controlling the temperature of the camera by keeping the environmental temperature constant, let the camera reach equilibrium temperature before used or by using a camera with active heating/cooling.

The experimental accuracy of the DIC method was investigated by Hoult et al. [75]. A tensile test specimen was clamped in a testing frame and uniaxial tension was applied to the specimen which corresponded to $1.000\mu\varepsilon$ in the specimen. At both sides of the specimen a digital camera was placed to record images of the strained specimen (see Figure 3.4). Additionally a strain gauge rosette was glued on the specimen to measure all three principal stresses as a reference.

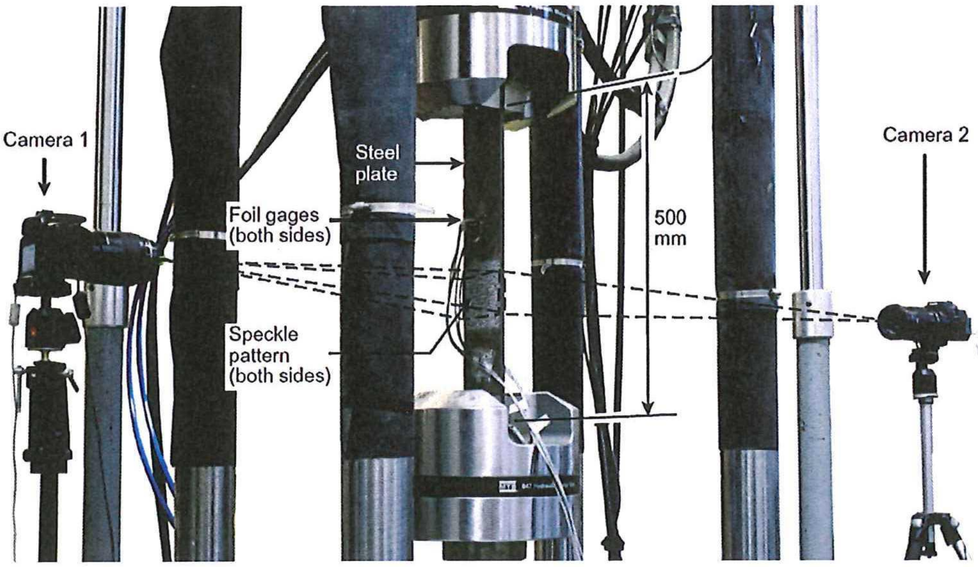

Figure 3.4: Experimental set-up of the steel tension specimen clamped in the testing frame to compare strain gauge rosette measurements and DIC using two cameras [75].

Both measurements showed good agreement with the rosette measurements; the maximum error was $22\mu\varepsilon$ on a magnitude of $1.000\mu\varepsilon$.

To obtain the residual stress distribution in the object, strains must first be translated into stresses by means of the stress-strain curve. For parts of the specimen which are completely in the elastic domain these strains can be directly converted to stresses via the Young's modulus. The residual stress at any yielded point, however, must be calculated via

$$\sigma_r = \sigma(\varepsilon_{max}) + E\varepsilon_{final} - E\varepsilon_{max} \tag{3.1}$$

in where ε_{max} and ε_{final} are the maximum and final strains respectively during specimen loading. This implies that at least three strain states need to be measured to effectively calculate residual stresses from inhomogeneous deformed specimens: the initial undeformed state, the maximum deformed state and the final state.

All together, based on the working principle, the measuring simplicity and the required equipment, digital image correlation is found to be a possible candidate to measure the residual stresses in laboratory specimen. The DIC method can be used with maximum accuracy if the residual stresses are introduced in such a way that the specimen does not have to be unmounted from a fixture. Furthermore, the camera must have a clear view on the specimen when the images are recorded. Altogether these requirements make DIC an appropriate technique to measure residual stresses from bending, cold hole expansion and in plane compression but is not suitable for methods like quenching or rolling. Additionally, since a full field surface strain can be obtained this method can be used to validate finite element simulations of the residual stress introduction.

3.1.4 The hole drilling method

One of the most used techniques for measuring residual stress is the hole drilling method [76, 71]. Hole drilling has been applied extensively in the past because of its relative simplicity and speed. Furthermore, hole drilling is the only residual stress measurement method next to X-ray diffraction with a standardized procedure (ASTM E837-99).

Discriminated can be between conventional hole drilling and deep hole drilling methods, which differ slightly in methodology. The kind of stress fields that can be measured (through thickness, gradients, residual stress amplitude) are reviewed in this section together with the applicability and accuracy of the method, based on work performed by third-parties.

3.1.4.1 Conventional hole drilling

The principle of the technique contains the introduction of a small hole into a component containing residual stresses and subsequent measurement of the locally relieved surface strains. The residual stress can then be calculated from these strains using formulae and calculations derived from experimental and Finite Element Analyses [71]. In practical terms, a hole is drilled in the component at the centre of a special strain gauge rosette. Close to the hole, the strain relief is measured in three directions from which the principal strains can be derived. A typical measurement set-up can be found in Figure 3.5a.

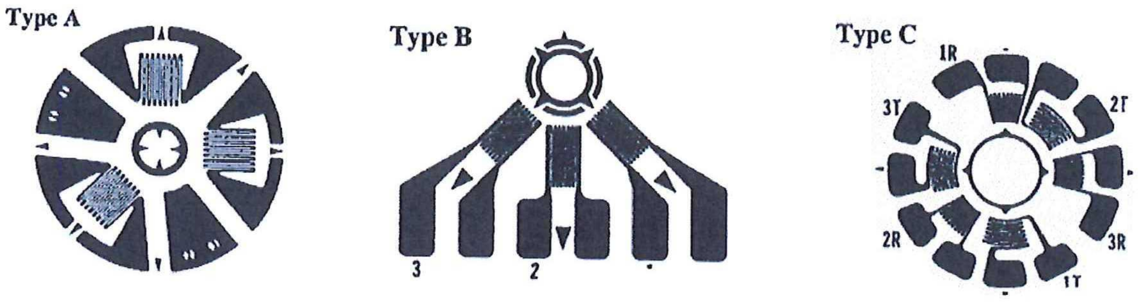

Figure 3.5: Strain gauge rosette geometries through which a hole is drilled [71].

The hole drilling technique measures in-plane strains at a specimen surface which contains gradually changing residual stress fields. Highly non-uniform residual stress fields will lead to large measurement errors because the rosette measures strain at three different locations, which will give different readings.
Other configurations are possible as well. Rosette configurations as shown in Figure 3.5b are tailored to residual stress measurements at notches or obstacles like radii or fillets. Set-up c uses six strain gauges to

increase the sensibility of the measurment by measuring every strain direction twice.

Residual stresses can be determined up to a depth of one hole diameter. This is because deeper drilling does not lead to measurable strain relief and thus do not represent the residual stress field correctly [71]. Furthermore the method can be applied without corrections of residual stress values up to 50% of the local yield strength of the specimen. In this way local yielding due to the stress concentration of the hole is avoided.
To increase the spatial resolution smaller hole increments can be used. This however also reduces the strain gauge readings which leads to bigger errors in the measurement. Optimal step size have been calculated and are available in [77].

Not only errors due to stress analysis occur in the drilling procedure, but practical measurement can also introduce significant errors. The main five sources from which measurement errors originate are [77] listed below. The uncertainty as given between brackets come from a literature review by Oettel [78].

- Strain measurement errors, including instrumentation errors, thermally induced apparent strains and additional residual stresses induced by the hole drilling process [±2-5 %].
- Hole depth measurement errors, including any non-flatness of the bottom surface of the hole.
- Hole diameter error, including diameter measurement errors, tapering of the hole, and deviation from roundness.
- Material constant estimation errors, including uncertainties in the given elastic constants [1% for yield strength, 3% for Poisson's ratio].
- Hole eccentricity errors, including possible eccentricity of the hole from the centre of the strain gauge rosette.

More errors can be introduced if subsequent measurements are performed too close to each other. The introduced error was found to be smaller than 2% if a spacing of more than 10 times the hole diameter was used [78].

The errors in strain measurement, hole diameter and eccentricity can be reduced if the full field strain is measured by optical techniques such as digital image correlation [79]. A challenge here is to extract the right information from the vast amount of data.

Based on the previous data it can be concluded that the hole drilling method is a relatively accurate and proven method to perform residual stress measurements. Advantages are that the technique does not need sophisticated specialized equipment and is fast to implement. The method however is sensitive to errors in the experiment and highly relies on the skills of the operator. Also the complete through-the-thickness stress field cannot be measured by hole drilling and is limited to roughly the hole diameter. Spatial resolution is limited to 10 times the hole diameter, which with a typical hole diameter of 1.8mm results into one measurement per 18mm.

3.1.4.2 Deep hole drilling

The deep-hole drilling (DHD) method consists of drilling a small reference hole through the specimen and thereafter incrementally drilling a circular slot around the reference hole [80, 81]. Measurement of the reference hole diameter is undertaken at different angles around the hole axis and at many intervals through the reference hole usually by means of an air probe. Then a column of material, with the reference hole as its axis, is trepanned from the specimen and the residual stresses are relaxed in the column. After trepanning, the reference hole diameter is remeasured and relaxed strains are subsequently determined from the diameter measurements before and after trepanning. The procedure is schematically depicted in Figure 3.6.

The major advantage of deep hole drilling above conventional hole drilling is that the complete through-the-thickness residual stress field can be mapped and that the relieved strains are larger which allows for better measurements [82]. On the other hand, more specialized equipment is needed for cutting the annular

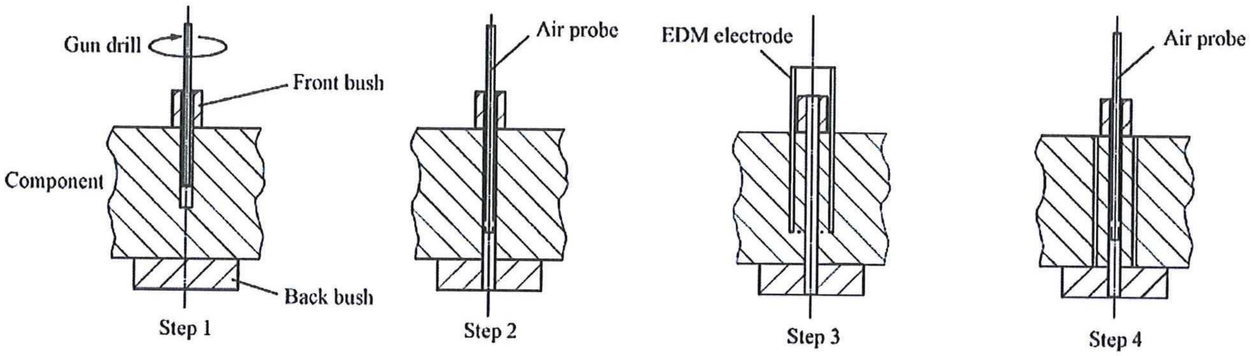

Figure 3.6: Schematic of the deep hole drilling process. Modified from [81].

slot and to measure inside diameters accurately. Furthermore, the deep hole drilling will require more time because of the additional slotting that must be performed.

The accuracy of the method was investigated by several authors. Mahmoudi et al. [82] validated the methods against FE analysis for a shrink fit assembly (Figure 3.7a).

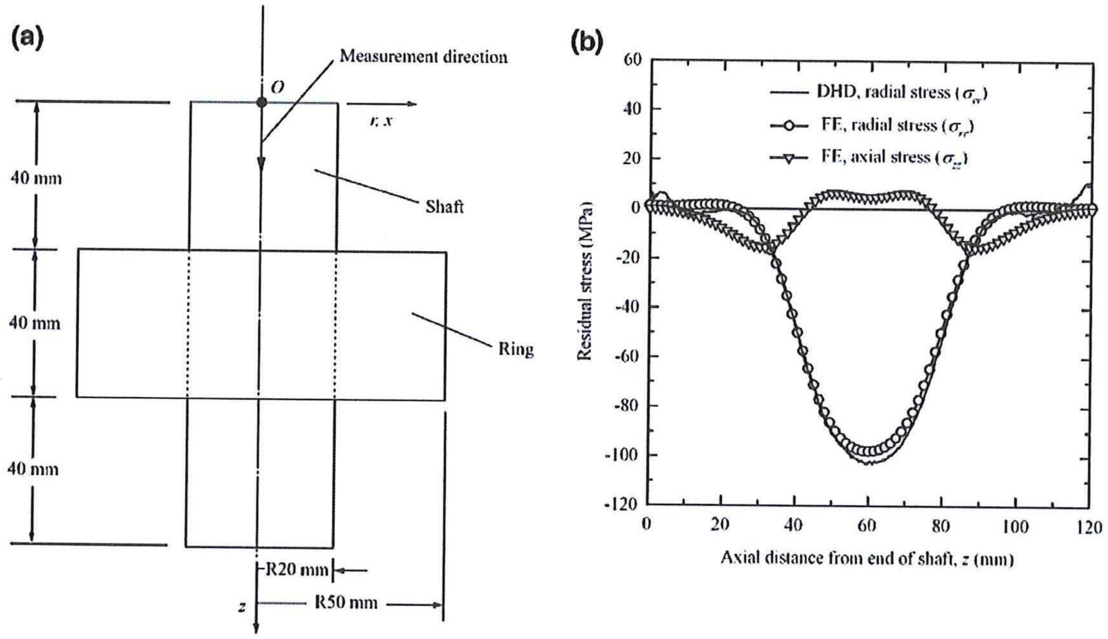

Figure 3.7: Residual stresses in a shrink fit assembly: (a) dimensions shrink fit assembly and (b) residual stress profile along the shaft axis from FE analysis compared to the deep hole drilling method [82].

The result of the measurement is shown in Figure 3.7b which reveals that at the edges of the shaft, where the radial stresses were expected to be zero, a tensile stress of 10MPa was measured. These errors were associated to errors in the measurement of the radius using the airprobe near a surface. The radial stress is highest in compression midway along the shaft and reaches 103MPa. The results from the FE model and the DHD methods correlated good. The peak value of compressive residual stress was 98MPa, within 5% of the measured value.

George et al. [80] conducted three experiments where the deep hole drilling method was used to measure externally applied loads to aluminium tension specimen, steel bending bars and aluminium pressure cylinders.The tension specimen were subjected to uniform tension and a hole was drilled in the center of the specimen normal to the applied load. Reference hole diameters and the deformation of the hole under the applied load was measured by means of an air probe. Several specimens with different thickness and hole diameters were tested. Good agreement was observed between measured and calcuated stresses. Measurement errors were ±10MPa in the aluminium pressure cylinder and up to ±25MPa in the steel beams. Additionally two different probe sizes (1.5mm and 3.175mm) were used on one specimen to quantify the effect of probe size on the measurement error. It turned out that the smaller probe produced errors of about 20MPa whereas with the bigger probe the residual stresses were determined within ±10MPa.

All together, the deep hole drilling does not provide big advantages over conventional hole drilling. However, if the residual stresses through the thickness are required the former is preferred. Nevertheless, since through the thickness stress gradients are often quite high (such as is shot peening, LSP and rolling) and considering the limited depth resolution of the method this can result into errornous residual stress data. Also since a usually large annular ring must be removed around the reference hole, multiple in plane measurements can only be done with large spacing between each measurement to avoid interferene. Deep hole drilling is not suited to residual stress mapping over an area unless a large amount of equally prepared specimen is available. If a constant through the thickness stress is assumed, for example after in-plane bending or stretching, the method can serve as a check to this assumption.

3.1.5 The countour method

In a similar fashion to the hole drilling methods, the relatively new contour method relies on the strain relaxation of components when they are cut in two [76]. After cutting the material, the surface created by the cut is measured by a coordinate measurement machine to generate a surface profile showing deformation normal to the cutting plane. By now using the surface profile as a displacement boudary condition in an FE model, the original 2D residual stress field at the cut surface can be reconstructed [83].
The method is founded on the elastic superposition principle as shown in Figure 3.8.

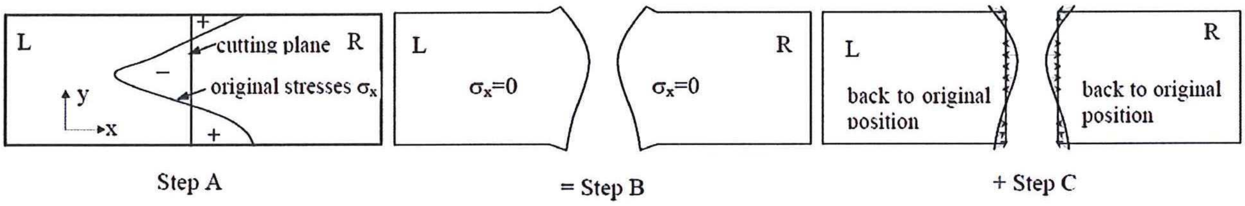

Figure 3.8: Illustration of the superposition principle as used by the contour method [84].

The original stress distribution in the material (step A) causes the material to deform normal to the cutting plane when it is sectioned (step B). This deformation can be forced back to the original shape by applying a certain stress distribution on the cutting plane (step C). The out of plane deformations of the cut section are inverted in sign (i.e. valleys become peaks and vice versa) and are applied to one half of the original specimen in an FE model as surface displacement boundary condition. The stresses at the deformed plane now equal the original residual stress field.

The main assumption is that all residual stress induced displacement is linear elastic. Furthermore it is assumed that the cut is perfectly straight, removes no material and does not introduce additional stresses in the specimen [83]. Experiments have shown that the first assumption is true even if residual stresses above yield are examined [85]. The other assumptions are approximately true if EDM wire cutting is used, which is found to make very straight, thin (as thin as $100\mu m$) and almost stress free cuts [83, 86, 87].
par The presence of any shear stress in the specimen does not influence the measurement if the surface profiles of both halves are averaged before data reduction. This is true because transverse tractions are anti-symmetric with respect to the cut plane and will therefore cancel out during averaging [83]
As stated before the cut must be straight with respect to the original specimen. The residual stress relieve during cutting however causes the specimen to move normal to the cutting plane and thereby creates a curved cut. It is thus of paramount importance that both sides of the specimen are sufficiently and symetrically clamped such that specimen movement is restricted [83].

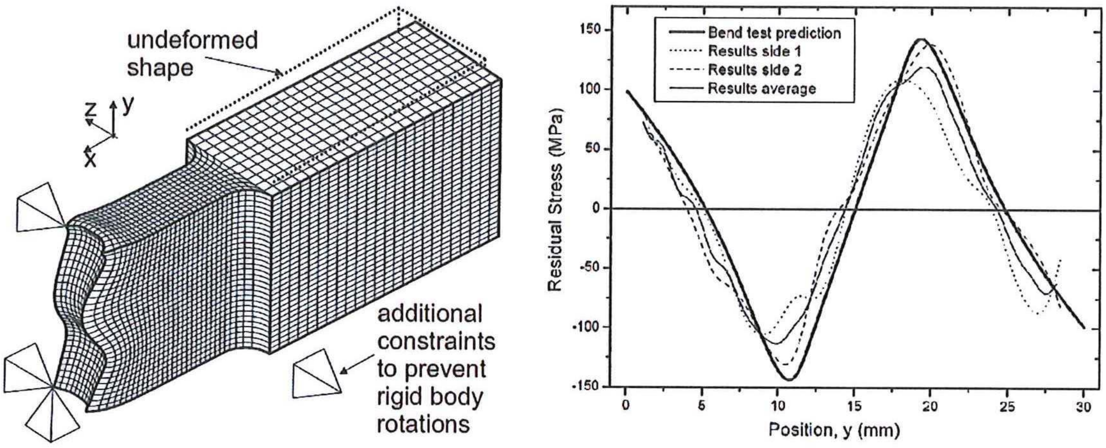

Figure 3.9: The FE model of a cold-bent rectangular specimen showing constraints and magnified boundary displacement (a) and the measured and predicted residual stresses (b) [83].

The accuracy of the method was validated by Prime [83] against a four-point-bent test. A rectangular beam was plastically bent and then unloaded. The specimen was subsequently clamped on a base plate and cut in two halves by using EDM. The surface profile was measured by a point probe, smoothed by aplying a Fourier series fit to the measured contour and finally applied as displacement boundary to the FE model (Figure 3.9a). The results of the calculations are depicted in Figure 3.9b which shows that the method follows the linear elastic prediction reasonably well with a maximum error of 16%.

It was noted that the surface deformations were relatively small (maximum peak-to-peak deformation was about 10*μm*) because residual stresses were low (max 150MPa) and a high modulus steel was used. Using softer material and larger residual stresses would increase the surface deformations and thereby increase measurement accuracy [83].

Zhang et al. [84] compared the contour method against FE predictions for a 4% cold expanded hole. The cutting and profile mapping procedures were the same as used in the study by Prime [83]. The 2D stress map from the contour method and the FE model are given in Figure 3.10a and b respectively.

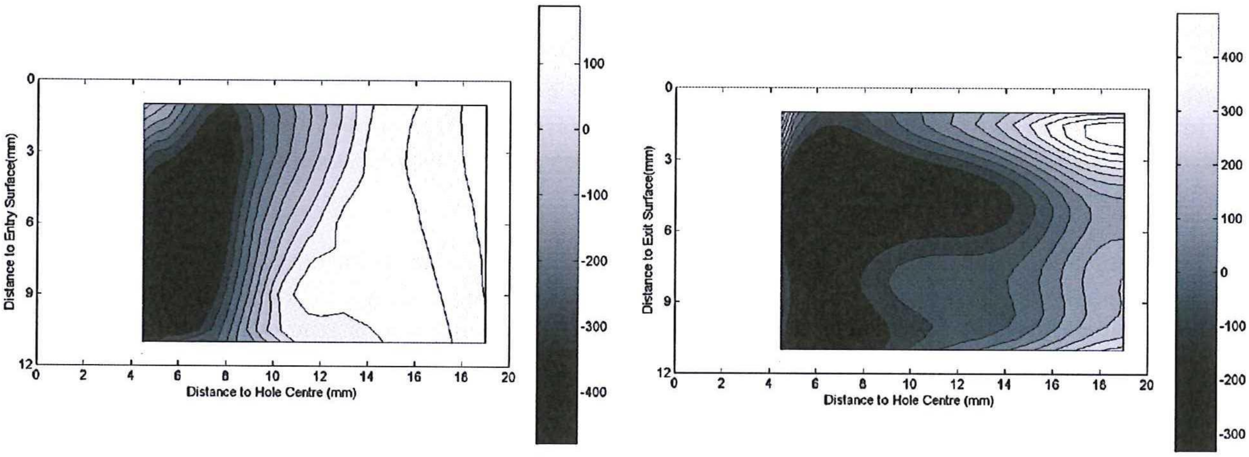

Figure 3.10: Hoop residual stresses as measured by the contour method (a) and FE model (b) [84].

It shows that the hoop residual stress measured from the contour method was in broad agreement with the output from the FE model. Arguments for the disagreement between the two figures are that cold expansion is difficult to model which could lead to errors in the FE model. It was also stated that the contact probe had difficulties to measure at the very edge of the specimen. Finally the required data smoothing filtered out some of the peak measurements which resulted into lower stress peaks.

Surface mapping errors were investigated in more detail [86] by mapping the profile of a weld-specimen using both a touch probe and laser mapping. Both methods were compared to neutron diffraction measurements. The residual stress maps generated by the touch probe (resolution $\pm 1 - 3\mu m$), the laser contouring ($\pm 0.4\mu m$) and neutron diffraction compared very well and had estimated errors of 32MPa, 24MPa and 35MPa respectively.

The raw topographic data of the touch probe and laser contour measurement were smoothed by fitting polynomials to the data. Selecting more polynomials gives more accurate results but also captures more noise; an optimum must be found for each measurement.

It can be concluded that the contour method is a promising method to determine residual stresses. The experimental results in the literature compare reasonably well to other residual stress techniques. The method is primarily suitable for complex 2D residual stress mapping; 1D residual stresses can be measured more conveniently with the slitting method (Section 3.1.2). The contour method requires an EDM machine with a clamping device and a highly accurate surface contour mapping machine. The calculational portion is extensive compared to other methods and can give rise to subjectivity, which reduces the repeatability of the method.

3.1.6 X-ray diffraction

X-ray diffraction relies on the elastic deformations within a polycrystalline material to measure near surface stresses in metallics [88]. Stresses change the spacing of the lattice planes and can be measured directly and subsequently converted to stresses by Hooke's law.

The X-ray machine radiates the specimen surface with monochromatic X-ray beams and at the same time measures the refraced beams with a detector. The impinging beams (1,2, and 3 in Figure 3.11) will be scattered in all directions by the crystal atoms. In some directions however an increased intensity is observed due to the constructive interference of the scattered waves. The conditions for constructive interference can be derived from Figure 3.11 in where the path length difference between the diffracted beams (1' 2' and 3') is an integer times the wavelength.

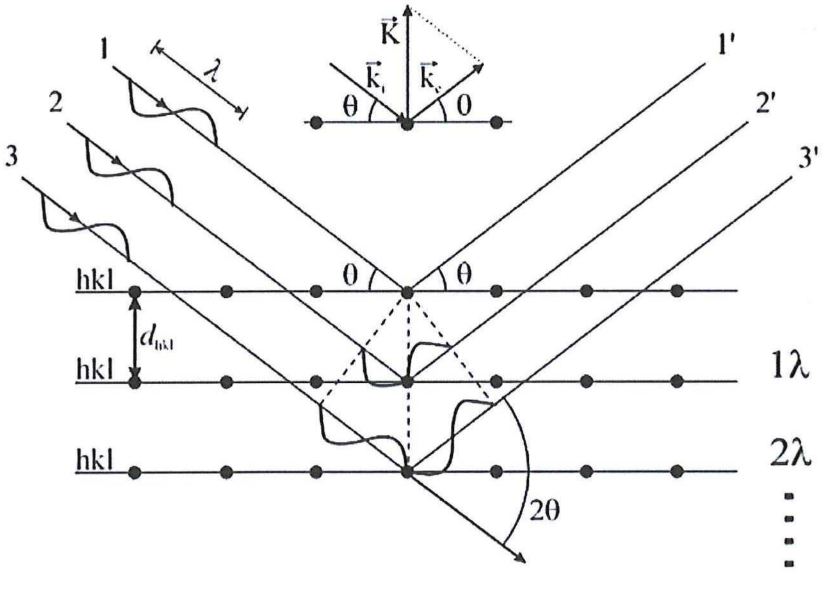

Figure 3.11: The X-ray working principle. The incident angle θ and lattice spacing d are chosen such that the diffracted waves are in phase and constructively interfere [89].

Bragg's equation is relates the incident wavelength λ to the change in the Bragg scattering angle $\Delta\theta$:

$$n\lambda = 2dsin(\theta) \tag{3.2}$$

giving with d_0 as stress free lattice spacing:

$$\varepsilon = \frac{d - d_0}{d_0} \tag{3.3}$$

Because the method compares the stress free lattice spacing to the stressed spacing it is necessary to have d_0 accurately measured. By assuming a plane-stress condition at the surface layer the popular $\sin^2\psi$ method does however not need a reference measurement [70]. Although the measurement is considered to be near surface, X-rays do penetrate some distance into the material. Hence the measured strain is actually the average over a few microns depth under the surface of the specimen [29].

The main sources of error are misalignment of the specimen, insufficient specimen surface quality (roughness, pits) and the type of residual stress that is measured [70]. Misaligning the specimen with respect to the incident angle gives faulty stress calculations because the slope of the lattice spacing vs. incident angle is used to determine stresses. The surface quality is important because surface layers like corrosion can distort the X-ray beams [88]. Non-flat surfaces like small diameters, fillets or threads also contribute to errors as ψ is tilted over the sample area.

If the sample area is chosen too small, or the metal grains too coarse, Type II residual stresses can be measured instead of Type I stresses (see Section 2.2.3). The diffraction method measures the average strain value over the sampling area. If a too small sampling area is chosen not the bulk stresses but very local grain orientation dependent stresses are measured [88]. A minimum sampling of 1mm by 1mm square is often used.

Francois et al. [90] studied the consistency of the X-ray method by measuring stresses at one reference specimen in 21 different laboratories. A shot peened steel plate with highly compressive residual stresses was tested in all the participating labs independenty. The average value of the stress σ_{11} is -469MPa and -436MPa for σ_{22} with a standard deviation of 32MPa and 30MPa respectively.

Next to the plate measurements, a stress free powder was investigated in all labs. This lead to an average normal stress of 3.2MPa with a standard deviation of 4.5MPa. Concluded from these small stresses was that misalignment errors were small. To check if the used software influenced the results all measurement data was subsequently analyzed with one software package. The average normal stress value was slightly higher but with a significantly lower standard deviation of 18.5MPa. This means that the used software does have a significant influence on the results.

The above mentioned shows that the X-ray diffraction method is a fairly consistent method to measure surface residual stresses. This on the conditions that the used material is polycrystalline, the specimen fits in the machine and the surface is clean and flat. Since the average stress over an area of at least $1mm^2$ is taken, high stress gradients are not captured accurately. This means that X-ray diffraction is not suitable to measure full field residual stress distributions but could serve well as a supplement to slitting or DIC measurements at coupon edges.

3.2 Introducing residual stresses into coupons

In the literature different techniques have been used to introduce such stresses from which the most popular are welding [91, 52], shot peening [92], plastic bending [93] and cold hole expansion [23]. Next to these processes also common techniques like machining, grinding or rolling produce residual stresses [11]. Machining and grinding are not suitable because of the difficulties with controllability (e.g. wear of tooling). Rolling requires large dedicated machines which are not generally available for laboratory coupons. Quenching has also been used in several studies [10, 94]. The controlability of this method is however regarded as insufficient and therefore not included in this review.

Shot peening and laser shock peening introduce high near-surface compressive stresses with high gradients. This could lead to sub surface crack initiation if crack growth tests are performed on peened coupons. Furthermore, a starter notch in the compressive zone would lead to a very large stress redistribution. Peening is therefore not an option for residual stress introduction.

In the end, plastic bending and hole expansion are the best suitable methods to introduce residual stresses. These will be reviewed in the following sections.

3.2.1 Plastic bending

Bending can be regarded as the most elementary operation to introduce residual stresses into a material. The bending operation creates residual stresses into specimen by plastically deforming the outer fibers, which results into residual stresses after unloading. The bending method requires a compression bench and a 4 point bending frame to perform the test.

Two standardized test methods are available for measuring material flexure by bending. These are the three point bending and four point bending test methods which are standardized in ASTM790-10 and ASTM D6272 respectively. The three point bending test generates at point wise maximum loading moment whereas the four point bending procedure has been designed to apply a constant bending moment over a certain span. This will create a constant residual stress field over the load span and is therefore the reviewed method.

3.2.1.1 Working principles of four point bending

In the four point bending test a specimen is loaded in a test rig with four contact points. Figure3.12 shows schematically how the stresses develop during the bending operation. When a small moment is applied to the specimen a linear stress distribution will develop over the height of the specimen from the linear strain distribution (a). When the moment is further increased the outer fibers start to yield first, which will give a non-linear stress distribution over the height (b) while the strain remains linear (c). If now the forces are relaxed and springback is allowed, residual stresses develop as in (d) with an alternating compressive and tensile stress zone.

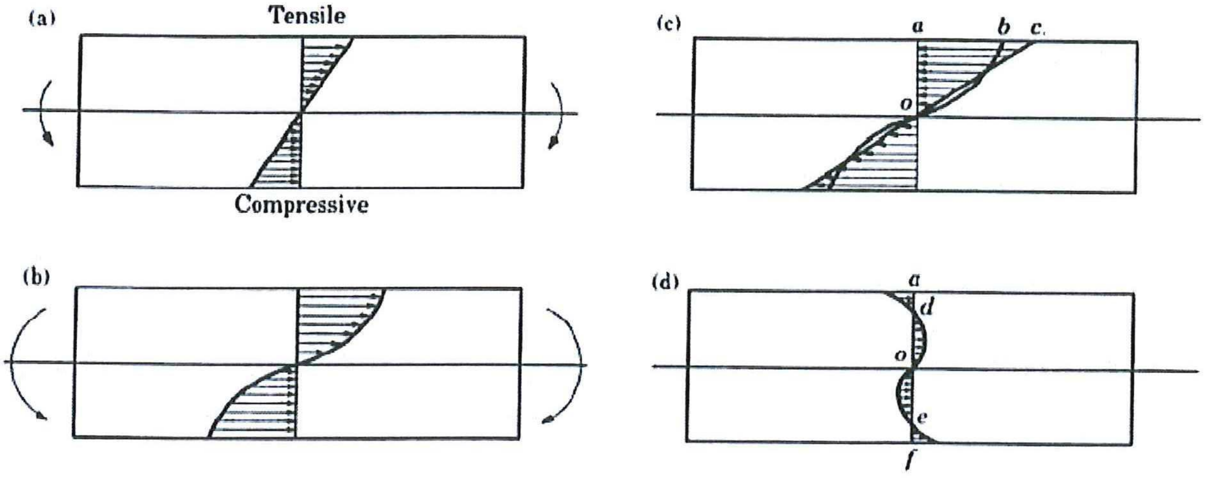

Figure 3.12: Stress development in a beam under four point bending [95].

3.2.1.2 Residual stresses from bending

An initial estimation of the residual stresses due to plastic bending can be made analytically. If elastic-perfect plastic material and a linear strain distribution is assumed, the first moment of stress can be integrated over the specimen height to obtain the required bending moment [73]:

$$M = \frac{E\epsilon_y bt^2}{12}(3 - \frac{1}{s^2}) \tag{3.4}$$

in where t is the bar height, E is the elastic modulus, ϵ_y is the yield strain, b is the thickness and s is the ratio of the extreme (outer) fibre strain over yield strain. The surface stresses then follow from

$$\frac{\sigma_{surface}}{\sigma_{yield}} = \pm\left(\frac{1}{2s2} - \frac{1}{2}\right) \tag{3.5}$$

and the internal peak stress can be calculated by

$$\frac{\sigma_{peak}}{\sigma_{yield}} = \pm\left(1 - \frac{3}{2s} - \frac{1}{2s^3}\right) \tag{3.6}$$

It can be seen that for s=1 the residual stresses are zero. The stress distribution for different levels of outer fiber strain is plotted in Figure 3.13.

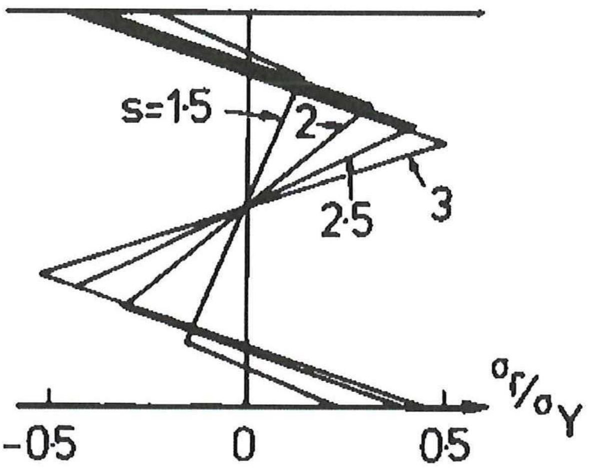

Figure 3.13: Residual stress distribution after different ratios of extreme fiber strain and yield strain [73].

As the bending load increases the internal peak shifts towards the neutral axis and increases in magnitude. Consequently, by controlling the bending forces the magnitude of the residual stress, stress gradients and the plastic zone can be controlled.

The residual stress distribution from the bend test were validated against the slitting method by Ritchie [73], against X-ray diffraction, neutron diffraction and the contour method by Prime in [96] and [83].

The residual stress profile from the slitting method by Ritchie and the analytical prediction was given in Figure 3.2. The analytical solution agreed very well with the slitting method and strain gauge readings. Only the predicted tensile peak stress was not confirmed by the measurements.

As mentioned in section 3.1.5 the contour method also gave good correlation to the four point bending test in [83]. A beam was plastically bent and unloaded. Strain and load measurements during bending were used to calculate the residual stress profile, see Equation 3.1. The residual stress profile from the contour method agreed well (Figure 3.9), though the neutral axis was found to be off-center and the maximum peak stresses were not found to be as high as predicted.

Prime reported X-ray and neutron diffraction measurements on identically prepared specimens in a different paper [96]. The stress-strain curves from strain gauge readings showed different behaviour beteen uploading and unloading of the beam. This effect was incorporated in analytical solutions for the residual stresses which lead to a compressive peak which was 20% bigger than the tensile stress peak.

The results are shown in Figure 3.14 which shows that the neutron diffraction measurements agreed with the predicted stresses and that the X-ray measurements gave scattered results. This was attributed to the variation in grain sizes over the specimen surface and related errors.

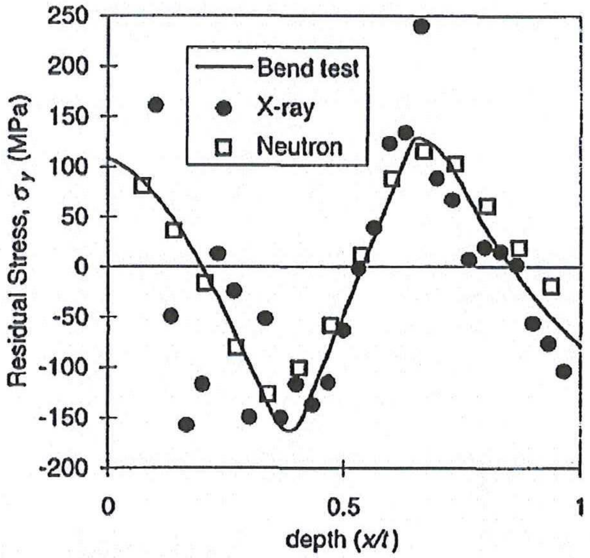

Figure 3.14: Measured and predicted residual stresses through the height of a cold-bent beam [96].

The neutron diffraction measurements correlated very good to the strain deduced stresses, but gave a more symmetrical distribution about the neutral axis and did not show the expected higher stress peak at the compressive side. A possible explanation can be the sampling area of $4.8mm^2$, which can smear out high peak values.

The above reviewed literature suggests that the four point bending method is a convenient method for residual stress introduction in coupons. Gradually changing residual stress fields over specimen height are generated and can approximately reach half the yield stress. The consistency of the operation depends on specimen positioning, contact friction and roller alignment. If the latter is not done correctly a sideway bending moment is introduced in the coupon which gives non-uniform residual stress over thickness.
par Strain controlled testing is preferred over load controlled to reduce scatter between coupons from friction and coupon dimensions. There is no limitation is use of DIC because of an open field of view during the bending operation.

3.2.2 Hole expansion and hole pre-yielding

Over the last 40 years a popular method to improve the fatigue life of fastener holes has been cold hole expansion. This technique can be used to introduce residual stresses in laboratory coupons by pulling a mandrel through the sheet. A similar stress distribution can be obtained by in plane stretching of a sheet with a hole, called the hole preyielding method. This section reviews previous work on residual stress measurements and predictions around cold expanded holes and overstretched sheets.

3.2.2.1 Working principles of cold hole expansion and preyielding

The cold hole expansion method requires the insertion of a hard tool in an existing hole to deform the pheriphery of the hole plastically both in radial and hoop direction. When the tool is removed from the hole, the elastically deformed bulk material around the hole forces the permanently deformed region to spring back so that compressive residual stresses are generated around the hole.
The most widely accepted method is the aerospace industry is the split-sleeve process [97]. This process involves pulling an oversized tapered mandrel through an internally lubricated split sleeve. The presence

of the sleeve reduces damage to the structure by preventing sliding contact between the mandrel and the structure.

In constrast to the cold hole expansion technique preyielding does not require any tooling to expand the hole. A residual stress distribution is obtained by in-plane stretching of the specimen by which a yielded zone is created at the hole edge, perpendicular to the loading direction.

3.2.2.2 Residual stresses from cold hole expansion and preyielding

The residual stress distribution after split-sleeve hole expansion of 7050-T76 aluminum 5mm blanks was measured by Ozdemir et al [97]. They used the Sachs boring technique, which is essentially a modified deep drilling method (see section 3.1.4.2).

Figure 3.15 shows the evaluated hoop stress profiles. The maximum residual hoop stress reaches -450MPa ($\approx$ 90% of the yield stress) at roughly 1mm from the hole edge. From this maximum the compressive stresses decrease quickly towards zero at about 3mm from the edge. It can also be seen that increasing the expansion from 4% to 6% did not increase the compressive residual stress, concluded was that the maximum residual stress saturates at 4% expansion.

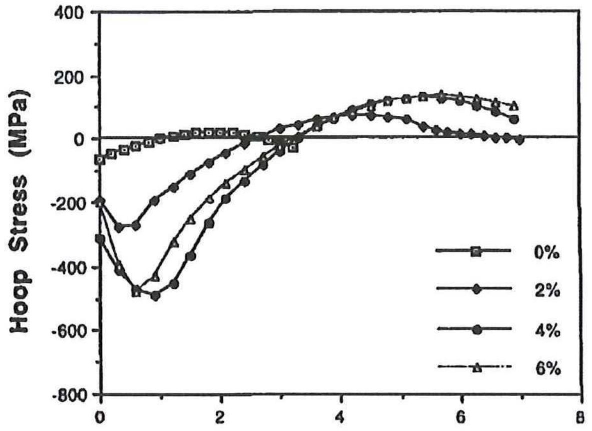

Figure 3.15: Effect of degree of cold expansion on residual hoop stress distribution [97].

To validate the measurements against theory, a comparison was made between the measured data and three analytical analyses. The agreement was reasonable for stresses far from the hole, but a mismatch occured at the egde of the hole where the predicted stresses were much higher than the measured stress. A possible explanation for this effect was given to be the Bauschinger effect.

The Sachs boring measurements were performed at the mandrel inlet side, at the blank mid section and at the outlet side. Furthermore, X-ray measurements were made at the inlet and outlet positions. Both measurement techniques showed that the compressive residual stresses at the inlet were considerably lower ($\approx$300MPa) than these at the outlet side ($\approx$400MPa).

Finally the angular variation in stress around the hole axis was determined by measuring in multiple angular directions. It was found that the peak stress at 90° from the slit was maximum (490MPa) and minimum (260MPa) at the direction opposite to the slit. At the position of the slit a tensile stress of 280MPa was measured which was attributed to the inhomogeneous plastic deformation due to the presence of the sleeve.

The same slit sleeve method was used by Stuart et al. [9] on aluminum 7050-T6 sheet material. Three identical dog-bone shaped coupons were cut from base material. Central holes (7mm) were drilled in the test section and expanded by 3%. Residual stress measurement were performed with the contour method (see section 3.1.5) to determine hoop stresses on the planes both left and right from the hole.

The measured residual stress distribution is similar to the one obtained by Ozdemir et al. [97]. The stress is highly compressive (-475MPa) near the hole edge and reaches the zero stress point at 2mm from the egde. A big difference however, is present near the hole surface. It was found that the stresses are maximum at the hole egde, instead of further away from the edge.

The correlation between the six measurements (left and right for each coupon) was good. The residual stress standard deviation is 40MPa at the very edge and quickly drops to ≈5MPa at a depth of 2mm.

Despite the small sheet thickness, also in this study a though-the-thickness stress variation is measured showing higher compressive stresses at the faces than at the mid section. Peak stresses are now found at the mandrel inlet face instead of the exit face.

Similar experiments to that of Stuart were conducted by Liu et al. [98]. LY12-CZ aluminum plate material of 4mm thickness were cut into dog-bone specimen after which a central hole of 5mm diameter was drilled. Split sleeve cold hole expansion ranging from 1% up to 10% strain was applied to the holes to map several residual stress distributions.

X-ray diffraction and FE analysis was used to determine residual hoop stresses up to 13mm from the hole edge. The FE results were comparable to the results in [9] and [97]; the maximum hoop stress was found at about 1mm from the edge with a magnitude close to the material yield strength. The X-ray measurements did not show the local compressive peak stresses and showed a much more gradual distribution. Whereas the values close to the hole edge differed significantly, for depths greater than 3mm the results coincided very good. The discrepancies were attributed to the relatively large sample size of the X-ray machine (1x1mm) which smeared out the peak values and secondly the reaming process was not taken into account in the FE analysis. A potential stress redistribution lowered the measured stresses.

Compact tension specimens with a circular notch were overloaded by Ghidini and Donne [60] to generate a residual stress field in front of the notch. Two 2024-T3 and two 7475-T7351 specimens were used for the residual stresses measurements. Back face cut-compliance showed good consistency and generally followed the FRANC2D finite element solutions except very close to the notch. Here the measured compressive stresses exceeded the compressive yield stress by factor 1.5. Errors were attributed to the limited sensitivity of the back-face strain measurements for shallow cuts.

In conclusion, the cold hole expansion procedure generates high compressive residual stresses around holes in hoop direction and also compressive, but somewhat lower stresses in radial direction. An often used strain of 4% generates stress compressive fields as large as a quarter of the hole diameter. Further away from the hole tensile stresses equilibrate the compressive stresses. Preyielding of holes gives similar stress distributions perpendicular to the applied loading. Through-the-tickness stresses are not constant for cold expanded holes which makes 2D crack growth predictions not applicable. Pre-yielding of holes give a more constant through-the-tickness stress distribution.

Finite element modeling of the cold expansion procedure faces difficulties because of the complicated mandrel-sleeve interaction, friction forces and unloading behaviour. The predictions generally agree with measurements with the contour method and the Sachs boring technique. X-ray diffraction measurements fail to map the near edge stresses correctly. The accuracy of preyielded hole FE models is difficult to assess because often either no residual stress measurement is performed on the specimen or the measurements have difficulties close to the hole edges (where the residual stresses are of highest importance).

The cold hole expansion method is standardized and relatively easy to use; high consistency in the literature has not been found between subsequent expansion results, most likely because of the uncertainty in residual stress measurements. Hole preyielding is not a standardized technique, but is also relatively easy to perform experimentally.

3.3 Method selection

From the sections 3.1.2 through 3.1.6 it has become clear that residual stresses can be measured by many different methods. Table 3.1 shows an overview of the reviewed methods including their penetration depth, spatial resolution and estimated accuracy.

Table 3.1: Comparison of different residual stress measurement techniques [70, 3].

Method	Penetration	Spatial resolution	Accuracy
Slitting	up to 95% of specimen	0.1mm	20MPa
DIC	surface only	0.01mm	comp. to stress-strain data
Hole drilling	hole diameter	$50\mu m$ in depth	± 50MPa
Deep hole drilling	up to 200mm	≤1mm in depth	± 30MPa
The contour method	surface of cut	0.1mm	±30MPa (probe)
X-ray diffraction	50μm (Al)	1mm lateral, $20\mu m$ depth	± 20MPa

The specifications in the table are based on the data given in literature and are a result of experimental analysis. Therefore these values are dependent on the used equipment in each experiment, together with the skills of the operators and often the chosen data reduction techniques.

The hole drilling method is the most widely available method because it only needs strain gauges and a drill. The technique is thus easy implemented, but the low spatial resolution makes it a labour intensive procedure because many specimens have to be prepared to get a sufficient spatial resolution.
Both the deep hole drilling method and the slitting method require an electrical discharge machine and strain gauges. While the slitting method provides a 1D stress profile over almost the entire specimen width, deep hole drilling can only provide a limited amount of 'point' measurements. The advantage however is that a moderately detailed through thickness distribution can be generated, while the slitting method measures the average stress over the thickness.
The contour methods uses an EDM machine and a CCM system. These requirement make, together with the labour intensive data analysis, the method (at this moment) only suitable to specialist laboratories. Furthermore some subjectivity kicks in by choosing the amount of surface smoothing.

By taking all the aforementioned into account the slitting method is selected as the measurement technique to determine the residual stress distribution in the coupons. Slitting relies on proven concepts (strain gauges and EDM) and is relatively fast to implement. The downside is that only one line measurement can be performed per coupon; this adds a constraint to the subsequent fatigue test that is performed on similar coupons: the crack growth path must lie on, or very close to the measured path or a constant stress field must be created perpendicular to the measured line.
Digital image correlation is available at Delft University and is found to be an accurate technique to determine surface strains. Therefore DIC will be used to measure strains during residual stress introduction, from which residual stresses can be calculated. Additionally DIC strain fields will be used to validate a FE model.

The three methods to introduce residual stresses that were left on the short list after initial selection were bending, cold hole expansion and hole yielding. The literature review showed that the residual stress state after cold hole expansion is not uniform in thickness and circumferential direction and that FE modeling is difficult. Therefore this option drops. To make a dicision between four point bending and hole yielding a trade-off will be made based on: (1) FE modeling accuracy and ease, (2) the fatigue testing procedure, (3) slitting data reduction, (4) DIC measurement accuracy, (5) method consistency and (6) experimental labour.
The FE model for yielded holes in a sheet will be simpler then the 4 point bending model but high stresses next to the hole will require a full calibration of the material hardening model. Fatigue testing of the yielded hole will be easier because thin sheets can be used and large scale yielding is not an issue since sheet width is easily increased if so. Slitting is in favour of 4 point bending because the thick coupons that are needed are very stable during slitting and compliance data is already available. DIC measurement cannot be done upto the upper and lower edge of 4pb specimens and close to the hole edge in hole specimens. However, on the rectangular specimens strain gauges can be attached to measure the edge strains and 'fill up the gap'. The consistency of both methods is estimated to be equal; strain gauge measurements during 4pb are more

accurate than during hole yielding but out of plane deformation can occur during 4pb. Finally the labour required to perform the experiments is smaller for sheet overloads since the sheets can be directly loaded in a tensile machine while the 4pb test needs a very accurate setup. The following table summarizes the trade-off in which every category is equally weighted:

Table 3.2: A trade-off between the four point bending method and hole pre-yielding as method to introduce residual stress.

	4 point bending	**hole yielding**
FE modeling	+-	+-
fatigue test	+-	+
slitting reduction	++	-
DIC	+	+-
consistency	+	+
labour	+-	+
total	++++	++

Based on the discussion above, the four point bending procedure is found most appropriate. Therefore rectangular coupons will be plastically bent to introduce residual stress and DIC, strain gauges and slitting will be used to measure the residual stress. This chapter is concluded by answering the research questions, as defined in the introduction of this chapter:

> **1) What is the best method to introduce constant through-thickness residual stresses into a laboratory coupon in a consistent and well-defined way such that subsequently a crack growth test can be performed on this coupon with the crack growing through a compressive and tensile residual stress field?**

Answer: rectangular coupons under four point bending who are fatigue tested in a single edge notched configuration.

> **2) What is the most accurate method to measure the macro residual stress distribution in a metallic laboratory coupon?**

Answer: the slitting method in combination of full field DIC measurements.

In the next chapter the above methods are implemented in a test plan.

Chapter 4

Experimental procedure

This chapter describes the experimental procedure. Section 4.1 gives a general outline of the experiments, section 4.2 contains the tensile and compression test layout. Section 4.3 defines the coupon layout while sections 4.4 and 4.5 contain the details of the bending and fatigue test respectively.

4.1 Overview

A flowchart of the testing procedure is shown in Figure 4.1. Following the right side of the chart, dogbone and cylinder specimens are cut from the base material to measure the elastic-plastic material properties. With this data the residual stresses from bending are derived by FE modeling, slitting and DIC measurements.

Now, following the left side of the chart, several coupons are used to produce baseline crack growth data. The remaining coupons are four-point-bent to introduce residual stress, from which three coupons will be slitted to measure the residual stress. The residual stresses from slitting can now validat the FEM and strain history results. The other coupons are used for the residual-stress-bearing fatigue tests. These tests are then compared to the residual stress free data such that residual stress effects on crack growth can be quantified. In the end, crack growth predictions are varified to experimental results. The following sections provide more details about the different steps in the flowchart.

4.2 Material characterization

The tensile and compressive stress-strain curves are determined with dogbone and cylinder specimens following the ASTM-E8M [99] and ASTME9 [100] test standards. Both tests are strain controlled at a rate of approximately 100μ/sec which is comparable to the strain rate of the outer fibers during four point bending.

In the tensile test, strain is measured with an extensiometer, strain gauges and DIC. The material characterization data is deduced from the extensiometer, the other data is used to varify if the strain gauges and DIC measurements are accurate for later use on four point bending. In the compressive test, strain is measured by two strain gauges positioned at 180° apart on the side of the cylinder because no extensiometer is available at the compression machine. Altough strain gauges are not recommended by ASTME9 because of barelling effects, this effect is expected to be small for ε<1% and slender coupons. Detailed test plans can be found in Appendix B.2 and B.3 respectively.

4.3 Coupon design

The coupon will be made of 50mm thick aluminum 7050-T7451 plate. This aluminum alloy is widely used in aircraft frames and bulkheads because of its good fatigue resistance in thick sections, high strength and excellent corrosion resistance [101]. The T7451 temper means that the plate is solution heat-treated, stress-relieved by controlled stretching (1.5% to 3%) and then artificially overaged (between T73 and T76). Since the parent material is stress-relieved during production the coupons are assumed residual-stress-free

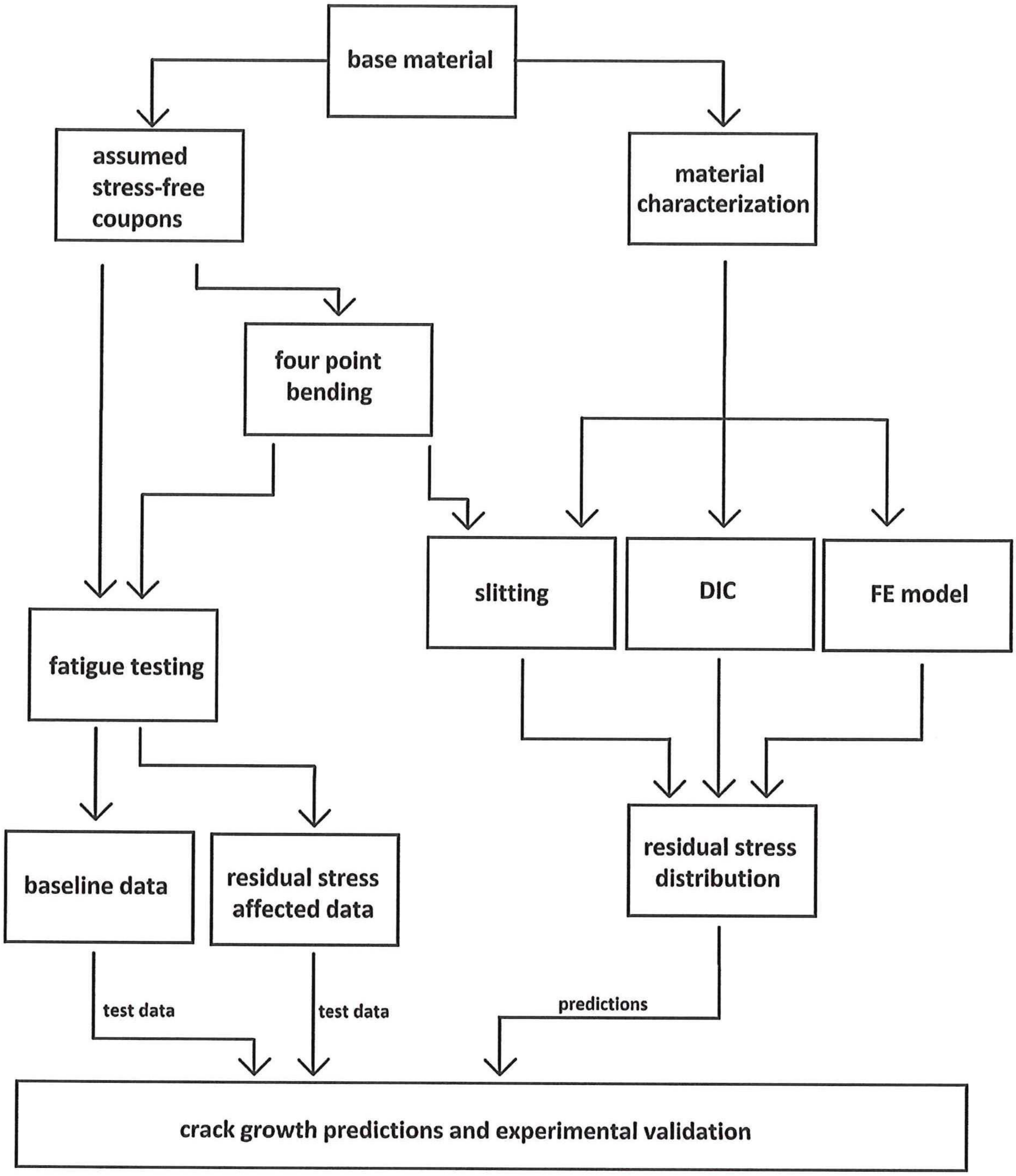

Figure 4.1: Flowchart of the testing procedure.

and will therefore not be annealed. Using as delivered material also allows for validation of results against handbook data.

The chemical composition as in the literature are given in Table 4.1. To check the homogeneity of the base material, several measurements of the chemical constitution were done in the scanning electron microscope (SEM) during the crack surface inspections. It can be seen that the amount of zinc exceeds the limit quite substantially and the amount of magnesium falls short. The most important observation, however, is that the constitution is fairly homogeneous throughout the coupons.

Table 4.1: Chemical constituents (wt.%) of 7050 aluminum [101].

Coupon	Si	Fe	Cu	Mn	Mg	Zn	Cr	Ti	Al
lit.	0.12	0.15	2.0-2.6	0.1	1.9-2.6	5.7-6.7	0.04	0.06	Balance
1	0.06±0.05	0.00	3.02±0.52	0.15±0.1	1.33±0.12	10.01±0.5	0.01±0.07	0.00	85.42±0.26
2	0.05±0.04	0.30±0.1	2.95±0.27	0.00	1.21±0.11	9.78 ±0.46	0.00	0.06±0.06	85.54±0.25

Since in the aircraft industry the L-direction is usuallly oriented parallel to the highest expected load, the fatigue tests will also be performed in this direction. Besides, an L-T orientation gives the lowest chance of preliminary splitting and the most consistent crack growth results [102].

4.3.1 Coupon shape and size

The size and shape of the specimens must be such that they can be loaded into a 4-point bending machine, can be used by the slitting method and can be loaded into a servohydraulic fatigue machine with clamped grips. A specimen size of L=254mm by W=50.8mm fits in the TU Delfts 4pb frame and slitting compliance solutions are also available for this rectangular shape [72]. Furthermore, this geometery makes single edge crack tension SEN(T) fatigue testing possible. In fatigue testing, often other geometries are used such as the compact tension C(T) or middle crack tension M(T) see Figure 4.2. These are, however, not suitable. The compact tension specimen is too small for the 4 point bending frame. It also requires two loading holes to be drilled close to the starter notch. These relatively large holes will cause residual stress redistribution close to the crack path. The middle tension specimen requires symmetrical crack growth to the left and right. The unsymmetrical residual stresses in the specimen will however make crack growth unsymmetrical and thus invalidate the results.

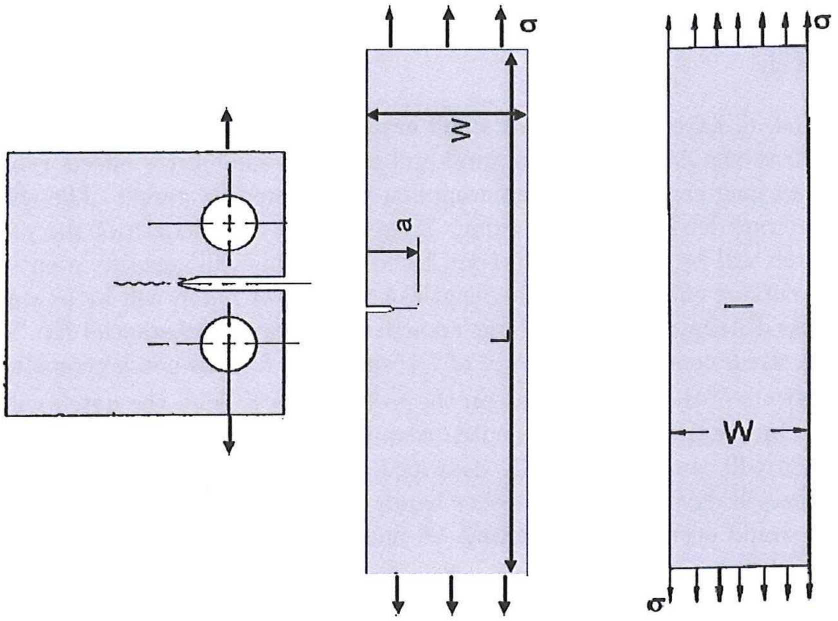

Figure 4.2: Compact tension C(T) left, single edge crack specimen SEN(T) and middle crack tension M(T) specimen (right), modified from [103].

The SEN(T) specimen is thus found most appropriate. The thickness of the specimen is advised in ASTM-E647 to be between $W/20$ and $W/4$, which is equivalent to 2.54-12.7mm, while the bending and slitting operations put no constraints to the coupon thickness (within the bench limits). A thickness of

12.7mm is chosen such that a minimum of out-of-plane deflection is present during bending and thus the residual stress distribution is constant over thickness. Figure 4.3 shows the shape and dimensions of the coupon.

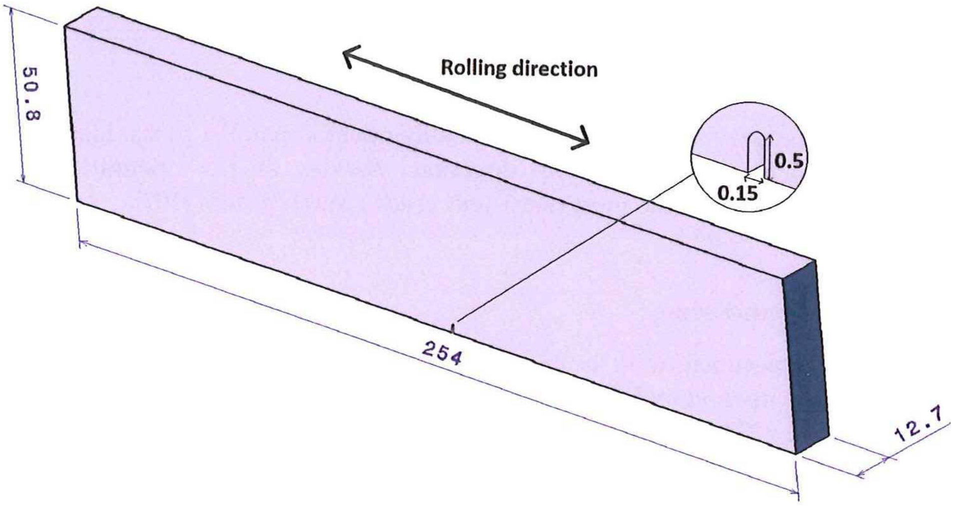

Figure 4.3: Coupon dimensions in mm.

Although it is advantegeous for crack growth tests to have a wide specimen as compared to crack length, a width of 50.8mm is chosen. Preliminary calculations show that a bending force of ±90kN is required to bend this coupon up to 1% out fiber strain, which is near the limits of the available four-point-bending frame.

4.3.2 Starter notch

Several researchers [104, 6] have reported that small cracks do not behave the same as long cracks with respect to crack length versus ΔK. Microstructural and micro residual stress effects typically make small cracks grow faster than long cracks at the same applied stress intensity range. The effects are reported to be present up to a crack length of about 1mm. Therefore the total length of the precrack is at least 1mm. The starter notch will be cut with an 0.1mm EDM wire; this will generate a cut of about 0.15mm width because of overcutting effects [105]. The length of the starter notch will be as small as possible to minimize residual stress distribution, but are large enough to generate a substantial K_t. Therefore a length of 0.5mm is chosen. A stress concentration factor of 7.1 was found for this notch geometry by FE analysis.

To minimize the effects of the starter notch on the residual stress field, the notch will be cut after the bending operation has been performed. If the notch were present at the compressive side during bending, the stress concentration will cause a plastically deformed area in front of the notch tip and consequently tensile residual stresses will develop. On the other hand, if the notch were present on the tensile side of the specimen fracture could occur during bending. A precrack of 1mm is assumed to be sufficient to be out of the notch affected zone.

4.4 Four point bending test

The variables that must be chosen for the plastic bending are the load magnitude and cylinder positions. This must be chosen such that the created residual stress is large enough to measure any effects during subsequent fatigue testing but small enough to prevent too large compressive stresses (through which cracks will not initiate), excessive plastic yielding and specimen curvature.

Table 4.2: Residual stress magnitude in longitudinal direction for increasing bending strains.

s	Extreme fiber strain [$\mu\varepsilon$]	σ_s [MPa]	σ_p [MPa]	Peak depth [mm]	Load [kN]	δ [mm]
1.0	6643	0	0	25.4	73	1.20
1.5	9964	129	69	16.9	93	1.54
2.0	13286	174	145	12.7	100	1.65
2.5	16607	195	201	10.2	103	1.71
3.0	19929	207	241	8.5	105	1.74

4.4.1 Residual stresses after plastic bending

Residual stress distributions for different levels of extreme fiber strain were given in Figure 3.13. The values of the accompanying extreme fiber strain, and maximum required load are given in Table 4.2. It can be observed that the stresses increase with increased bending force and the internal peak shifts towards the neutral axis. These calcuation come from an elastic perfect-plastic material assumption and beam theory. The last column shows the expected mid-deflection from initial finite element calculations. This is used to select a deflectometer with sufficient range.
It can be seen that for an outer fiber strain of 9964$\mu\varepsilon$ the surface residual stress is 129MPa and the interneal peak 69MPa. The residual stress magnitude of 129MPa at the surface is large enough to distinguish residual stress effects from experimental scatter [49]; therefore a value of 10.000$\mu\varepsilon$ is selected as target bending strain.

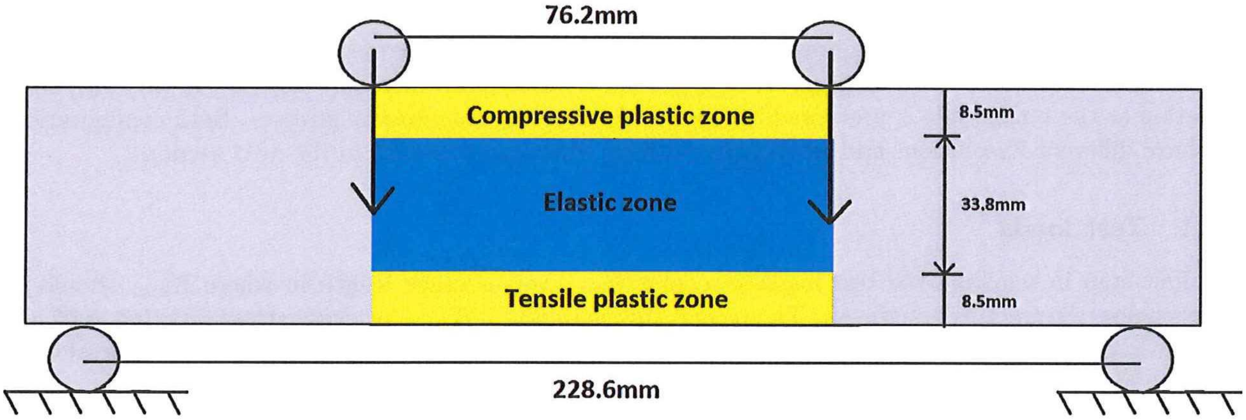

Figure 4.4: Schematic of the bending setup. The tensile and compressive plastic zones are indicated in yellow, the blue section remains fully elastic.

The loading points will positioned at 76.2mm apart (Figure 4.4) such that an as close to perfect bending moment is introduced in the specimens. Placing the upper cylinders further apart would increase the required forces to generate the same bending moment and increase shear effects. Positioning them more inwards can give plasticity effects from cylinder indentations near the crack path.

4.4.2 Strain measurements during four point bending

During 4 point bending, strain gauge measurements and DIC pictures will be taken. One strain gauges is glued on top of the specimen, another one is glued at the bottom to determine outer fiber strains. At the coupon neutral axis, strain gauges are placed on both sides to determine the quality of the bending. DIC measurements are taken over the full coupon heigth between the inner contact points. From this area the midline strains can be obtained. DIC measurements do not go completely up to the specimen edge; strain gauge data and DIC data are used to complement each other.

To summarize, the four point bending tests will be carried out as in schematic 4.4 with a target outer fiber strain of 10.000$\mu\varepsilon$. The applied force will be close to 93kN and the residual stress will have a maximum of 129MPa at the edges and internal peaks of 69MPa. Strain gauges and DIC are used to measure outer fiber strain and the strain distribution over the coupon heigth. Strain gauges on the left and right surface are used to detect out-of-plane bending.

4.5 Crack growth tests

Residual stress effects on crack growth are quantified by testing both stress bearing and stress free specimen. To investigate the effects of residual stress on crack growth as much unknown parameters as possible must be eleminated. To eliminate crack 'history' effects all tests are performed at constant amplitude loading and at loads as close as possible to each other. Although the constant amplitude test is not completely history independent - K is increasing during the test - K-values are increasing at approximately the same rate in each coupon. Therefore no crack history effects are expected in the upcoming tests.

To make a direct comparison between residual stress and stress-free specimens the applied forces are kept equal for each loading ratio. The applied forces and ratios must be selected such that a wide range of ΔK is tested without violating the small scale yielding criterion. Furthermore the applied ΔK must be roughly equal to ensure that $\frac{da}{dN}$ lie within the same range for each configuration.

As discussed in the previous section the specimen top side will be in residual tension, while the bottom is in compression. To quantify both the tensile and compressive stress effects, coupons are tested with the crack initiating at the tensile side and are tested from the compressive stress side. Crack initiation at the tensile side willl not give problems in the SEN(T) configuration; the residual stress promotes crack initiation and growth. At the compressive side however, large applied stress will be needed to initiate and grow a crack. Therefore these coupons are fatigued under three-point-bending: SEN(B). In this way, crack initiation at the tensile side is prevented because of the bending compressive stresses. Both configurations will have different K-solutions and small scale yielding behavior, as shown in the next sections.

4.5.1 Test loads

The first step in selecting the test loads is to plot K_{max} versus crack length in where K_{max} should be always below the fracture toughness. The second step is to find a K_{max} for every stress ratio 0.7, 0.05 and -1 such that the applied ΔK are roughly equal. Stress ratios of 0.7 and -1 bound the total stress ratio R_{tot} for residual stress bearing coupons tested at R=0.05.

The test matrix that has been used for the fatigue tests is shown in Table 4.3. The next sections show how these test loads are derived. K_{max}, plastic zone size and remaining ligament stress for the most heavily loaded coupons to determine the limits of small scale yielding (SSY). To do this, first the K-solutions are presented and SSY calculations are given.

4.5.2 K-solutions

For both configurations a K-solution has to be found that includes the correct boundary conditions. For the residual stress intensity factor a weight function solution is used.

4.5.2.1 SEN(B) solution

The three-point-bending SEN(B) solution is simply given in Tada et al. [106] as:

$$K_I = \frac{6P}{BW}\sqrt{a}F(\frac{a}{W}) \tag{4.1}$$

with

$$F(\frac{a}{W}) = \frac{1.99 - \frac{a}{W}(1-\frac{a}{W})(2.15 - 3.93\frac{a}{W} + 2.7(\frac{a}{W})^2}{(1+2\frac{a}{W})(1-\frac{a}{W})^{3/2}} \tag{4.2}$$

Table 4.3: Fatigue test matrix. Applied stress is the maximum gross section stress for SEN(T) and the maximum tensile outer fiber stress for SEN(B).

coupon	σ_{min} [MPa]	σ_{max} [MPa]	R	residual stress	configuration	note
C1	1.55	31.00	0.05	-	SEN(T)	failure at grips
C2	2.71	54.25	0.05	-	SEN(T)	non-symmetric crack growth
C8	2.71	54.25	0.05	-	SEN(T)	-
C3	59.68	85.25	0.7	-	SEN(T)	-
C4	-54.25	54.25	-1	-	SEN(T)	-
C5-B3	2.71	54.25	0.05	tensile	SEN(T)	-
C6-B5	6.45	120.9	0.05	compressive	SEN(B)	non-symmetric crack growth
C7-B6	6.45	120.9	0.05	compressive	SEN(B)	non-symmetric crack growth
C9-B9	2.71	54.25	0.05	tensile	SEN(T)	non-symmetric crack growth
C10-B8	-54.25	54.25	-1	tensile	SEN(T)	-
C11-B10	59.68	85.25	0.7	tensile	SEN(T)	-

where P is the applied load, B and W are specimen thickness and height respectively and a is the crack length. This equation is claimed to be accurate within 0.5% for any a/W.

4.5.2.2 SEN(T) solution

In the SEN(T) configuration the specimen is fully clamped on both sides. This clamping prevents any end rotation of the specimen at the grips which results into a non-uniform stress distribution over the specimen width, even though a uniform displacement is applied. If the simple closed form uniform end-stress solution is used, the stress intensity calculations will produce too large stress intensities. A more precise solution is thus required.

The solution by Ahmad et al. [107] combines the pin-loaded end solution and the pure bending solution [106] such that the end rotation is zero, see Figure 4.5.

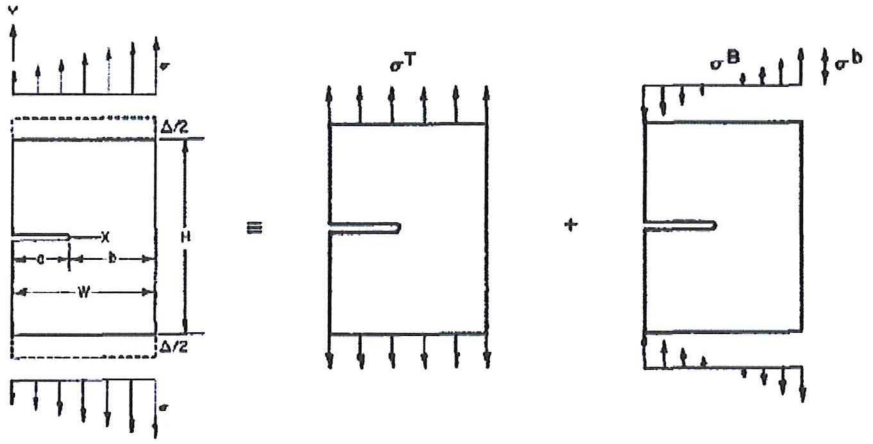

Figure 4.5: Linear superposition of tension and bending stresses to determine remote stress corresponding to uniform applied displacement. Modified from [107].

The solution is valid for any height over width ($\frac{H}{W}$) larger than one and for all crack depths up to $\frac{a}{W} = 0.95$ and is therefore used to calcuate K due to the applied loading for all SEN(T) specimens. The solution is presented as an addition of two fitted functions, from which the second function is activated by a Heaviside function for $\frac{a}{W}$>0.6. This second equation however, seems not be be fitted correctly, and gives a jump in the K-solution. Fortunately this will not affect any analysis in this thesis since only crack of length a<0.5W are considered (as will turn out, shear lips will start to grow at this crack length).

4.5.2.3 K_{res} solution

The residual stress intensity factor K_{res} cannot be obtained with the aforementioned solutions because these do not allow for random stress distributions over the crack plane. The common approach to calculate K_{res} is the weight function method [58] given by

$$K = \int_0^a \sigma(x)h(x,a)dx \tag{4.3}$$

where $\sigma(x)$ is the arbitrary (residual) stress distribution on the crack surface, a is the crack length, x the crack coordinate and $h(x,a)$ the weight function which is load-independent but geometry-dependent. In the analysis here, the weight function solution by John et al. [108] is used to calculate K_{res}.

This weight function is derived as:

$$h(x,a) = \frac{E'}{K_r}\frac{\partial v_r(x,a)}{\partial a} \tag{4.4}$$

where a is the crack length, $E' = E$ for plane strain and $E/(1-v^2)$ for plane stress, v is Poisson's ratio and v_r and K_r are the crack tip opening and stress intensity factor under the reference condition of constant applied stress. According to the method of Wu and Carlsson [57] v_r was assumed to be a forth order series expansion. The four constants were determined from (1) the reference K-solution, (2) self-consistency (inserting the σ_r in Equation 4.3 should give K_r back), (3) zero curvature at crack mouth and (4) crack mouth opening displacement from v_r.

The reference solution was obtained by an FE model containing eight-noded quadrilateral elements and quarter point singular elements around the crack tip. K was computed from the crack tip quarter point displacements. The accuracy of the finite element mesh was verified by simulating the pin-loaded end condition with constant stress. The K values from the finite element analysis were within 1 percent of the handbook solution by Tada [106].

This weight function is valid for coupon height over width, $\frac{H}{W} = 4$ only, while the coupons in this thesis will be tested at $\frac{H}{W} = 3$. In a later paper [109], John presented solutions for every aspect ratio between 1-10. To convert from the solution of $\frac{H}{W} = 4$ to that of $\frac{H}{W} = 3$ a simple correction function was provided which is shown in Figure 4.6 together with the non-dimensionalized K-solutions for $\frac{H}{W} = 4$ and$\frac{H}{W} = 3$. It can be seen that both solutions start at the semi-infinite plate solution of $K = 1.1215$ but diverge quickly as the crack length increases.

As effective stiffness, E', a value of 1.013 is taken, which means that the plane stress solution from John et al. is increased by 1.3%. This value is determined by Aydiner [110] as the 3D-constraint factor for slitting reduction. It is hereby assumed that the plane-stress/plane-strain effect is equal in slitting and crack growth.

Now the K-solutions and the residual stress intensity factors are known, $K_{max,total}$ can be plotted to check when the fracture toughness will be exceeded. Figure 4.7 depicts $K_{max,total}$ versus crack length for the most heavily loaded specimens.

4.5.3 Small Scale Yielding

In order to let LEFM valid, the small scale yielding criterion must be obeyed throughout the complete test. The criteria that are applied here are 1) the remaining ligament stress shall not exceed 80% of the material yield stress (=0.8*400MPa=320Mpa) and 2) the plastic zone size shall not be larger than 10% of the coupon thickness (=1.27mm). The plane-stress (conservative) plastic zone size is estimated by the following equation [7]

$$r_p = \frac{1}{3\pi}\left(\frac{K_{max}}{\sigma_{yield}}\right)^2 \tag{4.5}$$

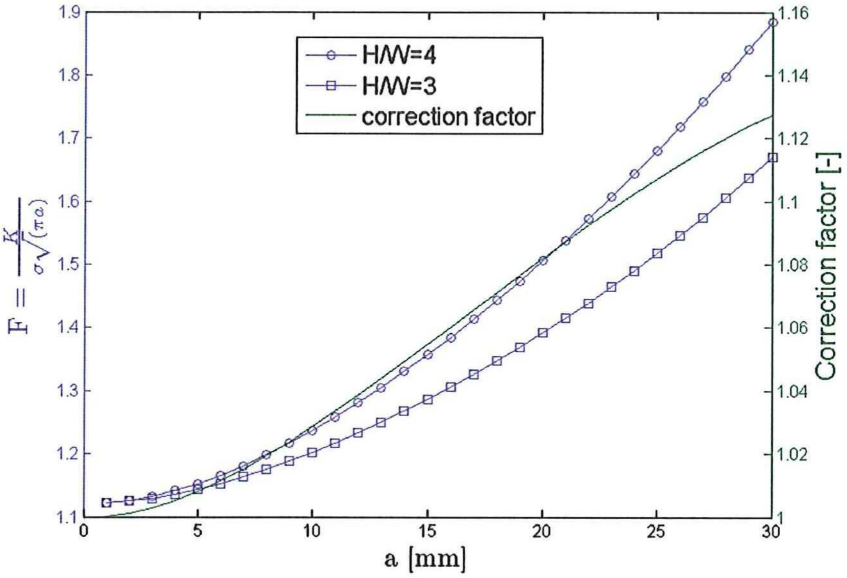

Figure 4.6: The non-dimensionalized stress intensity factors for a SEN(T) specimen clamped at different ratios (left axis). The correction factor to convert between the two solutions is shown on the right axis.

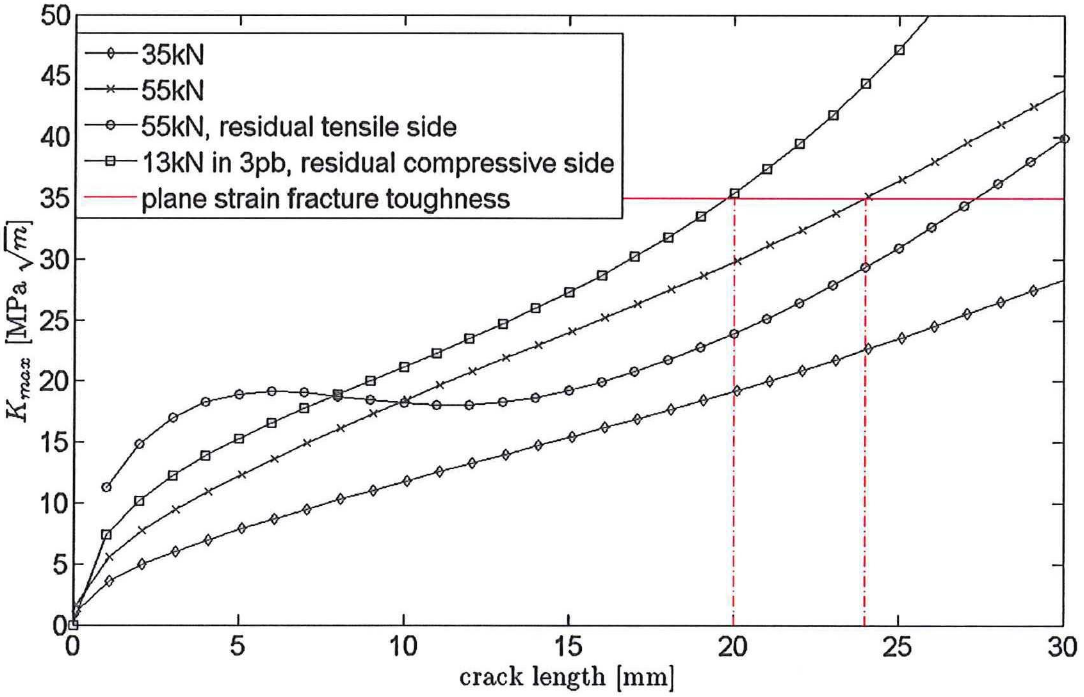

Figure 4.7: K_{max} is plotted against crack length for the most serverely loaded coupons. Coupons C5 and C6 (13kN, 3 point bending) will fracture at 20mm crack length. Coupon C3 (55kN) will fracture at 24mm crack length. Testing from the residual tension side increases possible crack length.

For the SEN(T) coupons the plastic zone size is obtained by setting K_{max} as $K_{applied} + K_{res}$. The remaining ligament stress is taken as the maximum tensile residual stress present before the crack plus the stress due to applied loading. Figure 4.8 shows the remaining ligament stress and reveals that coupons C6 and C7 are limited to 18.1mm crack length; for the other coupons no large scale yielding occurs.

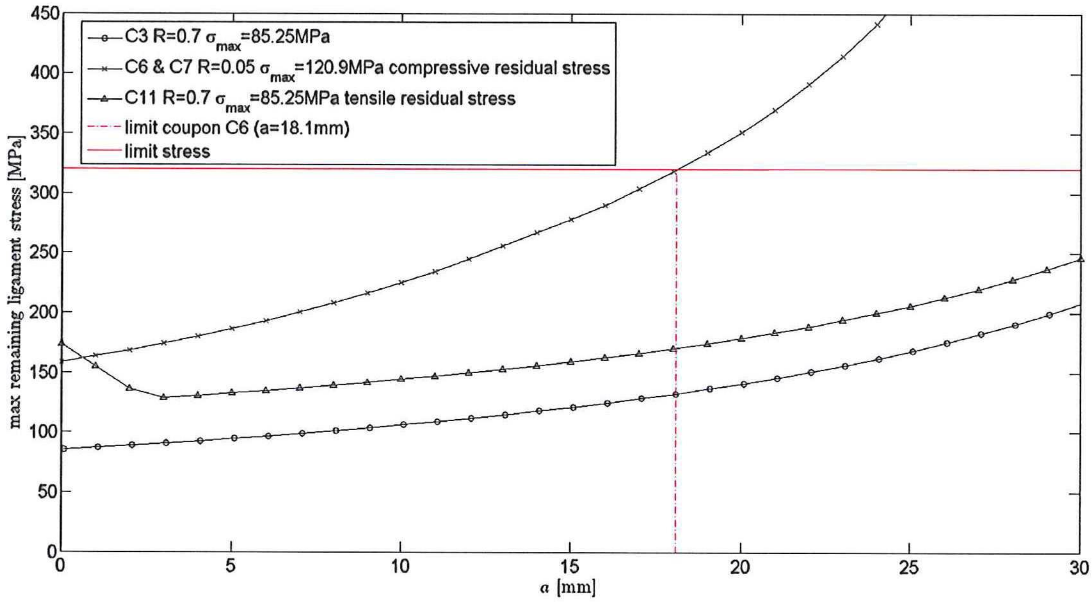

Figure 4.8: Remaining ligament stress for coupons C3, C6 and C11.

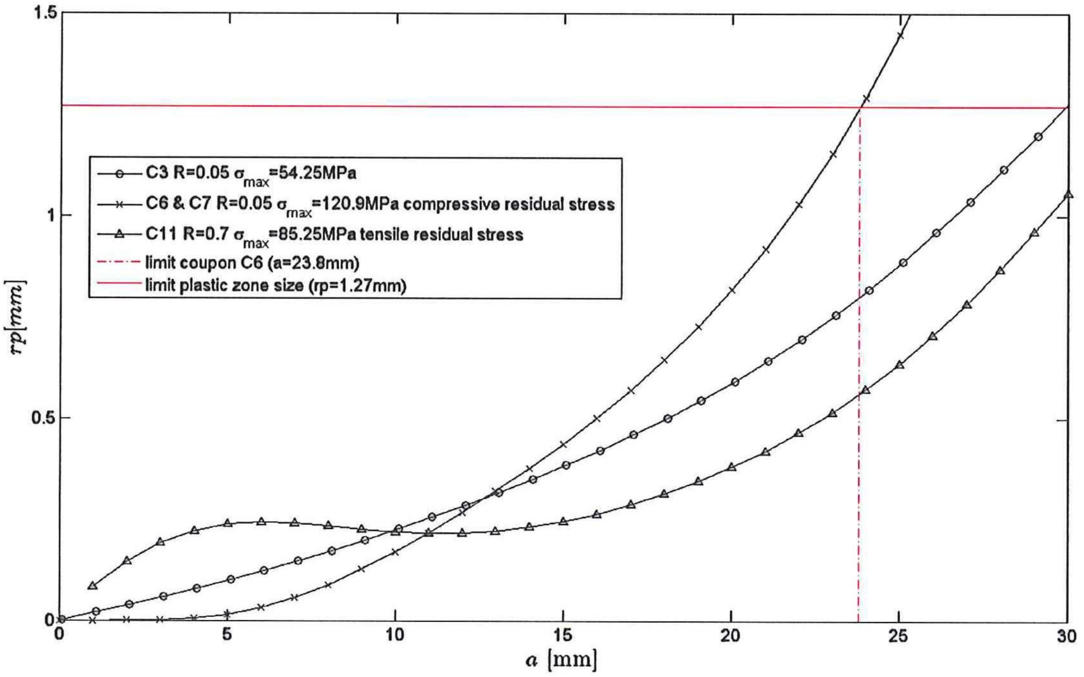

Figure 4.9: Crack tip plastic zone size for coupons C3, C6 & C7 and C11.

Figure 4.9 shows that due to crack tip plasticity, coupons C6 and C7 would be limited at 23.8mm since here the crack tip plastic zone exceeds the limit. This limit is however less restrictive then that of the remaining ligament stress. Again, coupons C3 and C11 do not suffer from large scale yielding up to 30mm.

In conclusion, the only coupons that are limited in crack length below 24mm are coupon C6 and C7; the maximum crack length is 18.1mm. All other coupons can be tested up to at least 24mm.

Chapter 5

Test results

This chapter contains the results from the material characterization in Section 5.1, four point bending in Section 5.2, slitting in Section 5.3 and finally Section 5.4 gives the crack growth results.

5.1 Material characterization

The aluminum 7050-T7451 material has been characterized according to Appendix B.2 and B.3. The test setup including all measurement devices of the compression and tension test is shown in Figure 5.1.

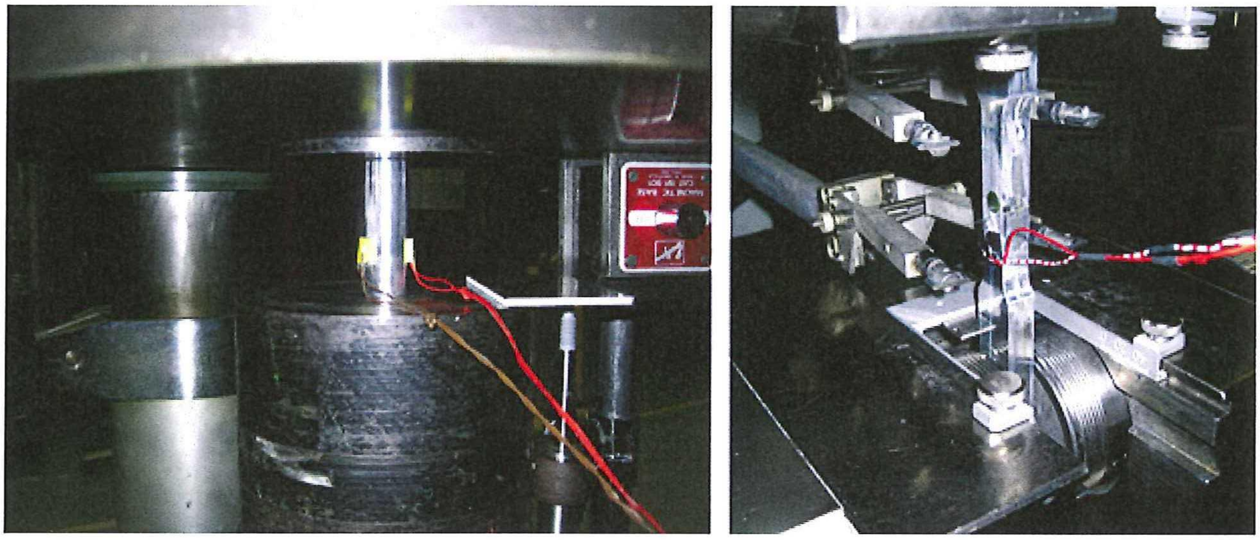

Figure 5.1: Setup for the compression test showing a clamped cyclinder (left) and the tensile test with a hydraulically fixed dogbone specimen.

The stress-strain data is shown in Figure 5.2. Only the first 1% strain is shown because this is the range of interest for the bending test. Both data sets are obtained from one single specimen. A second compression tests showed very consistent results but was not useful because stress relaxation occured during the test when it was shortly interrupted to take a picture.
The elastic moduli are determined by a least square linear fit over the lower 200MPa. The compressive modulus turns out to be 2.6% higher then the tensile modulus. Table 5.1 summarizes the most important results.

5.2 Four Point Bending results

This section contains the strain gauge and DIC results from the four point bending tests, as specified in Appendix B.4. In section 5.2.2 both methods are varified against each other.

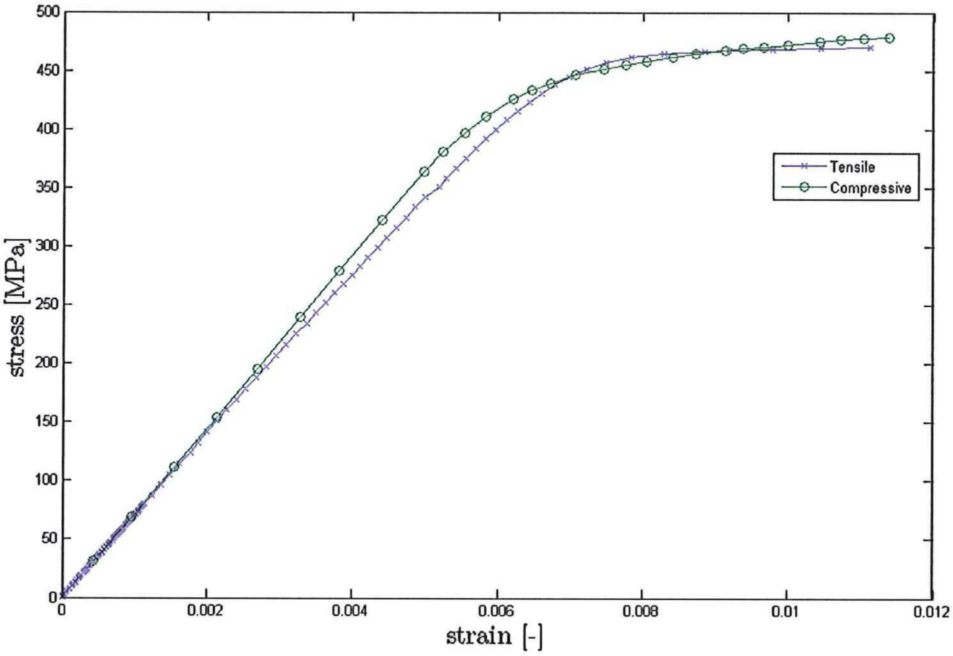

Figure 5.2: Stress-strain curves in tension and compression for 12.7mm thick Al7050-T7451 plate.

Table 5.1: Al7050-T7451 measured material properties.

Al7050-T7451	E-modulus [GPa]	$\sigma_{yield}[MPa]$	$\sigma_{0.2\%yield}[MPa]$	Poisson's ratio
Tension	70.2	±450	466	0.33
Compression	72.4	±375	462	

5.2.1 Experimental procedure

An overview of the four point bending setup is given in Figure 5.3.
The coupons were positioned between the cylinders with a specially designed device to ensure symmetric and perpendicular positioning. Small steel blocks were glued to the specimens at the contact points to reduce the plastic indentations and friction. After applying a small load to hold the specimen in place the zero measurement was taken.

The bending force was now increased manually. By monitoring the force in real time, every 2kN a measurement was taken. Because the strain could not be monitored in real time the tests could not be performed up to 10.000$\mu\varepsilon$ exactly. However, after the first strain reading above 10.000$\mu\varepsilon$ the test was ended and load reduced to zero in steps of 4kN.

5.2.2 Bending strain results

Table 5.2 summarizes the strain at maximum load and after unloading for the top and bottom strain gauges together with a maximum load. The first column shows that the target strain of 10.000$\mu\varepsilon$ was approached very closely. Specimen B2 was tested in transverse grain direction and shows a difference of 686 microstrain. The average compressive strain at maximum load is 341$\mu\varepsilon$ smaller than the tensile strain. The third and fourth columns show that the compressive residual strain after springback is however larger than the tensile residual strain.

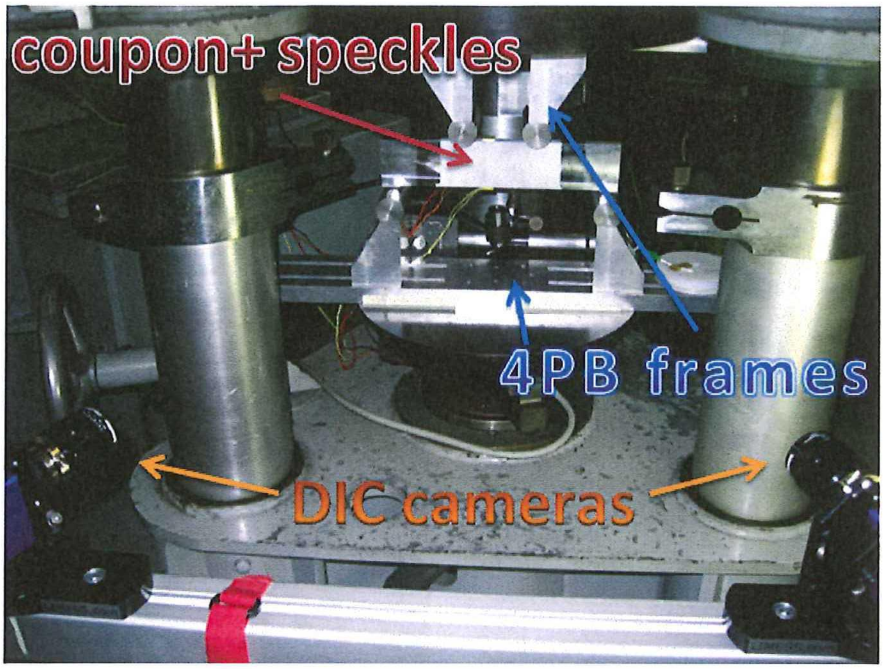

Figure 5.3: Overview of the bending setup.

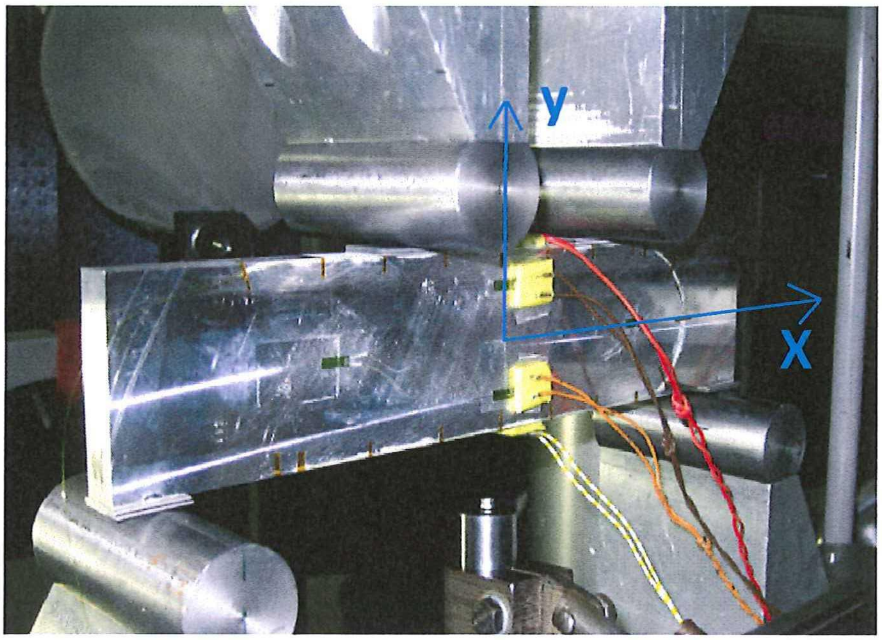

Figure 5.4: Close-up of coupon B2 showing three strain gauges and the axes for positioning the gauges.

DIC measurements were taken together with every strain gauge measurement to compare both results. Two 4 Megapixel cameras were used to capture the images and VIC3D software was used to analyze the pictures. The cameras were set up such that one speckle was captured by approximately 3 pixels. All analyses were done with a subset size of 21 pixels and a step size of 10 pixels. Taking smaller subsets captured too much noise.

Figure 5.5 shows the stain distribution in X-direction for coupon B3 at maximum load (left) and after springback (right). The other specimens show a very similar behaviour and are therefore not shown.

Several important conclusions can be drawn from these figures. First observation is that the deformation at the contact points does not influence the strain distribution at the midspan and that the strain field

Table 5.2: Top and bottom strain gauge results for coupons B2-B10. B1 and B7 failed. Strain shown at maximum load and after springback. Strain in microstrain.

coupon	loaded ε_{max}	loaded ε_{min}	unloaded ε_{max}	unloaded ε_{min}	max applied load [kN]
B2	10125	-9439	1493	-1294	90.82
B3	10024	-9503	1429	-1361	89.2
B4	10117	-9677	1465	-1515	88.29
B5	10004	-9618	1418	-1424	88.5
B6	10056	-9661	1395	-1385	88.85
B8	10123	-9942	1531	-1640	89.87
B9	9971	-9752	1400	-1534	88.89
B10	9994	-9744	1418	-1529	89.86
average	**10041**	**-9700**	**1437**	**-1484**	**89.07**

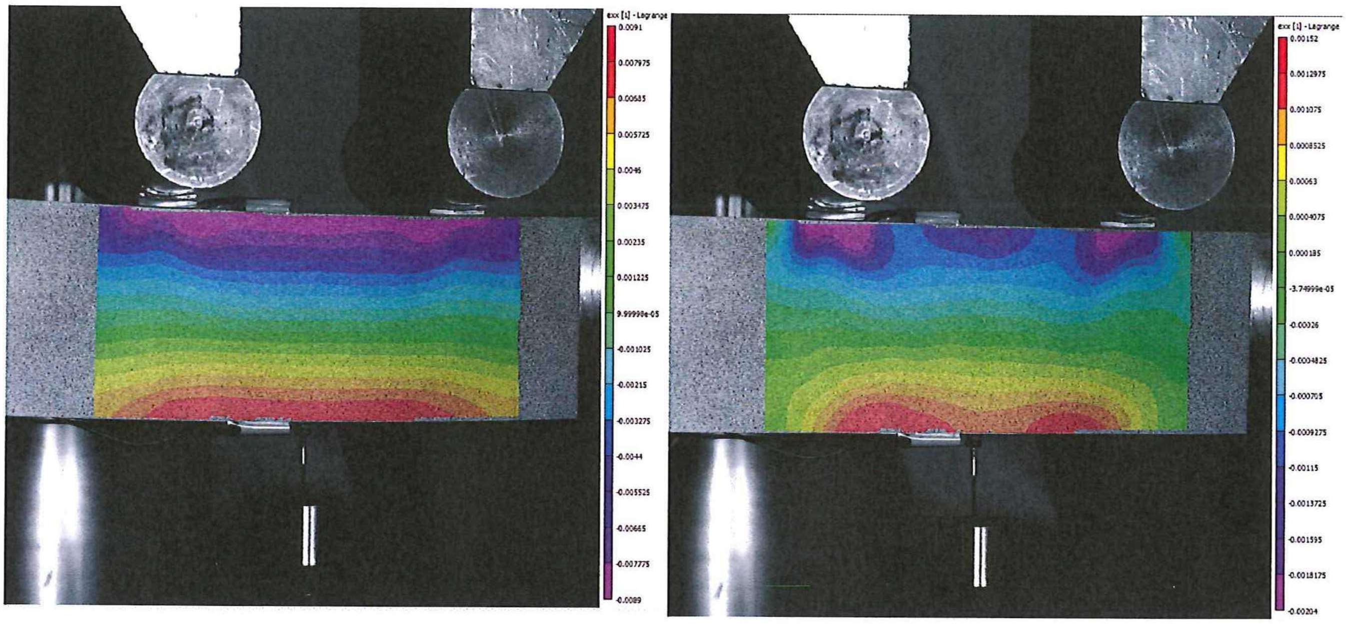

Figure 5.5: DIC result of coupon B3 showing ϵ_x at max load (left) and after springback.

is close to symmetrical. This latter proves that the load has been applied symetrically (i.e. both loading cyclinder apply equal force). Secondly the equistrain lines are almost perfectly horizontal and parallel, this proves that there was very little out of plane bending.

By knowing this, the strain over the midline of the coupon can be plotted together with the strain gauge data. The strain distribution over the width for coupons B2-B6 is plotted in Figure 5.6. The strain gauges are represented by the filled dots and the DIC by the lines. Both data sets coincide good, except for SG3 of coupon B2. It shows that the DIC strain distribution is linear between Y=20mm and Y=-20mm and more non-linear towards the ends. This non-linearity is an edge effect of the DIC analysis and can be reduced by decreasing the size of the smoothing filter or step size but on the other hand this also increases noise. The same non-linearity was seen if a smaller area of interest was selected (for example between Y=-15mm and Y=15mm) even though this gives a linear distribution in the original outcome. Therefore the non-linear parts of the DIC lines are neglected and it is proven that the strain distribution is linear over coupon height.

The DIC data shows that the neutral axis lies slightly below the specimen middle at both maximum load and after springback. This is in agreement with the strain gauge data from all coupons at the midline, which shows compressive strain and thus the neutral axis lying below the middle. This is surprising since the E-molulus of the aluminum is higher in compression than in tension and thus the neutral axis should shift up, instead of down. A possible explanation for this is that due to coupon curvature, the lower contact cylinders are pushed outwards, which creates an inward compressive force in the coupon and shifts the neutral axis down. This was not further investigated.

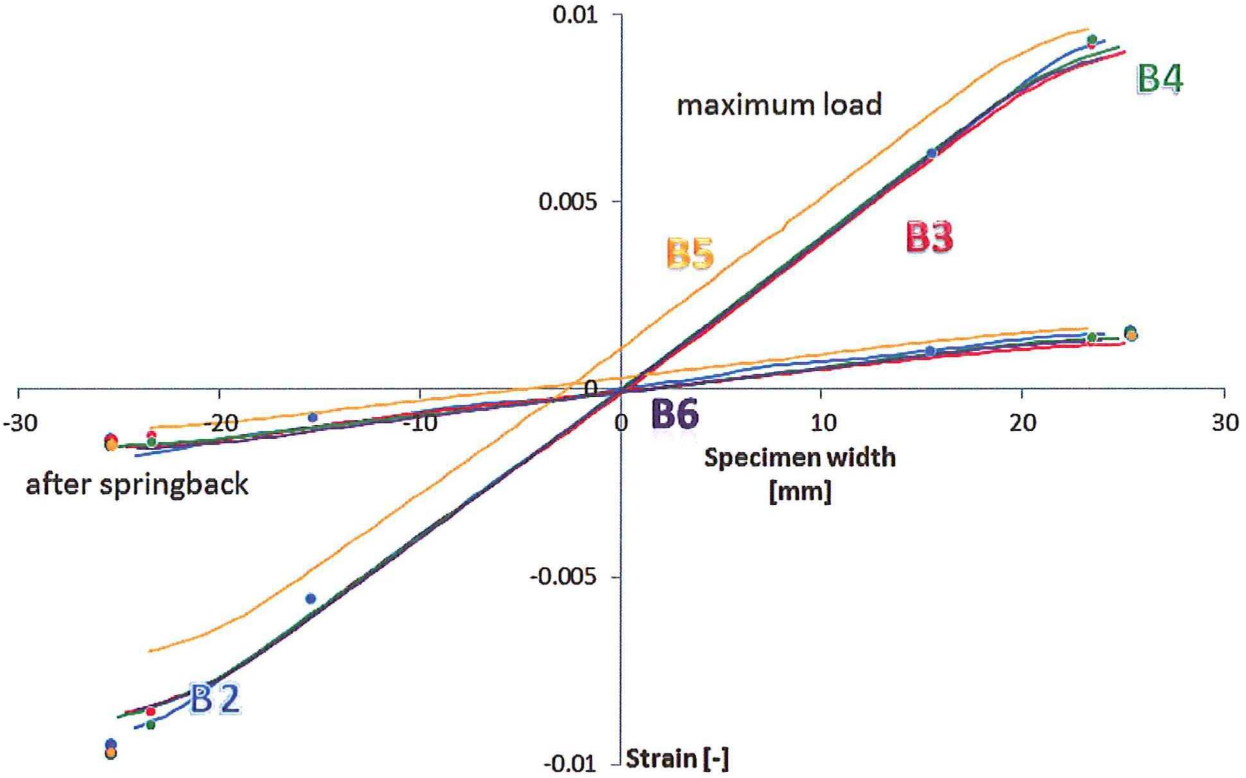

Figure 5.6: Bending strain distribution over coupon width at maximum load and after springback.

By zooming on the unloaded strain distributions one can see the variation more clearly (Figure 5.7). Coupon B2 shows a more wavy strain distribution then the other coupons because the DIC data was analysed with a smaller subset which gives more noise. Coupon B2 therefore also shows less non-linearity at the ends in Figure 5.6.

The variation in maximum between coupons B3-B10 is 0.5% at the tensile side and 1.2% at the compressive side. After springback the average difference from the mean is 2.6% at the bottom and 6.4% at the top. These larger differences after springback are explained by material variability, scatter in friction and the fact that the absolute errors stay constant, but the relative errors are larger for the unloaded case.

To conclude, by four-point-bending a constant strain distribution between the loading points can be achieved. Three dimensional DIC is an effective method to measure the strain distribution in the area of interest, with exeption of the coupon edges. The DIC proved the strain distribution to be linear over the width, therefore only two strain gauges are sufficient to obtain the full strain distribution from interpolation.
For this particular coupon and bending configuration, an average difference from the mean of 0.5% in tension (which was the strain controlled gauge) and 1.2% in compression gives a variation of 2.6% and 6.4% respectively after springback. This does however not mean that the residual stress distribution suffers from the same amount of variation, as can be seen in the following chapter.

5.3 Slitting results

Coupons B1, B2 and B4 were selected for slitting. B1 was used for practice, which came down to checking for slit closure, setting the Peekel strain amplifier to the highest sensitivity without going out of its range,

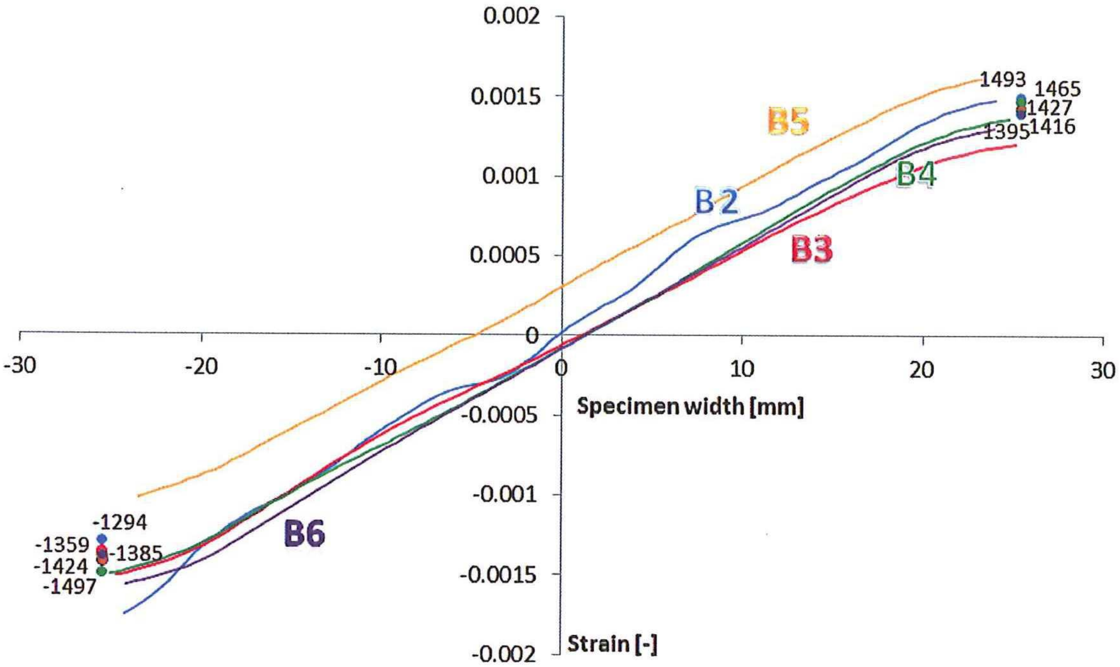

Figure 5.7: Residual bending strain distribution over coupon width.

determine cutting speed and voltage to obtain a nice cut, etc. Coupons B2 and B4 were expected to have almost equal residual stress distributions and are therefore used to check repeatability of the slitting method and to varify residual stresses as determined from the bending strains.

The cutting was done on a Fanuc α-CiA EDM wire cutting machine at a speed of 1mm/min and wire thickness of 0.25mm. All specimens were one-end fixed and aligned up to 0.05mm/m in the horizontal and vertical plane. Figure 5.8 shows the setup with the coupon clamped in the machine. Before cutting, the zero cut depth was set by just making contact to the edge of the specimen. For further details of the slitting experiments, see Appendix B.5.

Measurements were taken at every 1mm slot increment whereas a spacing of 0.5mm was used during the first and last 5mm of the cut. This was done to obtain a higher resolution where high stress gradients (peaks) were expected from initial calculations. At the end of each cutting increment the wire was kept fixed in position with the power running for 5 more seconds before shutting down the machine. In this way, a consistent overcut size was created at the end of each increment.

After every 5mm cut increment the slit was checked for closure. For both coupons the minimal slit thickness was about 0.15mm at a slit depth of 49mm which means that the residual stresses closed the slit by 0.1mm at most.
The measured strain for both coupons at each slit increment is plotted in Figure 5.9. It can be seen that the strain gauge was initially in compression and makes a transition to tension. This is expected since the cut was started at the tensile residual stress side. A second observation is that the magnitude of strain increases with slitting depth, which is due to an increased compliance of the coupon as the slit gets larger. The residual stress analysis of the two measurements can be found in section 6.1.2.

5.4 Crack growth results

In this section the experimental results of the crack growth tests are reported. Several residual stress-free test were performed to produce base line data. Residual stress bearing coupons were tested from the tensile and compressive residual stress side.

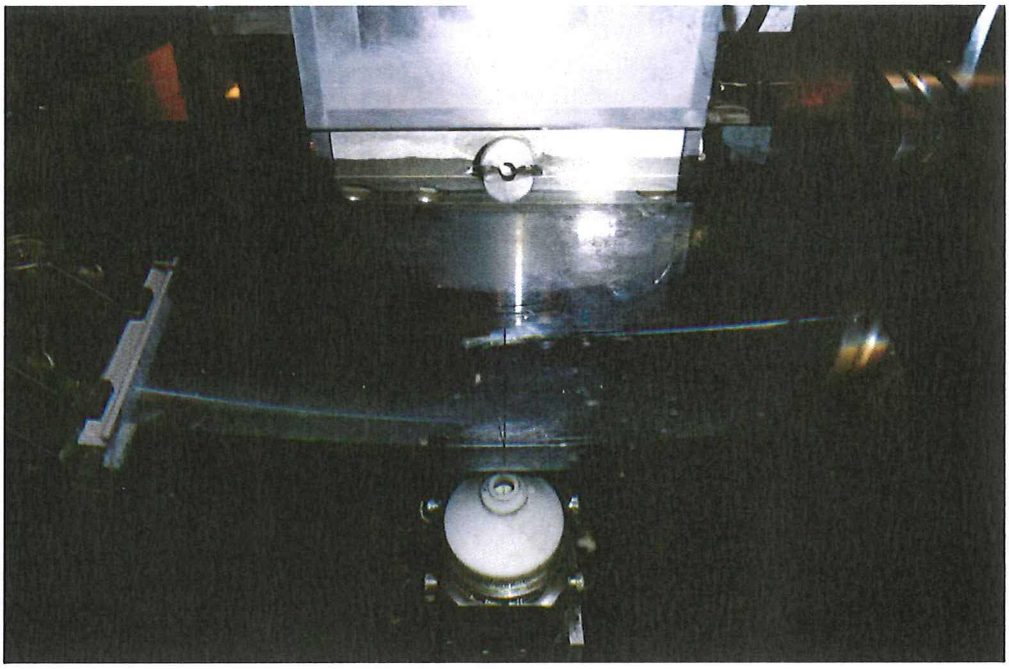

Figure 5.8: Overview of the slitting setup with the specimen clamped on the left. Strain gauge is mounted at the far side of the coupon, reading device not shown. Note that the coupon appears curved due to water diffraction.

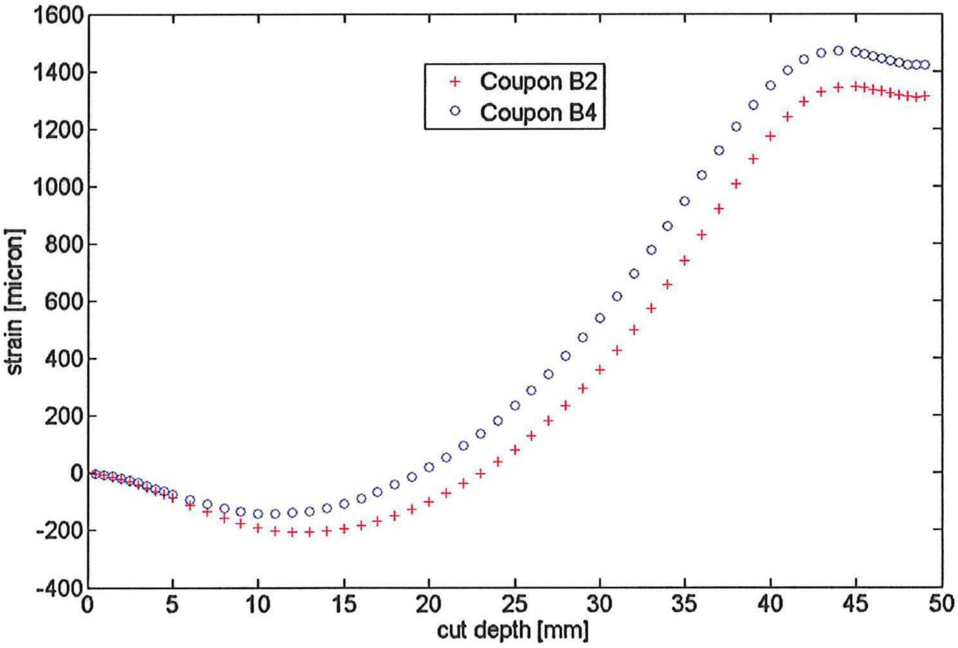

Figure 5.9: Back side strain per slit increment for coupons B2 and B4.

5.4.1 Methodology

All coupons were tested in the single edge notch configuration as indicated in Table 4.3. TU Delft's 100kN and a 60kN servo-hydraulic fatigue machines were used, depending on availability of the machines. The residual stress-free coupons and the coupons with a crack starting at the tensile residual stress side were tested in the SEN(T) configuration. The coupons with a crack started at the compressive residual stress side were tested in a SEN(B) configuation to avoid yielding in the coupon (see section 4.5).

Before specimen installation, the anticipated crack path was polished to enhance crack length measurements and 1mm thick aluminum 6xxx tabs were glued on the coupons to prevent failure at the grip area. This was done because coupon C1 showed failure at the grips due to fretting. The front and back side crack length was measured with two digital microscope camera's. Crack initiation was monitored at a magnification of approximately 200x until a crack length of about 2mm was reached. Thereafter the magnification was reduced to approx. 30x to monitor further growth.

The conditions for all tests was room temperature (20°C-28°C) and a relative humidity between 50% and 90%, while the sinusoidal force signal was kept at 25Hz for the major part of the crack growth. Only at the very ends of the tests this frequency was reduced to 5Hz because it took about 2sec to reach maximum force amplitude after each crack length measurement.

The SEN(T) coupons were clamped in hydraulic grips of 45mm width, the maximum available grip size. This is slightly less than the coupon width (50.8mm) but it is assumed here that the applied stress is completely homogenized as it reaches the coupon midline. Both ends of the coupon were inserted in the clamps by 51mm resulting in an effective length of 152mm (h/W=3). Figure 5.10 (left) shows how the SEN(T) coupons were installed in the machine.

The SEN(B) coupons were installed in a three point bending fixture as shown in Figure 5.10 (right). The lower frame was clamped in the servohydraulic machine, while the upper loading nose was directly taped to the machine. The lower span yielded 203.2mm, which is four times the specimen width. The coupon was aligned on the lower noses and kept in position purely due to friction during the fatigue test.

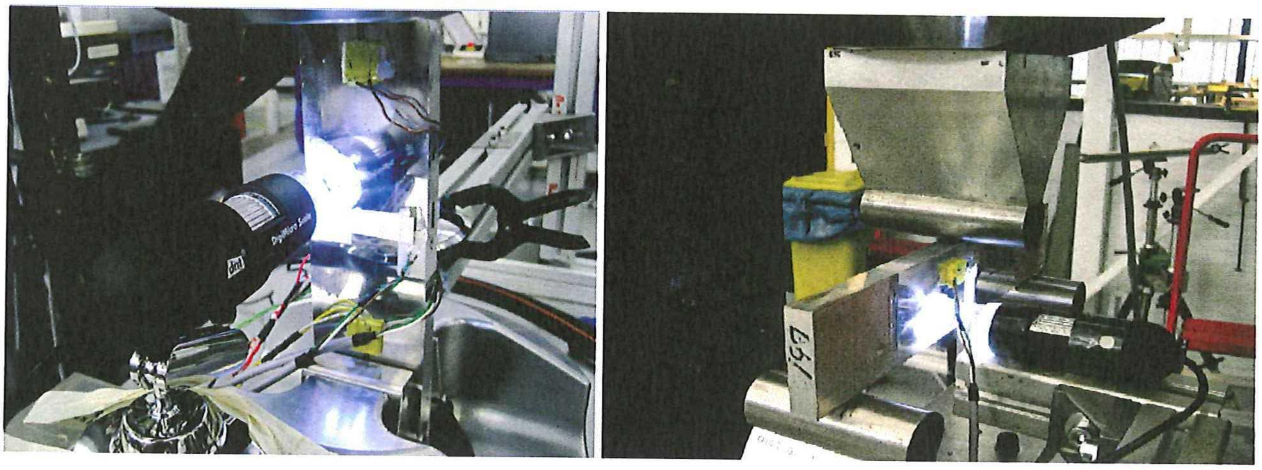

Figure 5.10: Setup of the fatigue tests showing the polished coupon, hydraulic clamps, digital microscope camera and strain gauges. Starter notch is on the left in SEN(T) and on the bottom in SEN(B) and is not visible.

5.4.2 Precracking and crack growth

This section contains the crack growth results. Reporting is done in chronological order to show the evolution of the test process due to failures and necessary adaptations.

5.4.2.1 Coupon C1, baseline R=0.05

Because the EDM wire machine was not available before test C1 and C2, 1mm deep starter notches were made with a saw and CNC milling respectively. During initiation of C1 the coupon failed under the upper grip due to fretting; therefore all subsequent tests were done with tabs glued to the clamping areas. For C1, the failed part was cut off and tabs were glued on the remainder to continue testing at a shorter coupon. par During crack initiation the force was increased from 20kN (35MPa) to 60kN (93MPa) in steps of 5kN. Because after 1million cycles still no crack was visible a jeweler saw cut was made in the existing saw cut, adding up to a total starter notch depth of 1.5mm (after final fracture of the coupon, the jeweler saw cut showed a strongly curved front due to the flexibility of the blade, which is clearly not suitable for thick coupons). Crack detection was at a total length (notch + crack) of 2.37mm at the back, while already being 4.11mm at the front side. The applied force was then reduced in steps of 5kN over the next 1mm of crack growth towards 20kN, after which the constant amplitude test at 20kN was run.

The non-symmetry in crack growth remained almost over the entire crack length. Figure 5.11 shows the front and back crack lengths together with the average length versus applied load cycles. This figure shows that up to 1.1 million cycles the crack length at the back was about half the length of the frontal crack.

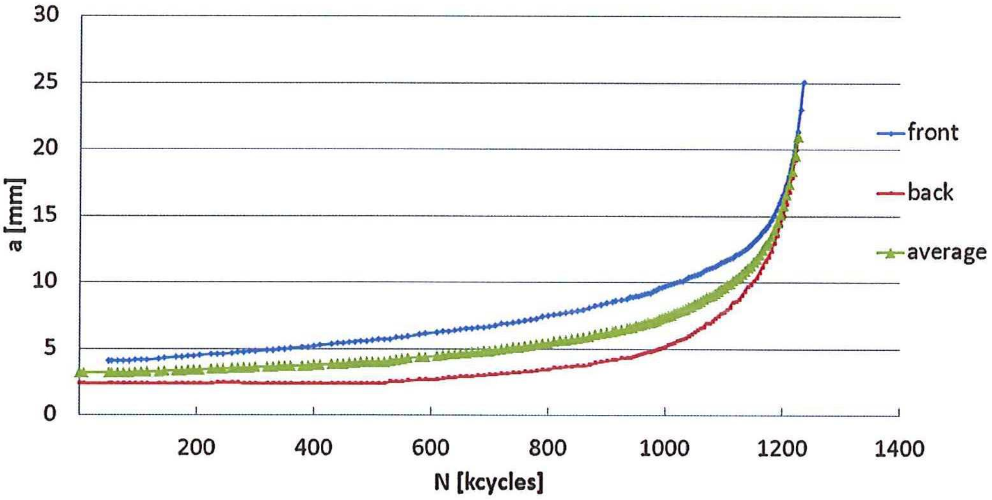

Figure 5.11: Crack length a versus applied load cycles N for coupon C1 showing strong non-symmetric growth. More symmetric crack growth towards the end of the test.

Because the K-solution assumes a straight crack front this solution becomes invalid if the non-symmetry gets too large. ASTM standard E-647 [103] suggests to declare results invalid if the difference in crack length is larger than a quarter of the thickness, being 3.17mm. By adopting this requirement every data point between a crack length of 4-10mm is invalid. Therefore the complete test is disregarded as part of any further analysis.

5.4.2.2 Coupon C2, baseline R=0.05

Because specimen C1 failed, stress-free specimen C2 was selected to repeat the procedure. To reduce the testing time and to stimulate symmetric growth, the applied CA stress was raised to 54.25MPa (35kN) for coupon C2. The crack faces of coupon C1 did not show shear lips for crack lengths below 40mm so shear lips were not expected to develop below $a = 25mm$, the target crack length. Inititation was done in the same way as for coupon C1. Unfortunately the initiation time was underestimated by the author and crack growth up to 6.3mm occured during precracking at 60kN (93Mpa) without taking any pictures. The force was shredded towards 35kN in steps of 5kN over the following 1mm of crack growth.

The crack grew -again- non-symmetrically towards an average crack length of 10mm were the maximum difference in crack length of 2.95mm was seen (Figure 5.12. By growing longer the crack straightened up and at $a_{average} = 22mm$ antisymmetric shear lips started to form and the test was ended at $a_{average} = 28mm$ with an overload until fracture.

The crack length versus applied number of load cycles is depicted in Figure 5.13. The square data points represent coupon C2. The data was modified such that at a crack length of 6.3mm N was equal to that of coupon C8.

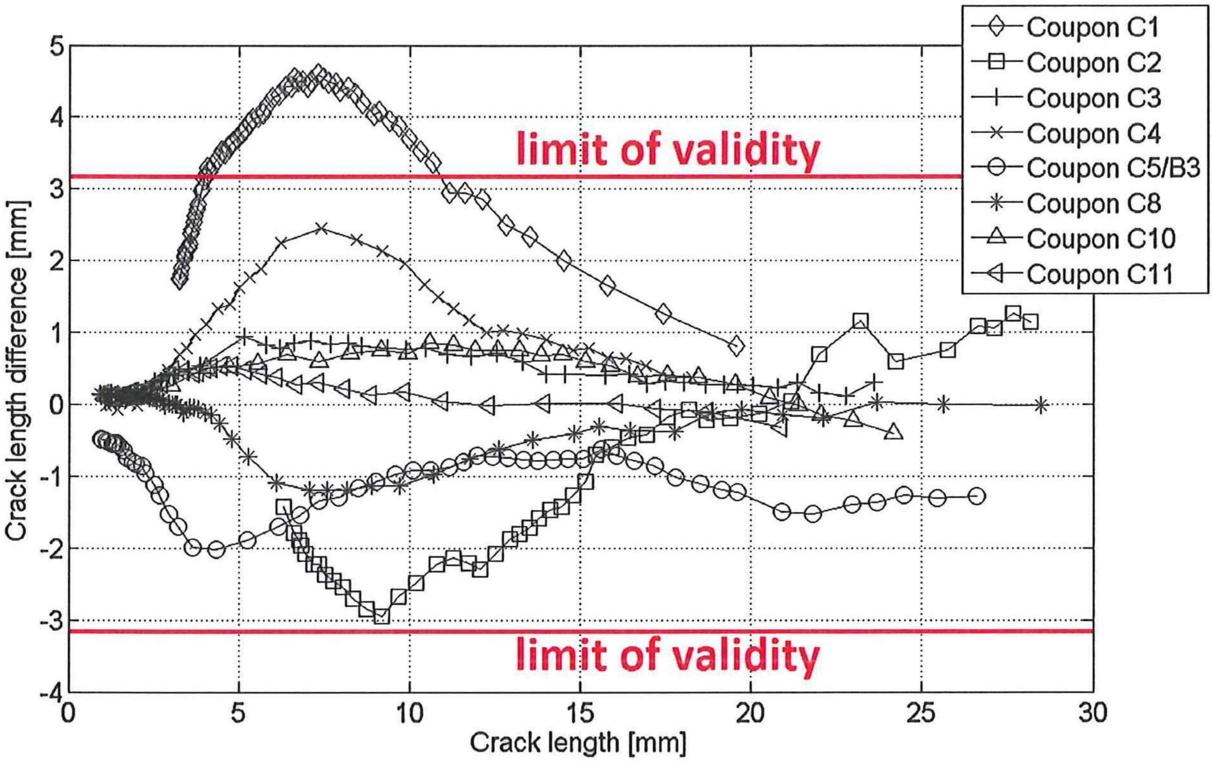

Figure 5.12: Difference between surface crack lengths versus average crack length. Red lines indicating limits of validity.

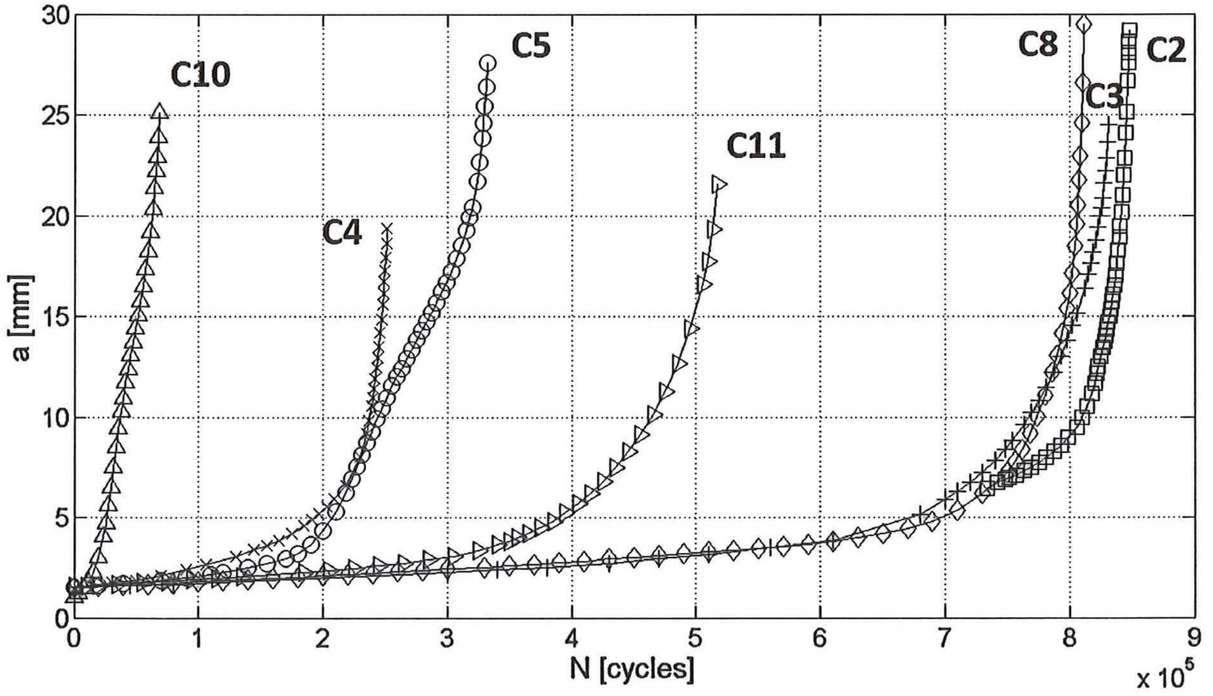

Figure 5.13: Average crack length versus applied number of load cycles. N=0 at $a_{average} = 1.5mm$ for all coupons exept C2.

5.4.2.3 Coupon C8, baseline R=0.05

For coupon C8 and all remaining coupons an EDM starter notch of 0.1mm thickness and 0.5mm depth was made. This -much sharper- notch simplified the precracking procedure because cracks initiated at the testing load after an acceptable amount of time. Crack growth was monitored without problems up to 25mm where the test was ended because of shear lip forming.

To provide some insight in the crack length measurements and its accuracy the left and right surface of coupon C8 are shown in Figure 5.14. Here the fatigue crack of 0.7mm can be clearly seen. For all copuons, by comparing two consecutive pictures, crack growth was estimated to be accurate up to ±0.01mm for the first 2mm of crack length. Further on the magnification of the camera was reduced and an accuracy of ±0.02mm is estimated. Measurement intervals ranged from 0.05mm for small cracks and increasing to 1mm at final crack length.

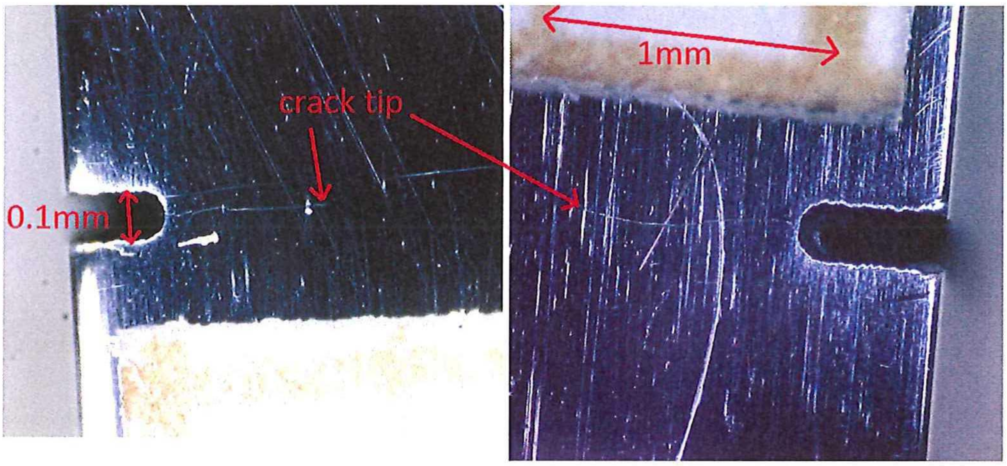

Figure 5.14: Left and right side of the fatigue crack in coupon C8 after 490k cycles. 0.7mm of crack growth from the starter notch. Crack tip can be clearly seen on polished surface.

5.4.2.4 Coupon C3, baseline R=0.7 and C4, baseline R=-1

Now the basline test at 0.05 was completed it was decided to test the two remaining baseline coupons at R=0.7 and R=-1 before testing a residual stress bearing coupon. Because no solution for the non-symmetric crack growth was found it was decided to continue testing in the same way as before. The clamping effect was, however, expected to be smaller since it is likely that the crack is fully opened during the whole load range at R=0.7 and thus the stress range above crack opening was not affected by the bending component. Similarly at R=-1 the crack was expected to be fully closed at P_{min} and fully opened at P_{max}, preventing the load range (only the local R) to be affected by bending effects. In other words, $\Delta K_{effective}$ was not expected to change, as it would do at R=0.05. P_{max} at R=0.7 was chosen to be 55kN such that ΔK was similar to that of the tests at R=0.05. The P_{max} at R=-1 was kept at 35kN. In this way the minimum and maximum crack growth rate was almost equal for all baseline tests, preventing extrapolation of data during later analysis.

As depicted in Figure 5.12 crack growth was very symmetric in coupon C3 (max difference 0.94mm) and acceptable in coupon C4 (2.49mm). No further difficulties occured during test C3 while during test C4 at an average crack length of 0.6mm a compressive overload of 60kN (93MPa) was accidentally applied. This resulted in an increased growth rate due to tensile residual stresses from notch plasticity for the next 1mm of crack growth. Because during the analysis the first 1.5mm of crack length was not taken into account, no effect was seen in the $\frac{da}{dN}$ versus ΔK graph later on (Figure 6.14).

5.4.2.5 Coupon C5B3, residual tension $R_{applied}$=0.05

With all baseline tests succesfully completed coupon B3 (B1, B2 and B4 were used for slitting) was EDM notched at the tensile residual stress side and fatigue tested in the same way as the previous coupons. P_{max} was again 35kN to make a fair comparison between the residual-stress-free and residual-stress-bearing coupons.

One strain gauge was mounted on each side of the coupon midline to check for symmetric clamping (see Figure 5.15, right). The maximum difference was $13\mu\varepsilon$ (1.4%) at 35kN.

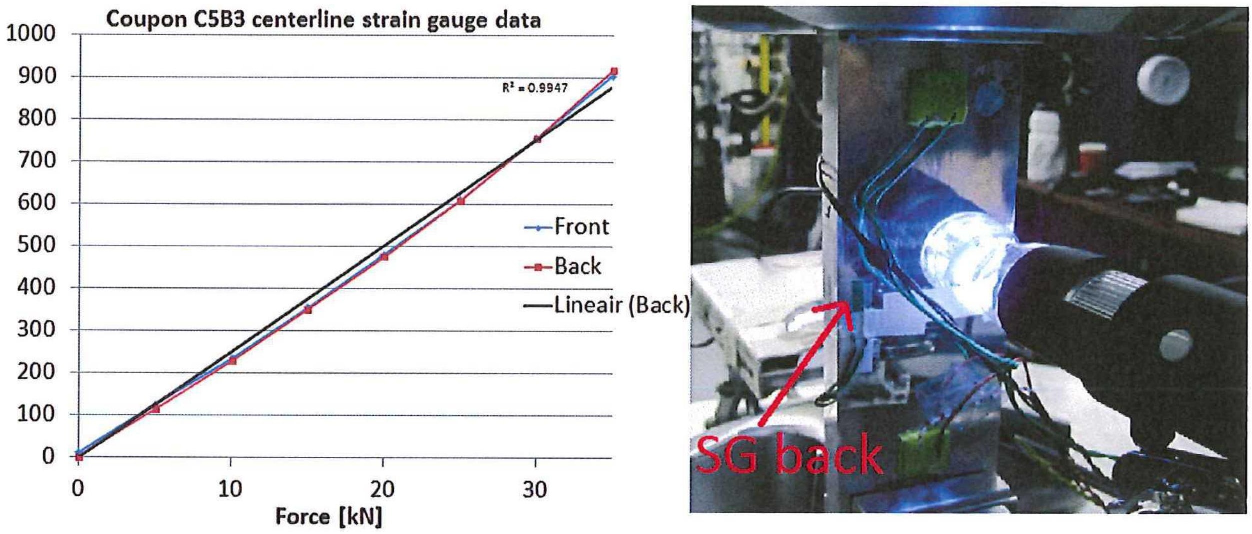

Figure 5.15: Specimen C5B3 installed in the 100kN TU Delft fatigue machine. Back side strain gauge is visible, starter notch behind the camera. Maximum difference $13\mu\varepsilon$ at 35kN applied force.

It was expected that the force-strain curve was linear. As can be seen in the graph both curves are not linear. The most plausible explanation for this effect is plasticity or slip under the clamps. A second effect could be the curvature of the specimen due to the four point bending. Furthermore, because of the starter notch the coupon has become asymmetric which could give rise to a non-linear response. Anyway, the difference between the two gauge responses is very small, which indicates symmetric clamping.

Despite the very careful clamping of the specimen the crack did not grow symmetrically on both sides. Figure 5.12 shows that the difference in crack length between front and back increased quickly to 2mm at $a_{average} = 5mm$. This difference then decreased to approximately 1mm for the remainder of the test. This behaviour is found throughout all coupons, see Section 5.4.4 for more discussion.

By looking at Figure 5.13) a distinct increase in crack growth due to tensile residual stres is seen for the first 5mm of crack length. Further on, crack growth was retarded due to compressive residual stress.

5.4.2.6 Coupon C6B5, residual compression $R_{applied}$=0.05

Bending coupon B5 was notched at the compressive residual stress side to make crack growth coupon C6B5. The specimen was clamped and precracked at $P_{max} = 50kN$ and $P_{min} = 1kN$. After one million cycles no crack initiation was found and the maximum force was increased by 5kN. Every 500k cycles this process was repeated untill a load of 70kN (108.5MPa) was reached. With still no crack initation, P_{min} was decreased to -40kN to enhance initiation. Just after doing this the tabs disbonded in shear.

To prevent future grip failure, the test setup was changed into a 3 point bending setup. In this way, higher forces could be applied to the specimen. The quality of the setup was checked with two strain gauges at the coupon midline. Over a loading range of 9kN strain readings were recorded in steps of 1kN. The difference between the two sides was $25\mu\varepsilon$. From the experience with other coupons this was considered good and the test was started.

After 375k load cyles still no crack initiated and the maximum load was increased to -10kN. After 2mm of crack growth at one side, no initiation was seen at the other side and the maximum load was increased to -11kN to enhance faster initation. Despite this effort the crack grew further up to 15mm without crack initiation at the other side, so there was an edge crack present of 15mm in length and less than 12.7mm in width. Within several thousands load cycles from here the uncracked side caught up and an almost symmetrical crack was formed. The last part of crack growth was symmetric.

It was observed that the difference in strain between both sides (at P_{max}) increased considerably with the edge crack growing larger. This means that the coupon was bending sideways in the direction of the edge crack. This bending created more tension at this side and thus increasing the growth rate, while at the uncracked side more compression was created which prohibited crack initiation. This means that if a crack starts to grow at one side, this side becomes more compliant and the coupon bends outwards in the direction of the crack, making the test inherently unstable.

Non-symmetric cracking can be attributed to several phenomena. First off all the residual stress from four point bending was not constant over the coupon thickness (see Figure 5.7). Secondly, the strain gauges showed an increase in difference when going from P_{min} to P_{max}. The latter was probably a result of a too flexible test setup. Therefore the setup was modified before the next test was started.

5.4.2.7 Coupon C7B6, residual compression $R_{applied}$=0.05

Before installing coupon C7B6 in the fatigue machine, the upper loading cylinder was replaced by an aluminum block, which was directly mounted on the hydraulic grip (Figure 5.16.

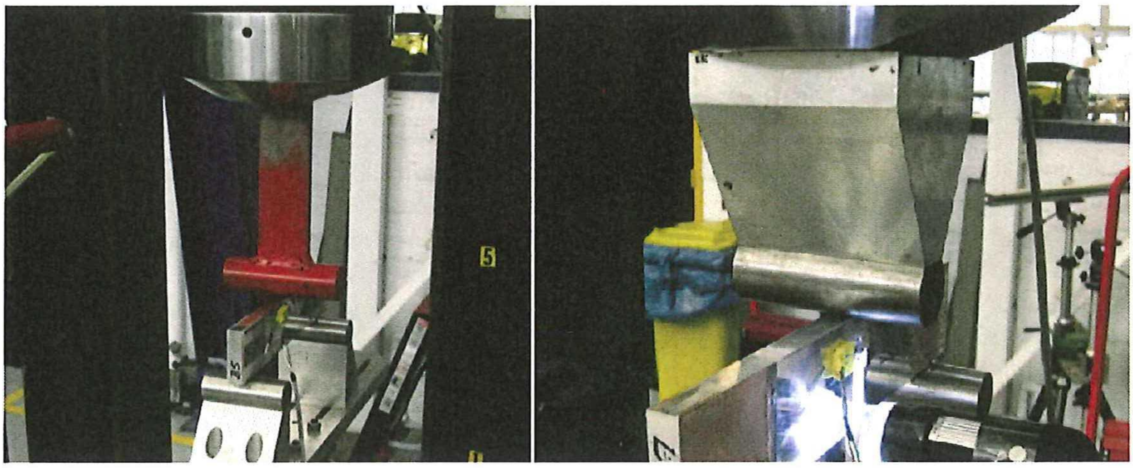

Figure 5.16: Improvement of the 3 point bending setup by replacing the T-shaped cylinder (left) by a rigid block.

Again two strain gauges were glued on the specimen midline but also two gauges were installed just next to the starter notch, 2mm from the coupon bottom tee see what happened at the crack location. By applying load the latter gave no difference in $\mu\varepsilon$ over the entire load range (0-11kN) while the upper gauges showed a difference of $20\mu\varepsilon$. This proved that little out of plane bending was present in the setup so the test was started.

Crack initiation occured uniformly over thickness. After a small amount of crack growth, at one side full crack arrest was observed while at the other side the crack grew longer. Therefore P_{max} was increased in steps of 0.5kN (keeping R constant) until the retarded crack started to grow again. At a P_{max} of 13kN crack growth was observed again.

For the remaining part of the test the longer crack kept growing faster than the shorter crack - see Figure 5.17- until break-through of the right side at 750k cycles. From this moment on the crack grew symmetrically but shear lips were already visible. The test was stopped at a crack length of 20mm with again no useful crack growth data.

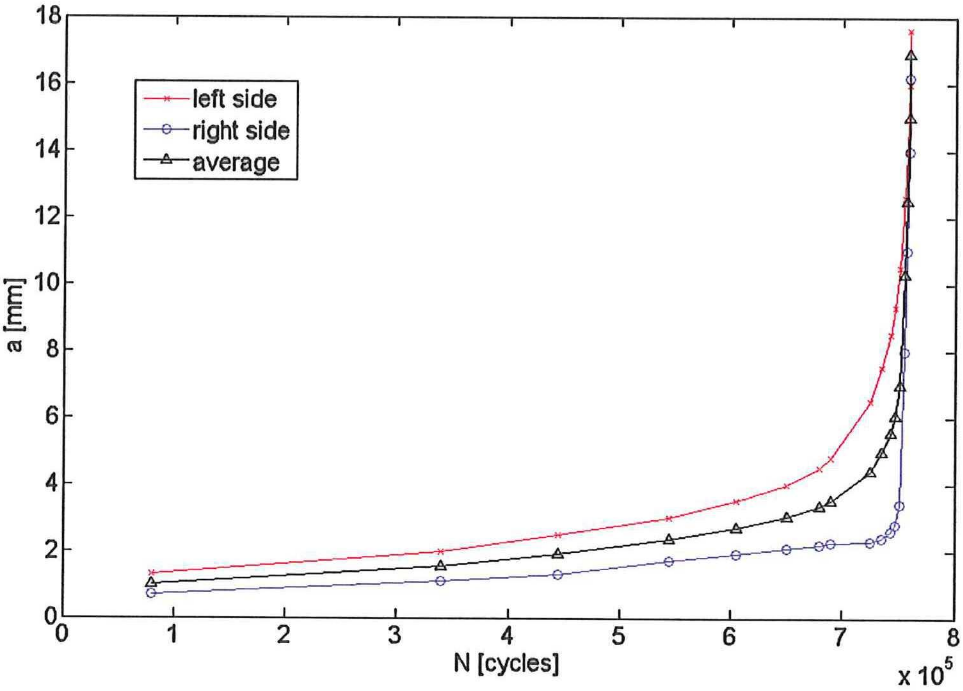

Figure 5.17: Crack length versus applied load cycles for coupon C7B6 showing non-symmetric growth and break-through of the right side at 750.000 cycles.

Because at the end of the test the crack was symmetrical, crack opening displacements could be measured. At an average crack length of 18.5mm, high magnification (200x) pictures were taken of the complete crack to capture the opening behaviour. Pictures were taken at P=0.1kN, P=0.65kN, P=1.3kN and P=2.05kN. Figure 5.18 shows the crack at the left side with a force of 0.1kN applied. The crack is fully closed for the first 3mm from the and opens further inwards because of tensile residual stress. At a load of 0.65kN the crack is still closed for the first 3mm and the crack opening slightly larger while at P=1.3kN only the outer 2mm of the crack is closed. At a load of 2.05kN the crack is completely opened. Near the crack tip the images are not clear enough (light scattering due to plasticity and shear lips) to see measure COD. From this can be concluded that partial crack closure is significant and present up to P=2.05kN. This data can be used to validate finite element predictions.

Since the last two test completely failed a decision had to be made on the subsequent steps. I was believed that the 3-point-bending configuration could not be improved any more because the strain gauges gave almost similar strains at both sides. Additionally, the SEN(T) configuration was not capable of applying the force magnitude that was required due to bonding failure. A possibility was to increase the depth of the starter notch such that crack initiation and growth could be achieved in SEN(T). This would however reduce the obtainable crack growth data (which wal already much smaller then in previous tests because of small scale yielding limitations). Another option was to increase the loading in the 3-point-bending configuration such that more symmetric initation and early growth could be expected. In this way it would be not possible to have a crack growing through a reversing crack growth field (from compression into tension or vice versa) which was desired to fully validate crack growth predictions. Therefore the final three coupons C9, C10 and C11 were tested with a starter notch at the residual tension side at R=0.05, R=-1 and R=0.7 respectively.

5.4.2.8 Coupon C9B9, C10B8 and C11B10 residual tension at R=0.05, -1 and 0.7

After clamping coupon C9B9 into the fatigue machine the strain gauges at both side recorded an $80\mu\varepsilon$ difference. The coupon was dismounted and rotated and after clamping the strain difference was the same.

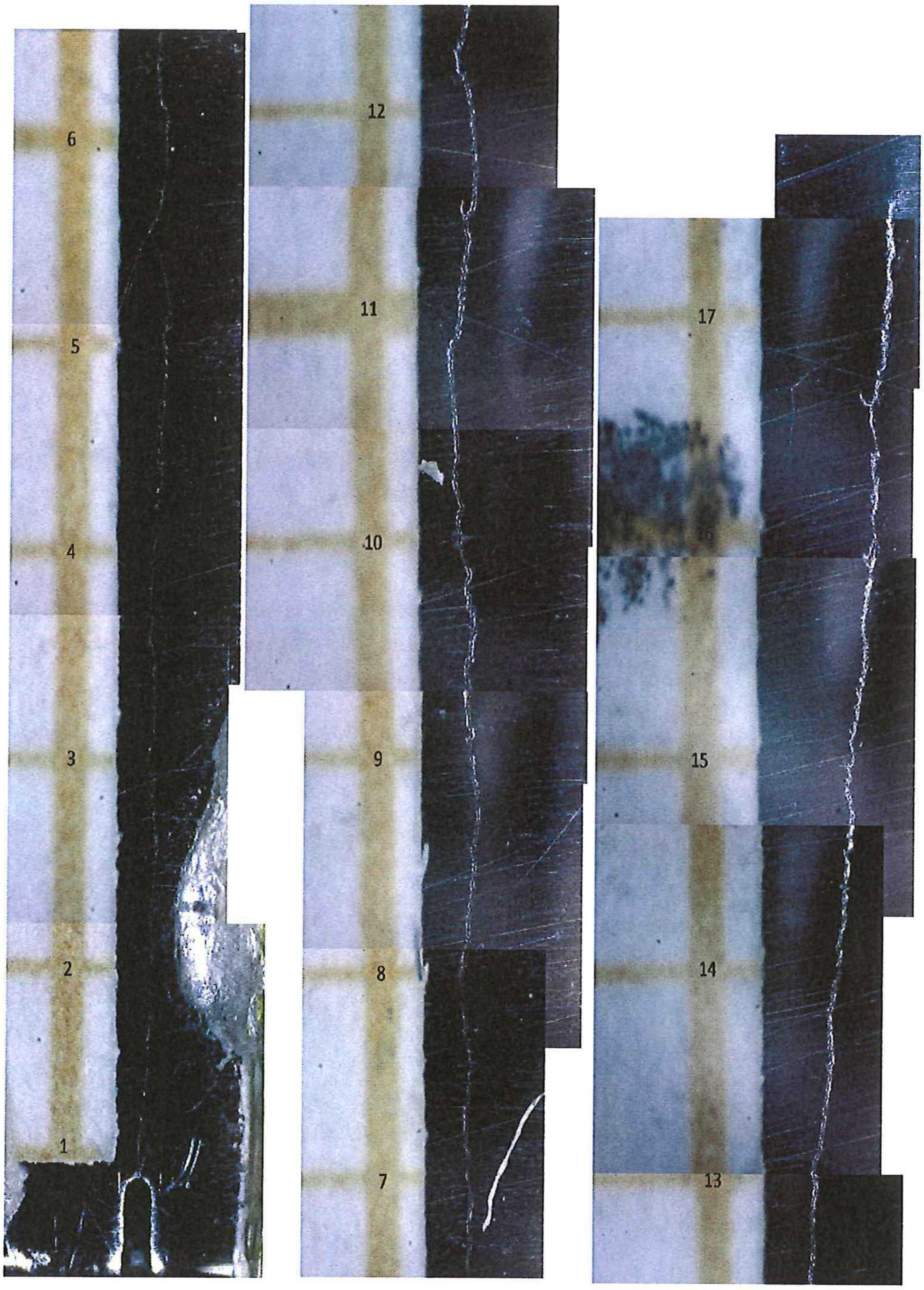

Figure 5.18: Crack profile of coupon C7B6 at $P = 0.1kN$ with the crack starting at compressive residual stress and growing into residual tensile stress. The crack is closed for the first 3mm and opens further inwards. Starter notch in the left bottom and crack grows upwards. Shear lip visible from 13mm.

This means that the misalignment was not due to the fatigue machine but from coupon imperfections. Aluminum foil inserts were placed between the grips and the crosshead to reduce the strain imbalance to $20\mu\varepsilon$, which was considered small enough to start the test.

After 300k cycles the left side started to crack while no initiation was present at the right side. While the left side crack grew to 4.5mm the right side did not grow and the grips were opened to add an aluminum foil to generate more tension at the right side. In this way, crack growth was stimulated on the right side. Unfortunately the left side kept growing to 9.42mm until after 660k cycles the right side suddenly cracked to 3.76mm. After this the crack became more and more symmetric with a final difference of 0.7mm between left and right.

Unfortunately it was only realized after the test that opening the grips (and thus changing boundary conditions due to residual stress redistribution) during the test invalidates the remainder of the test and thus no useful crack growth data was generated.

To enhance symmetric crack growth, coupons C10 and C11 were clamped such that the side with maximum residual tension from 4-point-bending was at the side with minimal tension after clamping. In this way the disbalance from clamping would be (partly) counteracted by the disbalance in residual stress. Both copons were initiated at $P_{max} = 35kN$ and $P_{min} = -35kN$ which led to very quick symmetrical crack initiation. Coupon C10 was further tested at the same load range while the load for coupon C11 was set to $P_{max} = 55kN$ and $P_{min} = 38.5kN$ (R=0.7) directly after initiation was observed. As can be seen in Figure 5.12 both coupons cracked very nice, with a maximum difference in crack length of less than 1mm.

5.4.2.9 Marker load coupons ML1 and ML2

To visualize the crack front shape two spare coupons without residual stress were tested with small overloads after every 4000 baseline cycles. Because the overloads will locally increase the crack growth rate, they are visible on the fracture surface under a scanning electron microscope (SEM).

Specimen ML1 was initially fatigued at 93MPa which was reduced in two steps to 47MPa while the overloads were kept at 16MPa above the baseline cycles. P_{min} was kept at 8MPa throughout the test. These reduction steps led to fretting, which is indicated on the fracture surface in Figure 5.19.

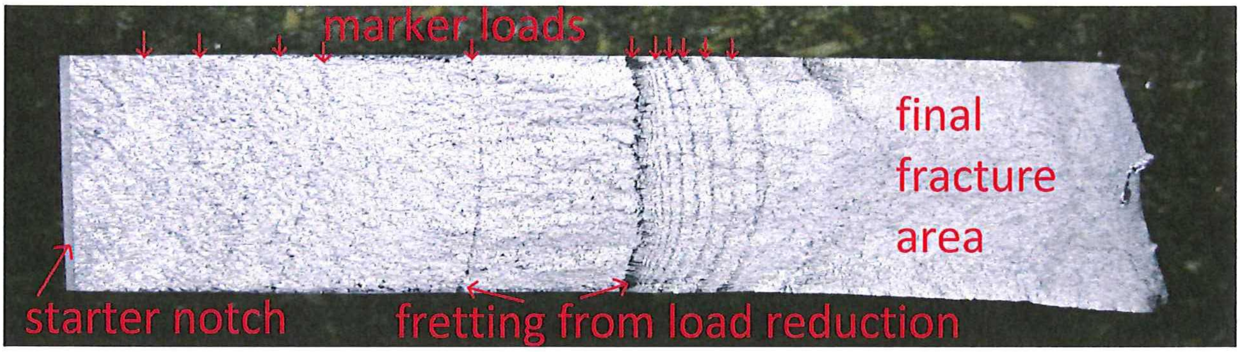

Figure 5.19: Fracture surface of coupon ML1. Crack initiated at the left side. Dark marker load bands show an increasingly curved crack front.

The last 10 visible dark bands are from the overloads. It can be seen (with some effort) that crack initiation was at the top left side and became a through crack later on. Because of this, the first 14mm of crack length was not useful for crack front reconstruction.

To stimulate symmetric growth, in coupon ML2 the loads and R-ratio were increased, as shown in Figure 5.20. Three different marker bands (five, three and two overloads) instead of one were applied to facilitate easy recognition during the SEM observations.

The marker loads were visible under the SEM at a magnification of 1000X, see Figure 5.21(left) where three blocks of three overloads are visible. The right picture shows that at a magnification of 5000x the repetitive pattern of 5, 3 and 2 overloads are easily identified.
Because of the coarse grain structure of 7050 aluminum, marker bands were difficult to follow through the coupon thickness. Grain boundaries, transverse cracking, fretting, different grain orientations and light scatter made the marker bands discontinuous. Despite of this, the crack front has been reconstructed between $a = 2mm$ and $a = 12.5mm$. This data is presented in the next section.

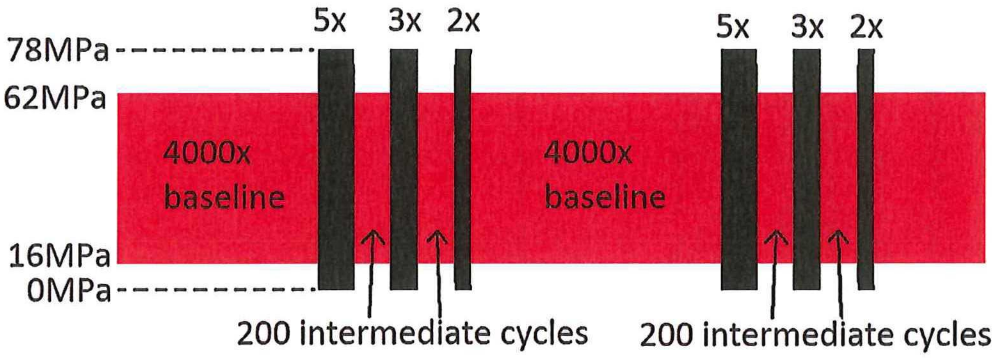

Figure 5.20: Sequence of marker loads as applied to coupon ML2. A block of 5, 3 and 2 overloads with 4000 baseline loads is continually applied. Between the overloads 200 baseline cycles are applied. Baseline cycles: $P_{max} = 62MPa$; overloads: $P_{max} = 78MPa$.

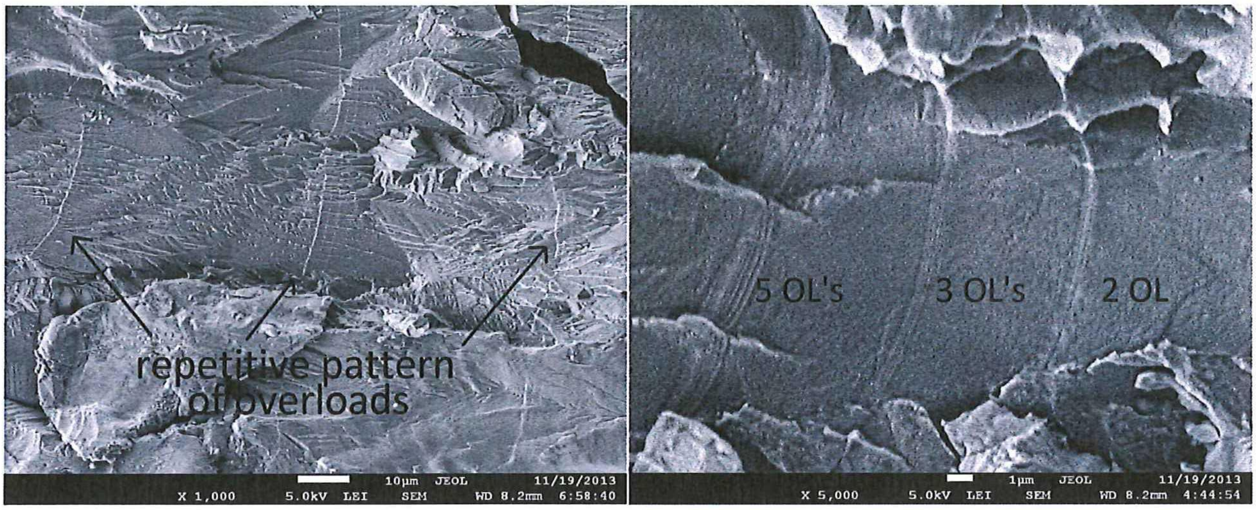

Figure 5.21: SEM pictures of the fracture surface of 7050 aluminum. Three repetitive blocks of marker loads visible at a magnification of 1000X (left). Individual marker loads indentifiable at a magnification of 5000X (right).

5.4.3 Crack curvature

As introduced in Section 2.3.3.3 the crack front will not be straight in thick coupon. Because crack length measurements are done from the surface, these values must be corrected for the average crack length.

Crack front data has been obtained from various coupons and is depicted in Figure 5.22. The first six purple lines are obtained with the SEM from marker loads on coupon ML2. The blue and red line are from final fracture of coupon C4 and C5 respectively while the last five orange lines come from Figure 5.19. Crack fronts were reconstructed by hand.

It is clear that up to a crack length of 6mm, the crack front is close to linear. It is remarkable that at 4mm crack length the curvature is negative; this effect is still slightly visible at 6mm crack length. From a=8mm and longer, the crack front gets curved more and more. Apparently, for the first six milimeter the stress intensity factors are too low to generate a large plane stress area near the surfaces and the crack behaves as in plane strain. For longer cracks, plasticity will be more pronounced at the coupon edges.

To make a correction on the crack length measurements, average crack lengths are computed for $a > 6mm$ and the average surface crack lengths are subtracted from this value. This gives the average additional crack length that was present inside the coupon for every surface measurement. By plotting a quadratic function through these data points, a correction function is obtained for surface crack length measurements

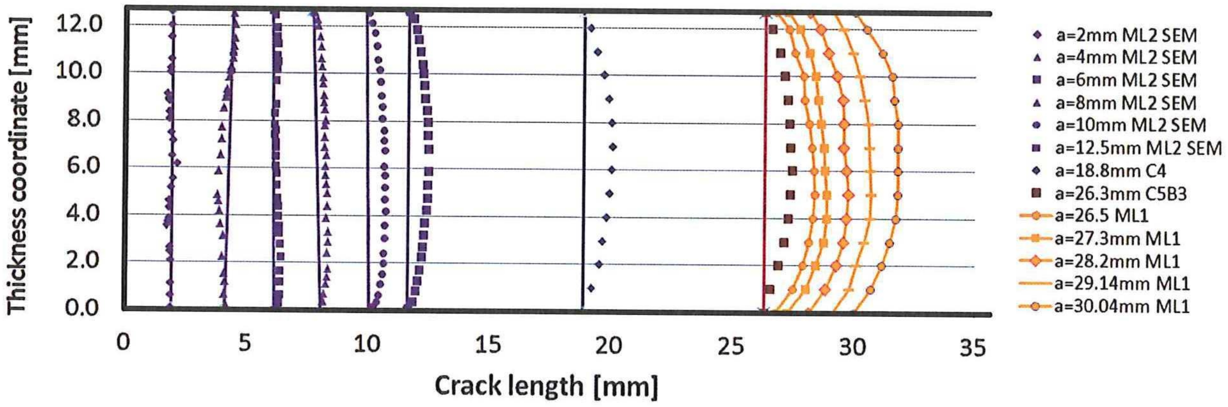

Figure 5.22: Crack front shape evolution. The initially straight crack front becomes more curved as it grows longer. The straight lines connect surface points.

between a=5mm and a=30mm, see Figure 5.23. Before the fit, nine data points of zero curvature at a=5mm have been added to force the curve though the x-axis here.

The red data point comes from coupon C5B3. At a crack length of 26mm, the crack has just grown through almost the complete compressive residual stress field which lowered K considerable as compared to the other (residual-stress-free) coupons. Therefore crack curvature is below the average for this data point. This immediately shows that the correction function will not be very accurate for coupons with residual stress. However, as can be seen in Figure 5.23, making no correction is more errorneous.

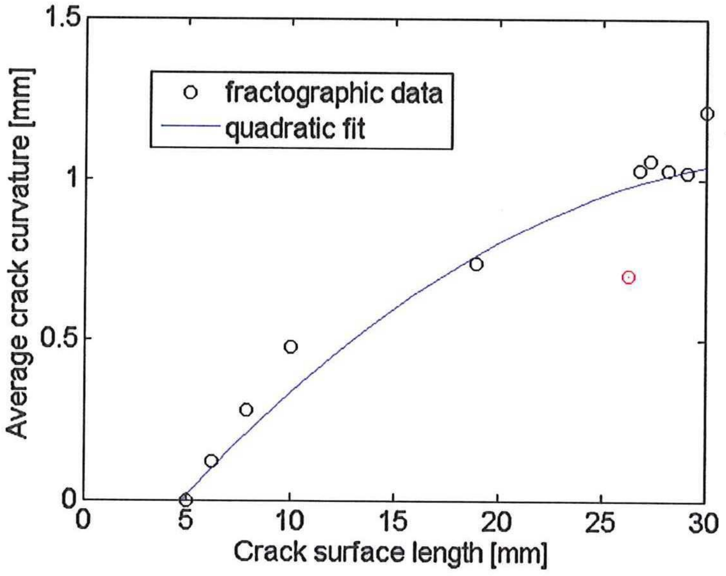

Figure 5.23: Through-thickness average crack length versus surface crack length. Quadratic fit gives correction function.

A more in-depth evaluation of crack curvature of function of applied loading, residual stress, material, thickness would therefore be preferable. In that respect, comparable results have been obtained by Branco and Antunes [111] by FEM analysis of a 10mm thick M(T) specimen. Figure 5.24 shows that the crack shape evolution is comparable to the test results herein. Altough not one-on-one comparable, because an initial curved crack front was assumed, this effect is neglectable for longer crack lengths.

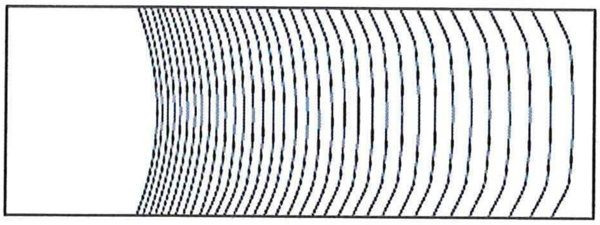

Figure 5.24: Crack front evolution with in initial curved crack front. Thickness=10mm, R=0.1, C=5.5054x10^{-11},m=3.544 [111]

5.4.4 Non-symmetric crack growth

It has become clear from the previous sections that non-symmetric crack growth over the coupon thickness is the major issue in the presented test results. It was noticed that even though crack initiation could be symmetrically, initially one side of the crack was always growing faster than the other side. The main reasons are a non-symmetric residual stress field through coupon thickness and bending effects due to clamping in the fatigue machine (due to coupon curvature from four point bending and residual stress distribution after machined out of large block, tabs not glued perfectly parallel to the specimen, fatigue machine misalignments, grip wear out, etc.). The combination of both effects causes non-symmetric crack growth.

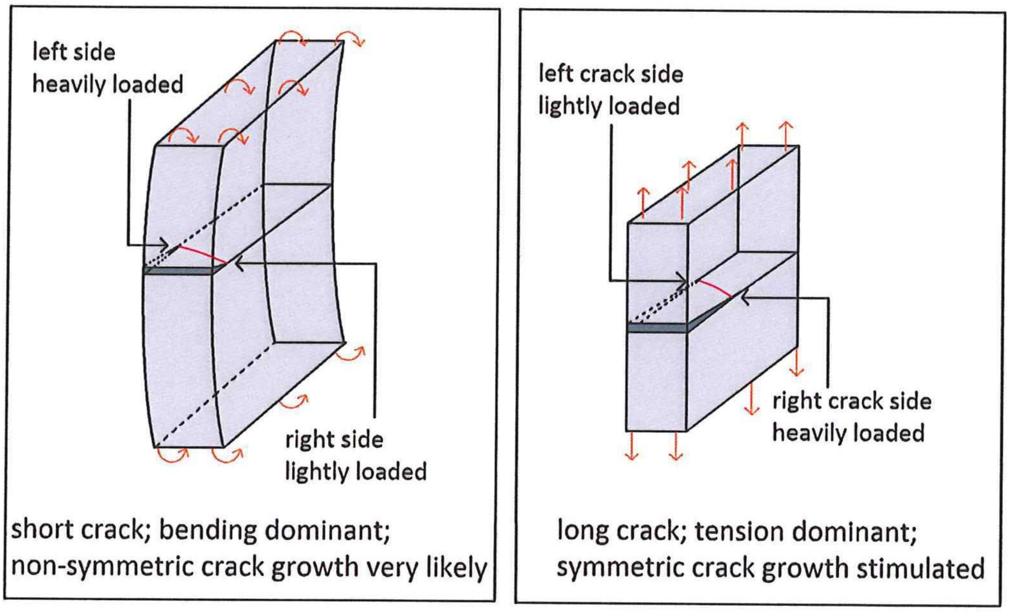

Figure 5.25: Left figure: at short crack lengths the bending moment from clamping is considerable and non-symmetric growth will occur. Right figure: at long crack lengths the tension component gets dominant and the crack straigthens up.

By looking at Figure 5.12, the trend for almost all coupons is that maximum crack length difference can be found around a=7mm, after which the difference in length decreases again. This is a geometry dependent effect which is visualized by considering a short and a long crack in Figure 5.25. When the crack is still small (left picture) the bending strains are considerable as compared to the applied tension strains (typically 10% of the maximum strain). Therefore the crack grows faster at the left side.

As the crack grows longer the net coupon section becomes smaller and thus the longitudinal strains larger. This makes the relative effect of the bending moment smaller. Additionally, the side at which the crack is shortest will be more heavily loaded during crack opening and thus symmetric growth is stimulated (right picture). This makes the shortest crack side catching up after the latter effect gets dominant.

It can be concluded from this that if longer coupons are used, the non-symmetric crack growth will be a smaller issue since clamping misalignments will have less effect. Secondly, the coupons should be clamped such that the disbalance in residual stress at the starter notch side is counteracted by the clamping disbalance. This gives the highest change of symmetric short crack growth.

5.5 Conclusions

From the fatigue tests it can be concluded that for a coupon of 12.7mm thickness non-symmtric crack growth is always present. The amount of non-symmetry is dependent on coupon curvature, fatigue machine alignment and gripping. It was noticed that shorter coupons give more non-symmetric growth. Fatigue testing in 3 point bending does not offer a solution for this problem because once the crack grows larger at one side, this side becomes even more stressed.

The crack front shape evolution can be reconstructed by applying overloads of 16MPa with sufficient baseline cycles in between.

Chapter 6

Analysis

In this chapter the test results from Chapter 5 are analysed. First the four-point-bending residual stresses are determined in Section 6.1 in which three independent methods are employed: strain history 6.1.1, slitting 6.1.2 and a FEM model 6.1.3. Thereafter the crack growth test are analysed in Section 6.2.1 and finally in Section 6.2 LEFM crack growth predictions are made and compared to test data.

6.1 Residual stress determination

The residual stress distribution in length direction over the coupon height is determined by three indepent methods. The first derives the residual stress from the strain measurements on the top and bottom of the coupon via the stress-strain curves. This method is called *bending strain method.* The second method calculates the residual stresses from the slitting experiment called *slitting method.* Thirdly a Finite Element Model of the four point bending procedure has been made and residual stresses after unloading are retrieved. In the next sections the results from the three methods are presented.

6.1.1 Bending strain method

The bending strain method employs the complete strain history to obtain the residual stress at each point over the height of the coupon. In Section 5.2.2 it was shown that the strain distribution over the coupon height was linear at maximum load and after springback. Therefore the strain at any point in time can be linearly interpolated between the top and bottom strain. An advantage of this method is that for any coupon a tailored residual stress solution is found from the bending strains and scatter in upcoming crack growth tests can be reduced.

For this method data from the top and bottom strain gauges is used. Because these strain gauges were placed centrally (neutral axis, see Figure 6.1 *a* and *b*), out-of-plane bending did not influence the results and therefore the average strain over coupon height was measured. One might argue that the stress-strain curve is not linear and thus taking the average between two strain values would give too low results. Figure 6.1c, however, shows that this effects is negligible.

After the maximum bending stresses have been reached, linear unloading is assumed. Figure 6.2 illustrates the method for the bottom of the specimen which is strained up to 10.000 $\mu\varepsilon$ and $\pm 1.500\mu\varepsilon$ after springback. First the tensile stress-strain curve is followed up to 10.000$\mu\varepsilon$ and then a linear line is drawn downwards towards the residual strain of this point. The final data point now contains the residual stress. Since the E-modulus of 7050-T7451 differs in tension and compression it is not obvious which value should be chosen as slope of the springback line. For the analysis here it is assumed that the specimen stiffness is the average between the tensional and compressive value. For the top half of the specimen the compressive stress-strain curve is followed and linear springback towards a positive residual stress is assumed.

To determine the complete residual stress distribution a MATLAB™ script was written in which the experimental stress-strain curves were converted into a function by using the *spline* function (no fit errors). Then the strain distribution was linearly interpolated between strain gauges 1 and 2. The stress at both

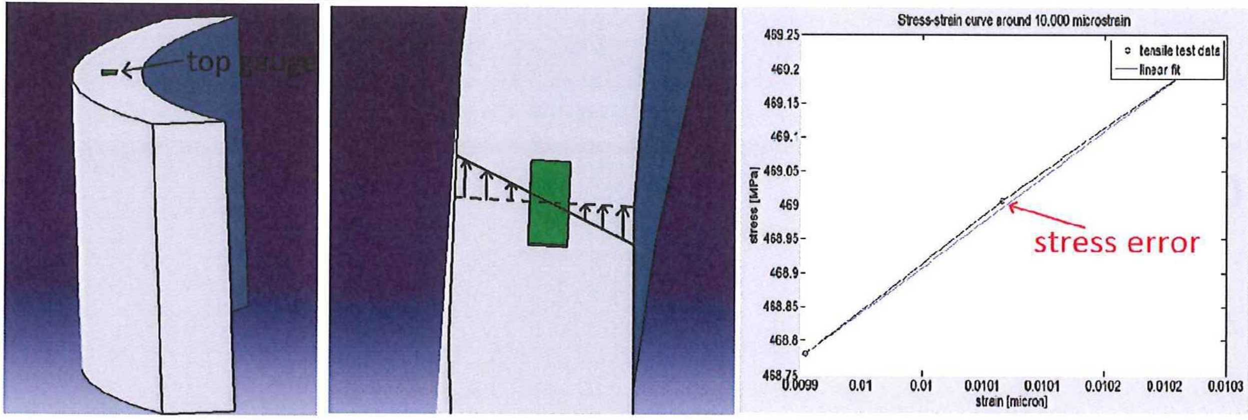

Figure 6.1: Out-of-plane bending due to misalignment in setup or coupon (a). Strain distribution over thickness due to out-of-plane bending (b). Linear interpolation error is small (c).

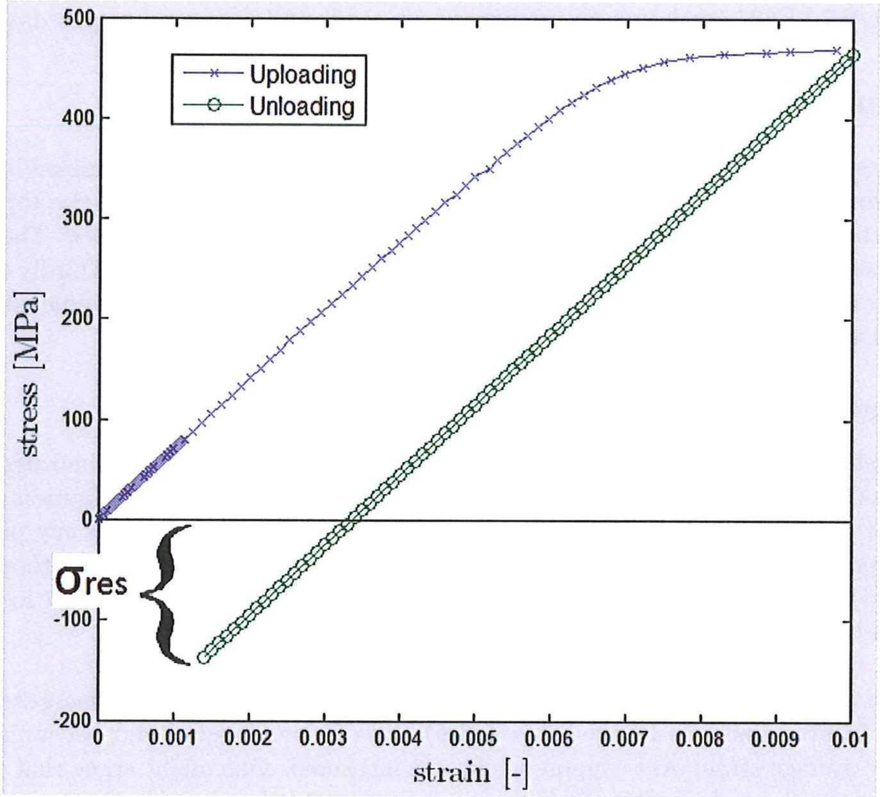

Figure 6.2: An illustration of the bending strain method showing the bottom of the beam first loaded in tension and unloaded to residual compression.

stages was now obtained from evaluating the splinefit by using the *ppval* command. By now subtracting the springback stress from the maximum stress the residual stress was obtained.

Figure 6.3 shows the residual stress distribution in coupon B2-B6 and the maximum difference at any point plotted by the dashed line. The variance is smaller than 10MPa for most of the time; only around $\frac{H}{W}$=0.38 the difference shoots to 11.5MPa.

An error of this method can that the Bauschinger effect is not taken into account. The Bauschinger effect is the phenomenon of a reduced yielding point when a metal is plastically strained in reversed direction. 7050 aluminum shows a very strong Bauschinger effect (e.g. figure 6 in [112]). Here it can be

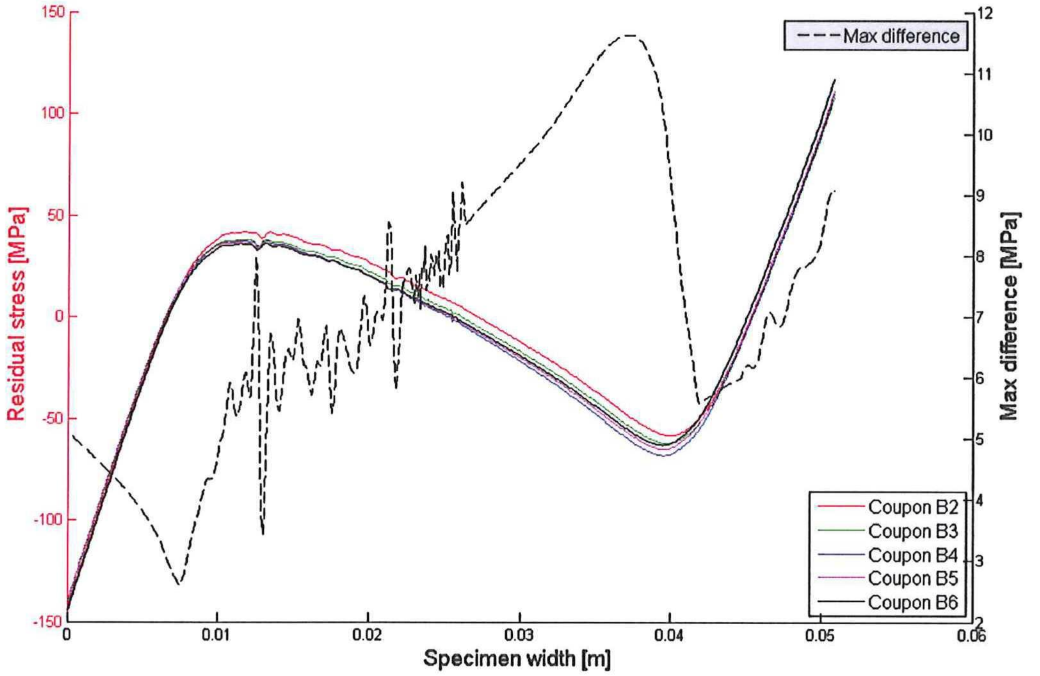

Figure 6.3: The residual stress distribution (left y-axis) in x-direction and maximum difference (right y-axis) over coupon height as determined by the *bending strain method*.

seen that after a tensile strain of 1% reversed yielding already starts slightly below zero stress. Kuruppu et al. [112] have found that the elastic stress drop is of 7050-T7451 aluminum is 700MPa after a tensile strain of 0.95%. This means that with a maximum stress of 475MPa in the experiments herein, a residual stress of 225Mpa can develop without Bauschinger effect. Since from linear analysis the maximum residual stress is 140MPa, no Bauschinger effect is expected.

One way of incorporating the Bauschinger effect is to derive the stress-strain curve directly from the bending strains [113]. This method employs elastic-plastic beam theory to convert top and bottom strain gauge data into the complete tensile and compressive stress-strain curves. The method was tried and gave good results for the uploading part but too high stresses for the unloading curve. The reason for this error is stress relaxation around maximum bending moment as a result of the manually applied bending force which was not perfectly continuous. This stress relaxation made the change in applied bending moment dM very large as compared to the change in strain (for pure relaxation the ratio $\frac{dM}{d\varepsilon}$ goes to infinity) and subsequently the stresses were overestimated.

A second potential error is the slope of the springback line, or in other words the weighted average stiffness of the material during unloading. In the above analysis the average stiffness from the tension and compression tests is used. Because it has been shown that the neutral bending axis shifts during loading, the tensile and compressive area's are not equal in size. It is therefore unclear what stiffness must be taken. Nevertheless it is assumed that taking the average is fairly accurate.

6.1.2 Slitting residual stresses

In this section the methodology for determining residual stresses from the slitting experiments (see Section 5.3) is shown and the results are compared to the *bending strain method*.

The residual stresses are assumed to be a linear combination of known stress distributions. These functions can be of any form, but Legendre polynomials are chosen here because these inherently satisfy force and moment equilibrium (Figure 6.4).

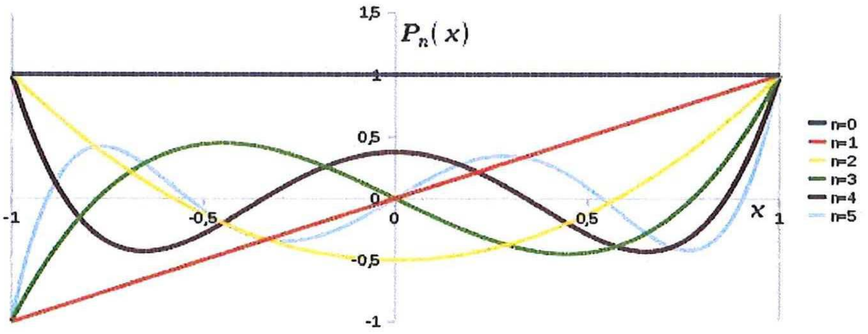

Figure 6.4: The first six orders of Legendre polynomials. From n=2 and higher equilibrium is satisfied automatically.

Residual stress is therefore expressed as

$$\sigma_x = \sum_{p=2}^{m} A_j P_j(x) \tag{6.1}$$

where P_j are known Legendre functions and A_j are a set of unknown amplitudes that can be determined from the measured strain data. The highest order term, m, appearing in the series is determined during data reduction such that the rms fit is minimal. The unknown amplitudes are related to measured strain by a compliance matrix. This compliance matrix is a geometry-specific 'stiffness' and represents the strain the would be present at the strain gauge location if the residual stress had the form of this Legendre function. Now using superposition, the strain that would occur as a function of slit depth for the residual stress in Equation 6.1 is

$$\varepsilon(a_i) = \sum_{j=2}^{m} C_{ij} A_j \tag{6.2}$$

Because $\varepsilon(a_i)$ is the measured strain and C_{ij} is also known, A_j can now be found by inverting Equation 6.2 in a least squares sense. In Matlab the command *pinv* is used for this.

For the anaylis here, FE data from Lee and Hill [72] for Legendre orders 2-12 are used as compliance input (see Erratum for more accurate data: [114]). This data is published for a generalized stiffness E'. For fully plane stress conditions $E' = E$, while full plane strain would give $E' = E\frac{1}{1-\nu^2} = 1.099$. With a specimen thickness of 12.7mm a neither fully plane-stress nor plane-strain is present. In fact, this factor changes with cutting depth and thus finding an average value would be more accurate than assuming either plane-stress or plane-strain. Aydiner and Prime [110] provide a 3-dimensional constraint factor, which turns out to be 1.0127 (thus closer to plane-stress than plane-strain). This factor is multiplied by the compliance functions to account for the finite thickness of the specimen.

In order to perform the data reduction Legendre functions were sampled at every cutting increment and stored in a matrix. The same was done for the compliance data from Lee and Hill. Both matrices served as input data for a Matlab script provided by Michael Prime [115]. The script can be found in Appendix B.6.

Since the number of available compliance functions is 11, there are 11 possible expansion orders: 2, 2-3, 2-4,...,2-12. This simply means that if the expansion order is increased, more Legendre polynomials are fitted to the strain data. To get more insight into this effect, residual stress distributions over all expansion orders are plotted in Figure 6.5 in where the open data points show the average stress of expansion orders 2-11 and 2-12, as will be the final solution.

It can be seen that for a<10mm the solutions oscillate heavily while for 10mm<a<50.8mm the data converges quite well. Now it is the question which of the eleven solutions describes the residual stress distribution most accurate. To quantify this, Cheng and Finnie [116] recommend to do a convergence test

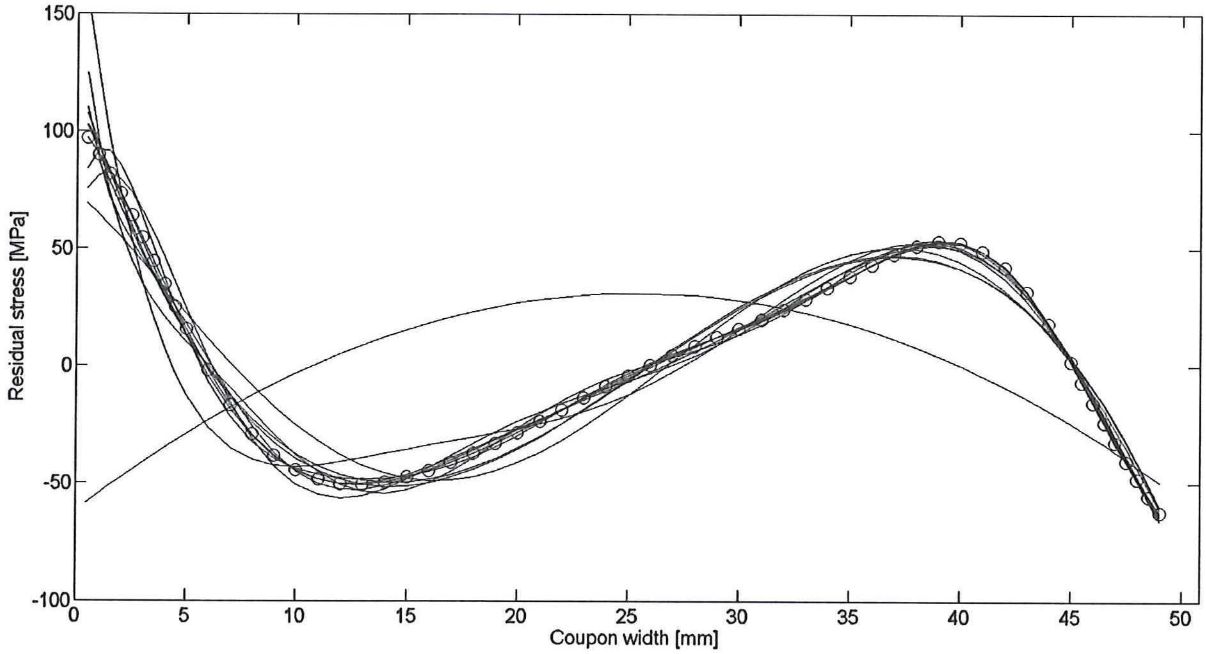

Figure 6.5: Residual stress estimate for Legendre oders 2,2-3,...,2-12 obtained by LSF.

for 0.2<a/W<0.9 as they refer to as the main convergence test. Once main convergence is satisfied, stability in the region a/W<0.2 and a/W>0.9 can then be improved by taking the average of converged solutions [116]. Because convergence here is excellent for a>10mm the domain 10mm<a>50.8mm is selected for the main convergence test.
The normalized deviation over two consecutive orders i and i-1 is:

$$\delta_i = \sqrt{\frac{\sum_{k=1}^{m}[\sigma_i(x_k) - \sigma_{i-1}(x_k)]^2}{\frac{1}{4}\sum_{k=1}^{m}[\sigma_i(x_k) + \sigma_{i-1}(x_k)]^2}} \qquad \text{for } 10mm < a < 50.8mm \tag{6.3}$$

in where k is the slit increment, σ is the residual stress at expansion order i or $i-1$ and x_k is the slitting depth at increment k. Convergence is assumed to start when δi<6%. By calculating the main deviation for coupon B2 and B4 it is found that the last three expansion oders (2-10, 2-11, 2-12) give convergence for B2 while for B4 only the last two orders converge.

The average of the converged solutions are plotted in Figure 6.6 together with the individual uncertainties per data point. Both solutions are very similar in magnitude and shape but are somewhat shifted. This shift can be due to the difference in rolling direction between the two coupons. The individual uncertainties are largest at the beginning of the cut, there where the oscillations in stress solutions are large. The main error is that the stress solution cannot be perfectly fitted to the measured data.

Since the compliance functions were available up to order 12, no higher order terms are included in the analysis here. Because higher orders tend to match the average better (see Figure 6.5) this probably would give better results. To quantify the effect of adding higher order terms, the average result for coupon B2 of orders 11 and 12 were compared and the difference computed. The maximum difference in stress when increasing from order 11 to order 12 turns out to be 1.19MPa with an average of 0.04MPa. These low values, together with the fact that differences typically get smaller with increasing expansion order show that taking n=2-12 is sufficiently accurate.

As a quality check, the strain fit is plotted together with the measured strains in Figure 6.7. It shows that the solutions match very well to the measured data. The average strain misfit is $0.7\mu\varepsilon$ and $0.8\mu\varepsilon$ for coupons B2 and B4 respectively.

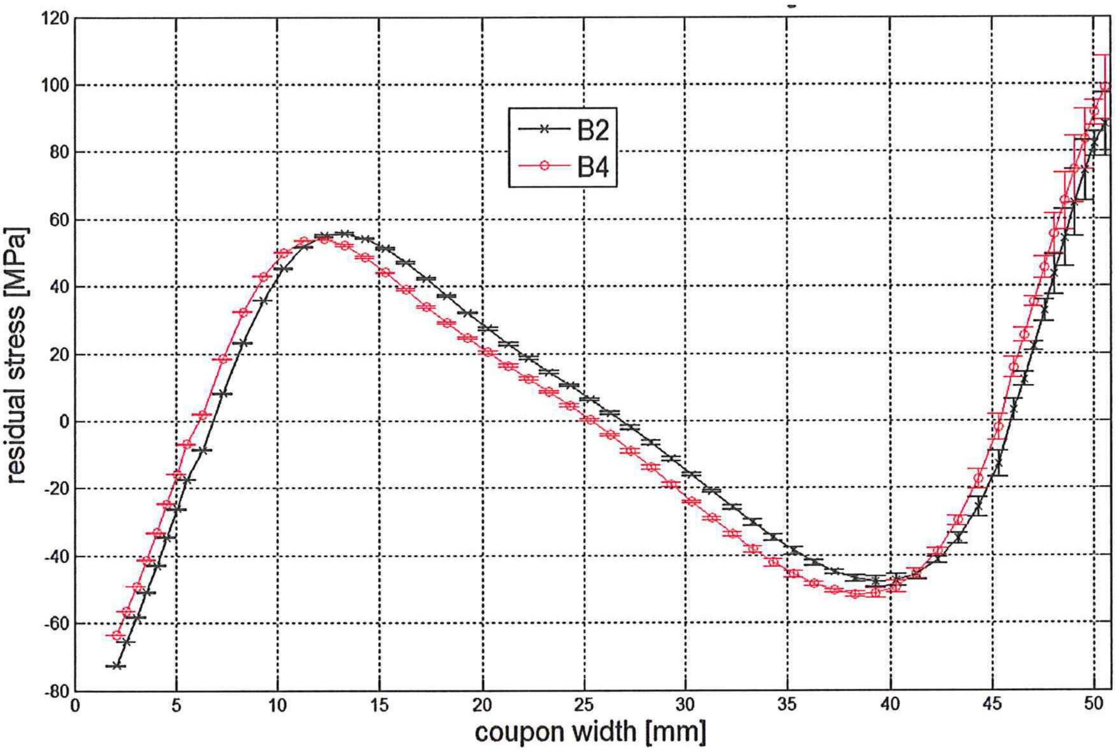

Figure 6.6: Slitting residual stress distribution over coupon width for coupon B2 and B4. Errorbars showing the individual uncertainties.

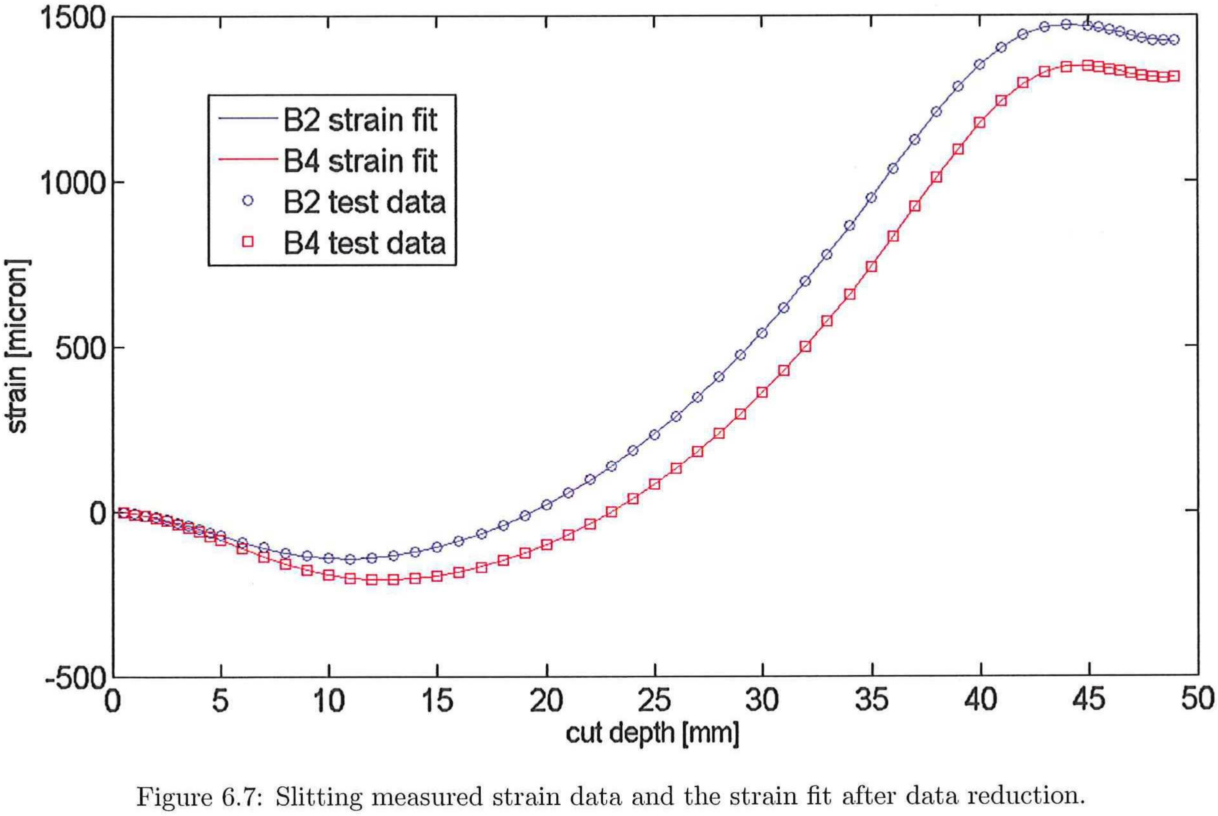

Figure 6.7: Slitting measured strain data and the strain fit after data reduction.

Because the stress is calculated as the average stress over the slit increments and the slit was made upto 49mm, the residual stress at the final 1.8mm cannot be determined. By plotting the slitting stresses together with the stresses from the *bending strain solution* a comparison can be made, see Figure 6.8.

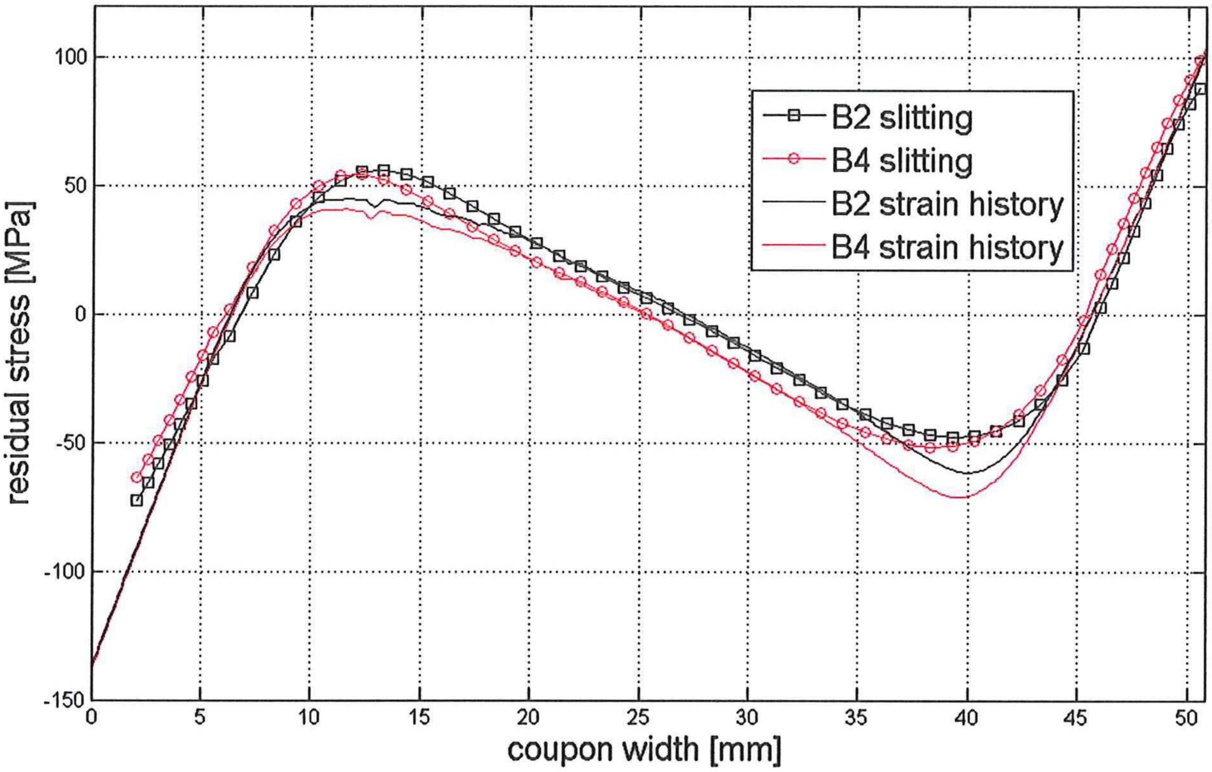

Figure 6.8: Residual stress for coupons B2 and B4 as determined by slitting and bending strain history.

6.1.2.1 Conclusions

It can be concluded that slitting is an effective method to measure 2D residual stresses in metallic coupons within reasonable amount of experimental effort and time. Altough only 2 coupons were slitted the repeatability of the method is considered good, given the close results. The results are believed to be even closer when several coupons are slitted with the same rolling direction.

From the average strain misfits and the inidividual stress uncertainties is is believed that the accuracy of the analysis is better then 15MPa at the start of the cut and drops quickly to values below 2MPa if the cut exceeds 10mm. This uncertainty can be further reduced if more coupons are slitted from the residual compressive side.

As compared to the bending strain method, slitting results match excellent between a=15mm and a=35mm. In this region the bending strain method is believed to be very accurate since this part of the coupon stays in the elastic regime thoughout the complete bending operation. This further enlarges confidence in the correctness of the slitting data. Alltogether the slitting results are believed more accurate than the bending strain results because 1) they do not rely on the individual stress-strain curves and subsequent error magnification 2) there is no need to assume a different E-modulus in tension or compression and 3) the (small) Bauschinger effect is inherently incorporated in the method. In the next section the finite element model is varified against the slitting residual stress distribution.

6.1.3 Residual stress from FE model

A finite element model of the four point bending procedure is made in Abaqus™ 6.11 to mimic the residual stresses. The goal of the model is to match the experimental strains throughout the coupon midline at maximum load and after springback. The residual stress distribution can then be compared to the slitting and strain history data.

To match the experimental strains, various parameters parameters such as contact properties, zero plastic yield point, plastic hardening law, element type & size and boundary conditions play a role. It is therefore not claimed that all parameters match reality (for instance, a friction coefficient of 0.03 between rollers and coupon proved to be optimal, while it is 0.3 in reality). However, if the general behaviour of the FEM model matches with the experiments and the midline strains are very close, it can be assumed that the residuals stress profile over this midline will be accurately modeled. The upcoming sections describe the model and compare FEM outcomes to experimental data.

6.1.3.1 Model overview

Becasuse of symmetry conditions only one half of the coupon has been modeled. The second symmetry plane through mid-thickness has not been used because thickness effects in subsequent crack growth modeling are expected. As shown in Figure 6.9 the specimen is modeled as continuum solid elements and the cylinders are analytically rigid. The steel blocks between the contact points have not been modeled.

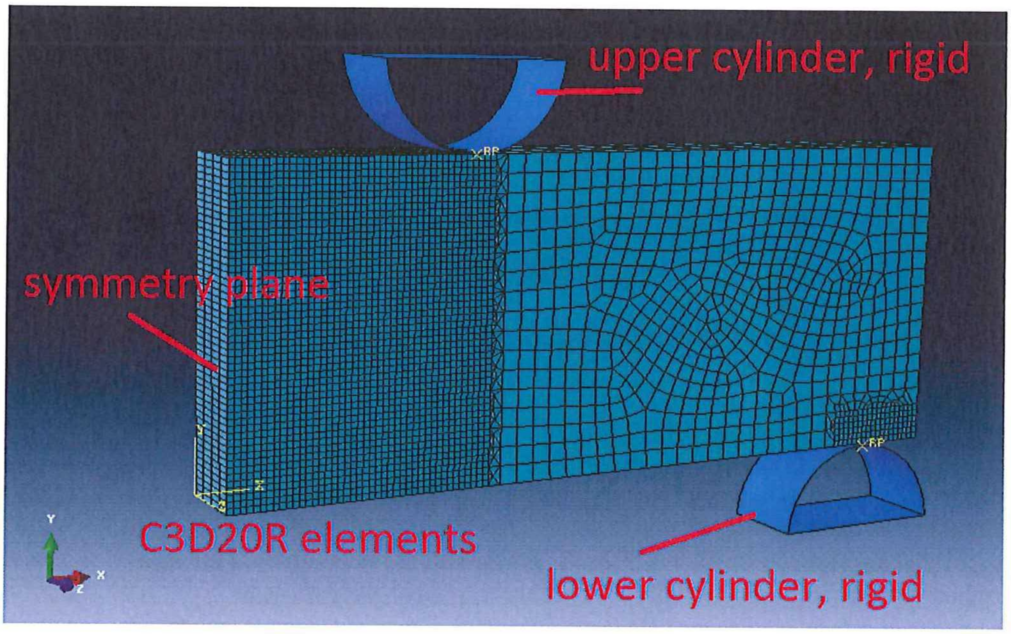

Figure 6.9: General outline of the FE-model which simulates four point bending.

6.1.3.2 Steps and boundary conditions

In Table 6.1 the steps that are used and the evolution of the boundary conditions is shown. In the initial step the first four boundary conditions are created. These BC's are: (1) constraining movement in X-direction at the symmetry plane, (2) fixing one end point in Z-direction to prevent rigid body motion, (3) fix the lower cylinder in space and (4) guide the upper cylinder by only allowing vertical displacement. All these four BC's propagate through all steps. In the 'make contact' step the fifth boundary condition is created which is a small downward displacement (0.2mm) of the upper cylinder to make contact between the cylinders and the beam. In this way, too large strain increments at the contact points are avoided in further analysis. In the 'apply load' step the downward load is applied on the top cylinder to plastically bend the specimen; here the fifth BC is set inactive. The final step simulates springback by removing the applied load.

Table 6.1: Boundary conditions in the FE model.

	step			
BC	**initial**	**make contact**	**apply load**	**springback**
1. symmetry plane	created	propagated	propagated	propagated
2. end point in z	created	propagated	propagated	propagated
3. fix lower cylinder	created	propagated	propagated	propagated
4. guide upper cylinder	created	propagated	propagated	propagated
5. press upper cylinder down		created	inactive	inactive

6.1.3.3 Mesh size and element types

Continuum solid quadratic brick elements (C3D20R) have been used to model the coupon. Reduced integration was selected since only very little difference was observed with fully integrated elements while the required computing force decreased significantly. Between the upper cylinder and the symmetry plane the elements have dimensions of 1x1mm, while a transition is made to 3x3mm elements further outwards to save computing time (see Figure 6.9). A more refined mesh of 0.5x0.5mm elements at the symmetry plane resulted in a drop of only 0.08% in strain along the symmetry plane. Therefore a 1x1mm mesh is found sufficiently small. A transition area of triangular wedge elements is present to keep the brick elements aspect ratio close to 1. Around the contact area of the lower cylinder also 1x1mm elements are used to avoid numerical problems. Finally, the mesh pattern is swept through the thickness with four elements in thickness direction and a total of 11.804 elements.

6.1.3.4 Plastic Hardening

From section 5.1 it has become clear that 7050-T7451 has different plastic hardening characteristics in tension and compression, which should be captured in the FEM model. Unfortunately, Abaqus™ does not support a full stress-strain curve but only the first quadrant. Therefore it has been chosen to use the tensile material data as input.

It was tried to divide the specimen into a tension and a compression zone and material specified accordingly but a jump was found in the residual stress curve around the neutral axis because of differences in E-modulus. This result is not supported by the slitting data and therefore not used. If the E-modulus, however, is set as the average of the two, the specimen behaves as too stiff and midline strains are too low.

As material input Abaqus expects a stiffness and true plastic stress-strain data. From Figure 5.2 no clear point can be identified where the zero plastic strain point should be selected but it should be somewhere around 400MPa. The correct value can be found by playing around with the yield point until the midline strain at maximum load and after springback match the experimental data. By doing so it has been found that 406MPa is an accurate value. The complete plasticity input data can be found in Appendix C.

Because reversed plasticity is present during unloading the Bauschinger effect can play a role. To account for this, plastic hardening rules can be selected in Abaqus. Isotropic, kinematic and combined hardening are most often used. By selecting isotropic hardening the reversed plasticity is equal to the original plasticity and thus no Bauschinger effect is captured. Kinematic hardening assumes linear hardening above yield while combined hardening combines isotropic and kinematic hardening. For the latter two, cyclic strain tests must be performed to obtain the hardening parameters. This data is not available to the author, but the tensile stress-strain data can be used in combined hardening if the option 'half cycle' is selected. To see what this effect is, the model has been run with both isotropic and combined hardening as hardening law and the stress-strain data is extracted.

Figure 6.10 shows that the isotropic hardening model follows the original stress-strain curve and springback is linear. The combined hardening curves show more hardening and also a fully linear springback. From this it can be concluded that the Bauschinger effect does not kick in at unloading in both models. Consequently isotropic hardening is used as hardening model since it follows the original stress-strain curve. It must be

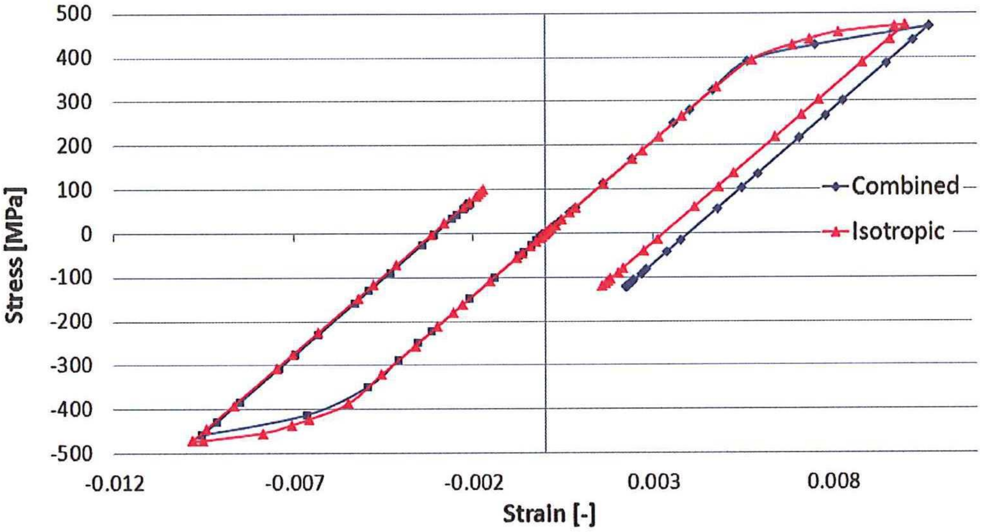

Figure 6.10: Full stress-strain curves for different hardening models in Abaqus.

noted that for this specific coupon geometry and loading, isotropic hardening is most accurate. For other simulations with more reversed plasticity (cold hole expansion, plastic bending up to larger strains) the Bauschinger effect can make combined hardening a better choice.

6.1.4 Model results and validation

In this section the results from the FE model are given and compared to test data.

6.1.4.1 Strains

Figure 6.11 qualitatively compares the longitudinal VIC3d strain of coupon B4 against the strain from the FE model at maximum bending load and after springback.
Both figures show that the iso-strain lines compare very well, except at the contact points. This was expected since the steel blocks between the cylinder and coupon were not modeled in FEM.

A comparison of the DIC strain of coupon B4 and the average is given in Figure 6.12. As discussed in Chapter 5 the VIC3d data shows non-linearity at the extremes which is not correct. The rest of the figure reveals that the FEM strain shows slightly more compression at maximum load and after unloading. To quantify the differences the strains at the top and bottom for each coupon and the FE model are presented in Table 6.2.

Table 6.2: Four point bending top and bottom strains at maximum load and after springback for each coupon, the average and FEM.

Coupon	loaded $\mu\varepsilon_{max}$	loaded $\mu\varepsilon_{min}$	load [kN]	unloaded $\mu\varepsilon_{max}$	unloaded $\mu\varepsilon_{min}$	$\delta_{max}[mm]$	$\delta_{min}[mm]$
B3	10024	-9503	89.2	1429	-1361	2.97	0.72
B4	10117	-9677	88.29	1465	-1515	2.92	0.68
B5	10004	-9618	88.5	1418	-1424	-	-
B6	10056	-9661	88.85	1395	-1385	-	-
B8	10123	-9942	89.87	1531	-1640	-	-
B9	9971	-9752	88.89	1400	-1534	-	-
B10	9994	-9744	89.86	1418	-1529	-	-
average	**10041**	**-9700**	**89.07**	**1437**	**-1484**	2.95	0.70
FEM	**10026**	**-9815**	**89.07**	**1483**	**-1661**	2.51	0.37

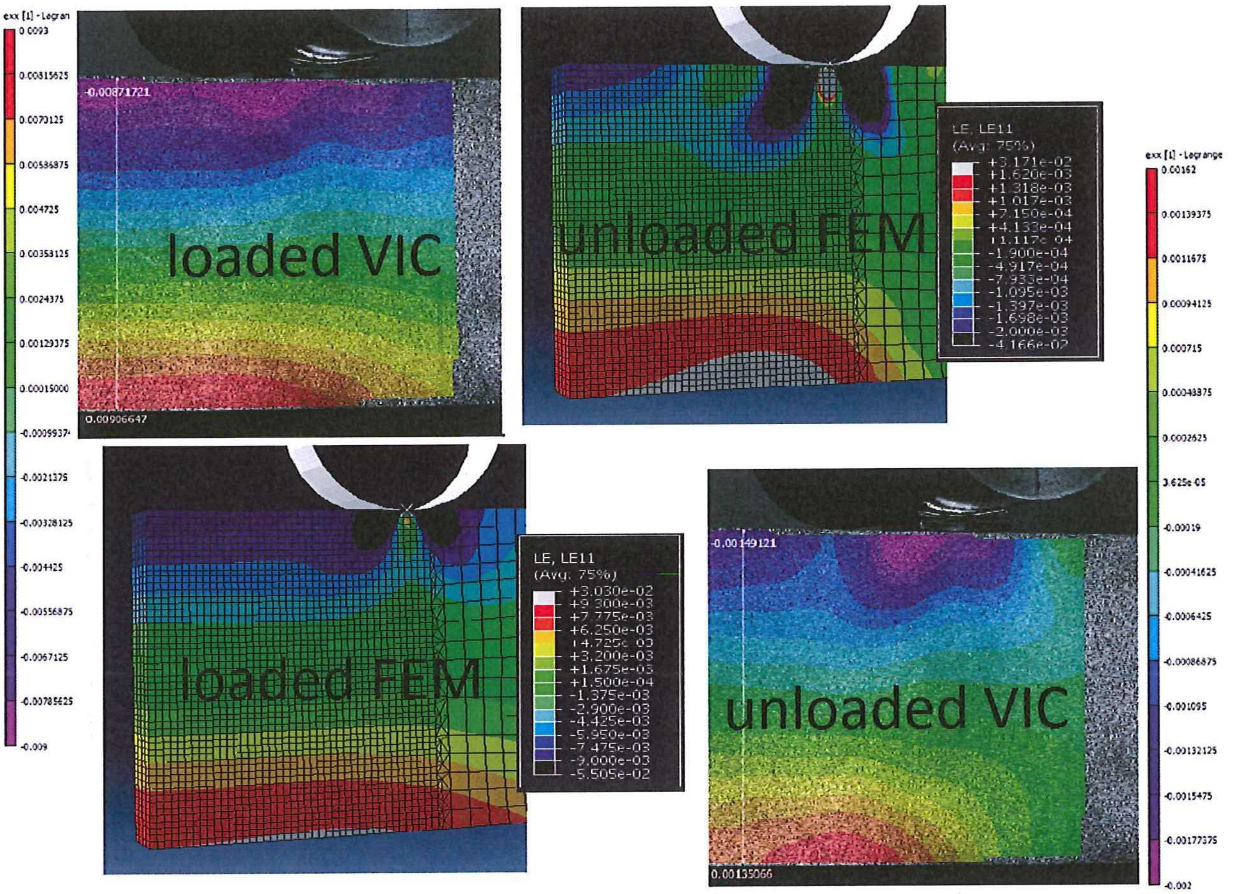

Figure 6.11: The strain distribution in horizontal direction of coupon B4 during four point bending at maximum load (left) and after springback (right). Comparisons are made between digital image correlation and finite elements. Note that each figure has its own legend.

By comparing FEM and the average test data, it can be seen that the FE model predicts too large compressive strains. The main sources in this error are believed to be the definition of zero plastic yield, an infinitely stiff modeled bending framel, friction & contact point indentation and assuming isotropic plastic behaviour. If the yield stress is increased, less plasticity occurs at maximum load and subsequently the springback strain will be smaller, which would make the model more accurate. On the other hand, by increasing the yield stress, the applied force must be increased to reach $10.000\mu\varepsilon$ which is not comform the tests.

An extra check is made by comparing the bottom deflections, see the last two columns in Table 6.2. At maximum load an average deflection of 2.95mm is measured while the FE model gives 2.51mm. This difference is expected and can be explained as compression of the 4 point bending frame, while it is modeled as rigid body. After springback, however, the FE model gives a bottom deflection of 0.37mm while an average of 0.70mm is measured. This difference cannot be explained by frame compression because the applied load is zero; it turns out that curvature of the steel blocks after springback has a large influence on the measured deflection which does not allow for a fair comparison.

6.1.4.2 Residual stress

Now the behaviour of the finite element model has shown to mimic the experimental data accurately, finally the residual stress distribution over the coupon midline can be varified. Longitudinal residual stress over the coupon midline for coupon B2 and B4 from slitting, strain history and the FEM result is plotted in

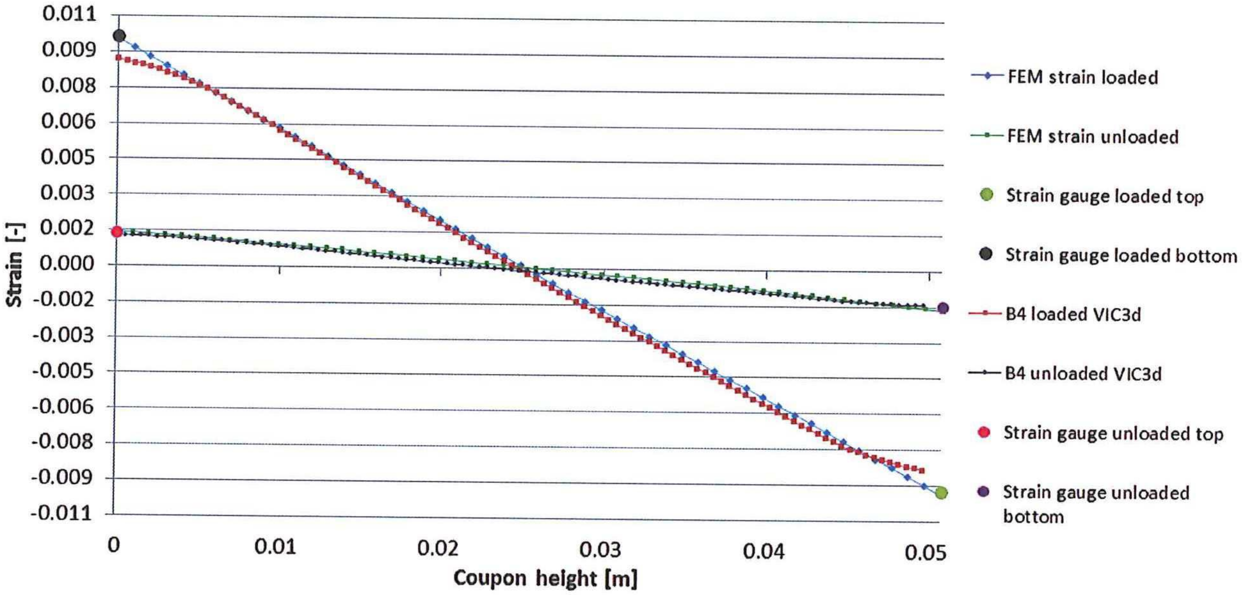

Figure 6.12: The midline strain at maximum load and after springback from the FE model, strain gauges and VIC3d. FEM data and strain gauges show mid-thickness data; VIC3d data is from coupon surface.

Figure 6.13.

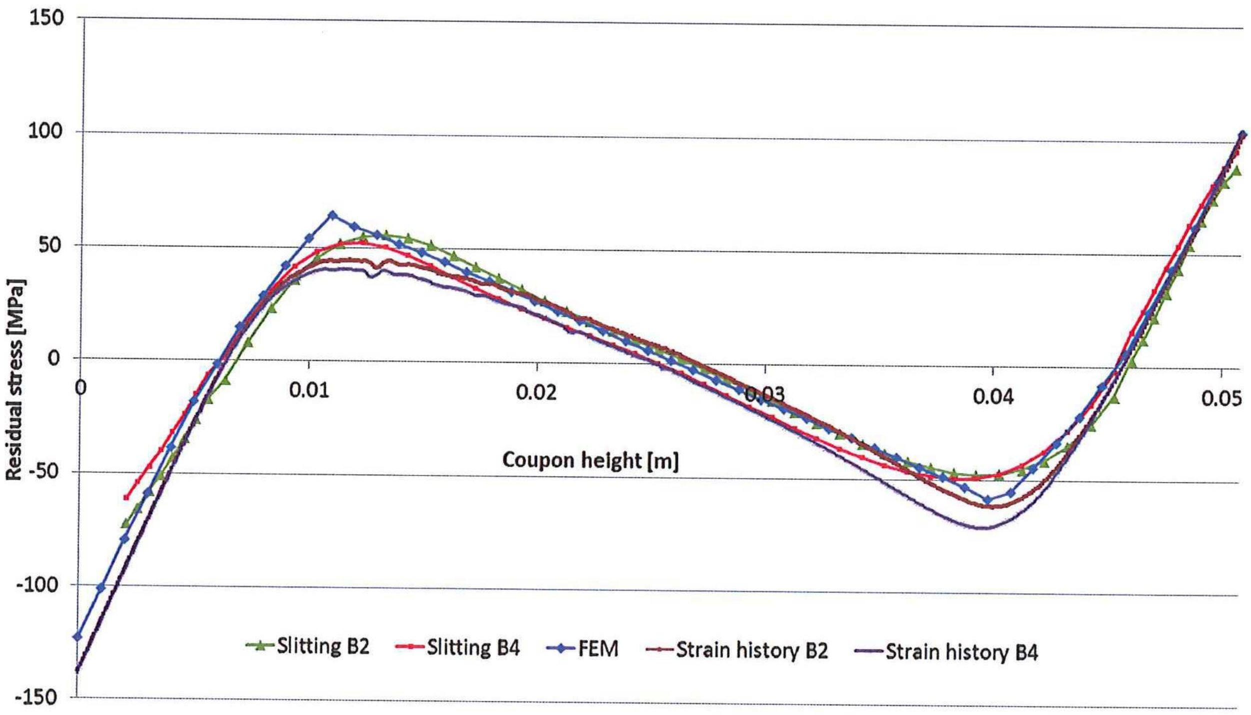

Figure 6.13: The residual stress over coupon midline. Slitting, FEM and strain history compared.

It can be seen that the FEM and slitting data match closely except at the peaks at 0.01m and 0.04m. Here the finite element model predict a distinct transition while the slitting data is more gradual. This is caused by the material definition in Abaqus™ were a sharp transition between elastic and plastic data is present. In reality, however, the material yields more gradually.

In the fully elastic zone, roughly between a coupon height of 0.015m and 0.035m, the FEM stress is lying in between the slitting data of coupon B2 ans B4. Since the FE model is constructed to match the average four point bending results; this is as expected (note that in Figure 6.3 B2 and B4 are the extremes and the average should lie in between). The largest mismatch in stress is found near the compressive side of the coupon. Here slitting B4 gives a stress of -61MPa while FEM gives -70MPa. On the contrary, at the tensile residual stress edge all data matches very well.

6.1.5 Conclusions

In conclusion it can be stated that the three independent residual stress predictions compare well, with most scatter around the internal peaks. The FE model suffers from an idialized material definition while the bending history predictions seem to under- and overestimate stress due to the large difference in tensile and compressive stress-strain data that are used. Residual stress predictions turn out to be very sensitive to the stress-strain input data.

Both the FE model and the strain history predictions do not take any Bauschinger effect into account, but slitting proves that this effect is small. The assumption of fully linear springback seems to slightly overestimate the residual stresses near the coupon ends. Experimental validation of the reversed material behaviour should be performed.

Despite of these shortcomings, it is believed that the FEM results are sufficiently validated by slitting and can be effectively used as foundation to predict crack growth through residual stress fields due to plastic bending. In the next section linear elastic fracture mechanics is employed to make crack growth predictions, based on the above derived residual stress field.

6.2 Crack growth analysis and predictions

As discussed in Section 2.4.1, linear elastic fracture mechanics has been found to be an effective method in residual stress predictions but is criticized by many. A LEFM crack growth prediction is made in this section to varify its applicability. Since the tests with a crack starting from the compressive residual stress side failed, predictions are only made for a crack growing from the tensile side into compressive stress.

The prediction is founded on equations 2.14 and 2.15, which are repeated below.

$$\Delta K = K_{tot-max} - K_{tot-min} = (K_{app-max} + K_{res}) - (K_{app-min} + K_{res}) = \Delta K_{app} \tag{3.14}$$

$$R_{tot} = \frac{K_{tot-min}}{K_{tot-max}} = \frac{K_{app-min} + K_{res}}{K_{app-max} + K_{res}} \neq R_{app} \tag{3.15}$$

In order to arrive at an accurate prediction, baseline crack growth data is required over every stress-ratio R that is 'felt' by the crack tip growing through residual stress. This would however require a huge amount of baseline tests. Therefore Harter-T interpolation is used to calculate crack growth rate at every R-ratio between the available data at R=0.7, R=0.05 and R=-1. In Section 6.2.1 the crack growth test are analyzed to obtain da/dN versus ΔK data. Harter-T interpolation is performed in Section 6.2.1.2. Finally in Section 6.2.2 the predictions are varified against experimental results.

6.2.1 Crack growth rate versus stress intensity factor

From the crack length data of Figure 5.13 the crack growth rate can be extracted at avery point by taking the derivative. Because of measurement errors, scatter in material, branching etc. taking the direct derivative gives very noise results. To smoothen the data the ASTM 7 point polynomial fit method is used to obtain crack growth rates [103] from each crack growth test. For each data point i, a quadratic polynomial is fitted to $i-3, i-2, ..., i+3$ and the derivative at point i is taken as growth rate. For the first and last three points the data is fitted over the first and last seven data points respectively.

The first 1.5mm of crack length is disregarded because of small crack effects. The stress intensity factor is obtained by inserting the effective crack length into the K-solution by Ahmad [107].

6.2.1.1 Baseline coupons

Figure 6.14 shows the crack growth rate versus stess intensity range for all baseline coupons, together with data from the MIL-HDBK-H at R=0.1.

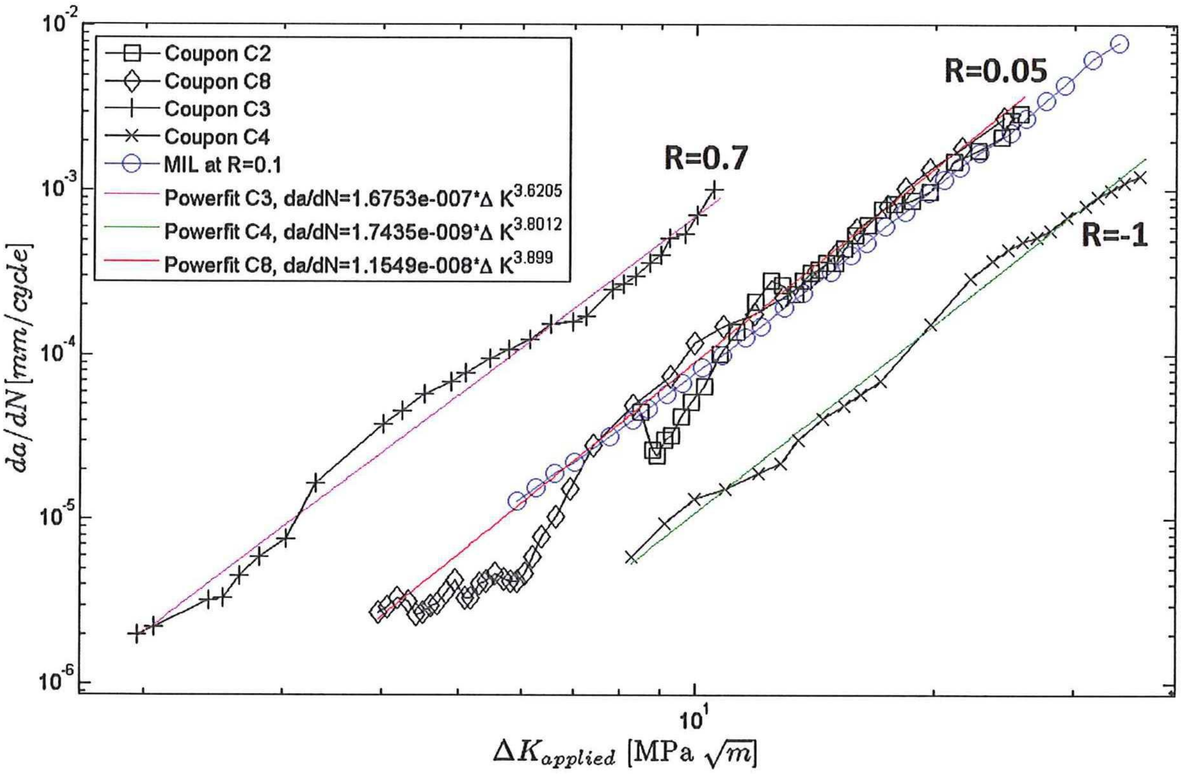

Figure 6.14: Crack growth rate versus applied stress intensity range for the baseline coupons.

The growth rates from coupons C2 and C8 can be compared directly. It shows that above $\frac{da}{dN} = 2 \cdot 10^{-4}$ the lines match very well. At lower crack growth rates, an overload effect is seen for coupon C2 because precracking was not done correctly (see Section 5.4.2) and therefore this part does not allow for validation. It is interesting to note that after this crack retardation a short overshoot is visible.

A powerfit has been plotted over the data from coupon C8 to determine the Paris constants for later crack growth predictions. The fit is within a factor two in $\frac{da}{dN}$ except for the region $5<\Delta K<6.5$ where the measured crack growth rate is considerably lower.

By zooming on this area at the a versus N plot in Figure 6.15c, it can be seen that around N=930k, 1140k and 1250k there are severe discontinuities (both at the left and right side, so they are no measurement errors). It turns out that these discontinuities in growth are excactly at the positions where crack branching occured (Figure 6.15b). By comparing Fig 6.15a) and b) it can be seen that the two large branches coincide with the two dips in growth rate. To eleminate brancing effects, the powerfit has been perfomed over the range $6.8<\Delta K<K_{max}$ and is extrapolated to lower values if needed.

The curves from coupons C3 and C4 show very little scatter and the powerfits lie close to all data points. A clear R-shift can be observed in the data from coupons C3 and C4 which were fatigued at R=0.7 and R=-1 respectively; the shift to the right (from R=0.05 to R=-1) is however smaller then the leftward shift. This is as expected since lowering P_{min} does hardly affect the crack growth rate any more after a certain level has been reached.

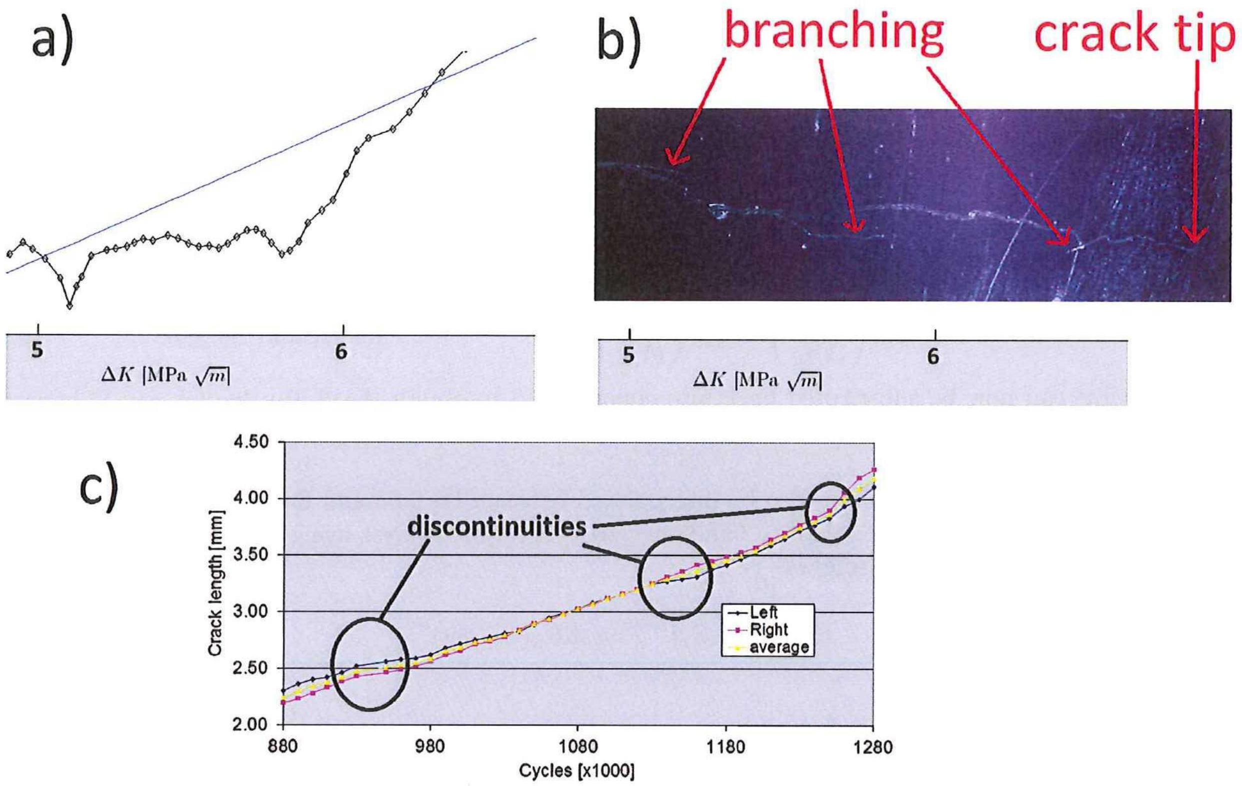

Figure 6.15: a) Zoom-in on the crack growth curve around ΔK=6 showing a severe retardation in growth rate compared to powerfit. b) Branches coincide with reduction in growth rate. c) Crack growth curve around ΔK=6 showing discontinuities at both left and right surface.

As discussed in Section 2.3.4 the baseline data can be collapsed into a single $\frac{da}{dN}$-ΔK_{eff} curve. The data at R=0.05 and -1 collapses well if the equation by Schijve [42] is used. The data points from R=0.7, however, do not collapse well. If this data is assumed closure free and thus U is set to 1 it collapses very good to the other two lines. All data then collapses to within a growth rate factor 2, exept the above described data that was affected by branching.

As a check, MIL-HDBK-JH data at R=0.1 is plotted together with the measured data. The MIL data lies to the right of the curve from coupon C8 while it was expected to be slightly left because the stress ratio is higher. This difference cannot be explained because both fatigue lines are obtained from 12.7mm thick coupons in LT direction at room temperature. The only difference is that the MIL data is obtained from C(T) coupons, while coupon C8 is tested in SEN(T). Furthermore, it is not known how the crack length was measured at the C(T) specimen; it is possible that a clip gauge or the voltage drop method was used (as often with C(T) specimens). Nevertheless the data from C8 is assumed to be correct since it is varified by C2.

6.2.1.2 Harter-T interpolation

The Harter-T method, or formerly known as the point-by-point Walker shift, is used to capture the R-shift of ΔK at a certain crack growth rate by means of the Walker equation. The Walker equation is an enhancement of the Paris equation to account for the R shift:

$$\frac{da}{dN} = C[\Delta K(1-R)^{m-1}]^{n} \tag{6.4}$$

At a fixed crack growth rate, for two baseline points the Walker equation can be equated as

$$\frac{da}{dN} = C[\Delta K_1(1-R_1)^{m-1}]^n = C[\Delta K_2(1-R_2)^{m-1}]^n \tag{6.5}$$

which reduces to

$$[\Delta K_1(1-R_1)^{m-1}] = [\Delta K_2(1-R_2)^{m-1}] \tag{6.6}$$

which shows that n and C drop. Solving for m yields

$$m = 1 + \left[log_{10}\left(\frac{\Delta K_1}{\Delta K_2}\right)/log_{10}\left(\frac{(1-R_2)}{(1-R_1)}\right)\right] \qquad \text{for } R_1 \text{ and } R_2 \geq 0 \tag{6.7}$$

This m value can now be substituted back into equation 6.6 to obtain the ΔK value for any R between R_1 and R_2. The value of m is thus a measure of the rate of R-shift: the larger m becomes the smaller the shift and vice versa.

Because the baseline data must also be interpolated between R=0.05 and R=-1, negative stress ratios must be handled as well. The method to handle negative R-ratios involves using K_{max} instead of ΔK and switching the m component as follows:

$$K_{max}(1-R_1)^{1-m} = \Delta K_2(1-R_2)^{m-1} \tag{6.8}$$

Now solving for m yields

$$m = 1 + \left[log_{10}\left(\frac{\Delta K_{max1}}{\Delta K_2}\right)/log_{10}\left(\frac{(1-R_1)}{(1-R_2)}\right)\right] \qquad \text{for } R_1 < 0 \text{ and } R_2 \geq 0 \tag{6.9}$$

The first step in the analysis is to find the crack growth curve for R=0. This is done by finding m in Equation 6.7 and extrapolation from baseline data at R=0.7 and R=0.05 by means of equation 6.6. The reason for not using interpolation between R=0.05 and R=-1 is that this would give a discontinuity around R=0.05 because K_{max} is used instead of ΔK for negative R ratios. When the R=0 curve has been found, interpolation between this line and R=-1 by means of equations 6.9 and 6.8 gives the remaining ΔK values. Figure 6.16 shows the results of the Harter-T interpolation for several intermediate R ratios.

6.2.1.3 Residual stress coupons

Coupons C5B3, C10B8 and C11B10 were all tested with the crack growing from the residual tension side at R=0.05, R=-1 and R=0.7 respectively. This allows for a direct comparison between these coupons and the baseline coupons who where tested at the same loads. Figure 6.17 depicts the crack growth rate versus applied stress intensity range for all six coupons.

The first and most obvious observation is that the crack growth rate at R=0.05 and R=-1 is initially higher than the baseline curves, then crosses the baseline data and finally dives underneath for the remaining part. At R=0.7, on the contrary, the residual stress data stays slightly above the baseline data. Only a small residual stress effect is visible here. The final observation is that for low ΔK values, baseline and stress bearing data at R=0.7 and R=0.05 lie very close to each other, while the two R=-1 curves are separated by a factor 8.

6.2.1.4 FE model

With the finite element model as described in Section 6.1.3 a crack growth rate prediction is made for coupon C5 at R=0.05. The J-integral is employed in combination with superposition.

While the four point bending model has a mesh size of 1x1mm at the symmetry plane, the mesh size is decreased to 0.127mm within the first mm from the symmetry plane. Mesh refinement did not change the outcome of J-integral solutions in this configuration.

To simulate crack extension, the symmetry plane was succesively released from its constraint. Crack lengths between 1.5mm and 25mm were modeled with a step size of 2mm. After crack extension first

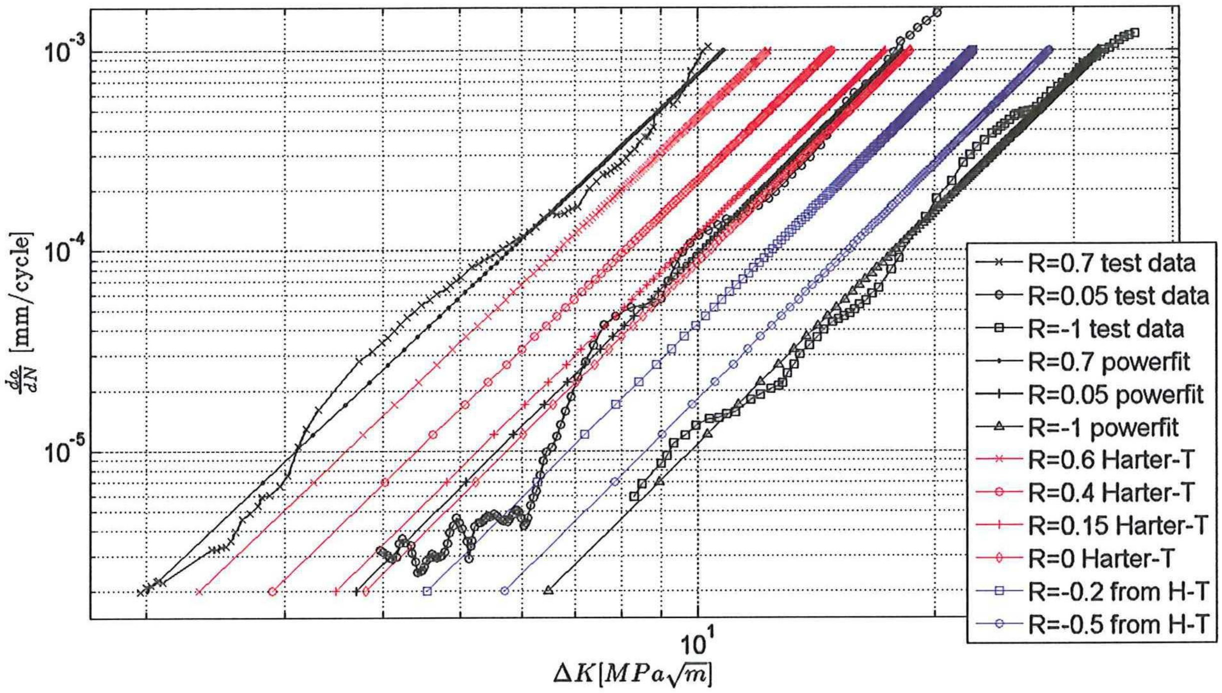

Figure 6.16: Harter-T method used to calculate ΔK values for R ratios between baseline data. Baseline together with interpolated data at various R ratios shown.

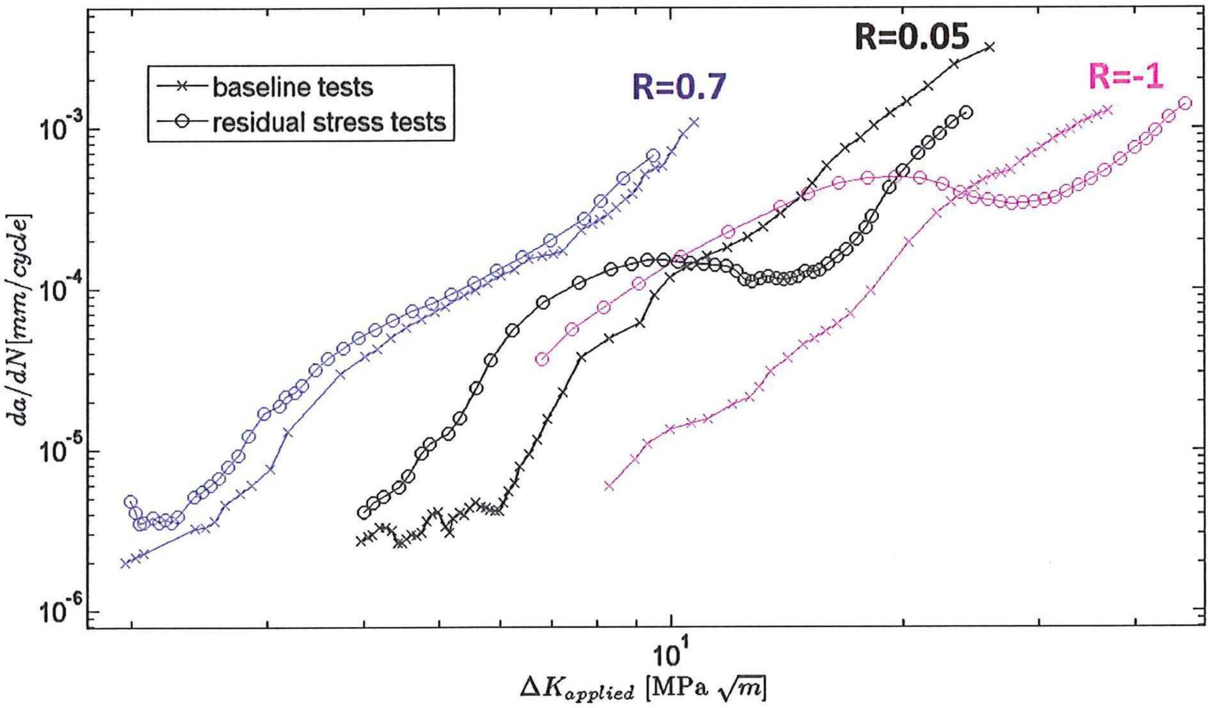

Figure 6.17: $\frac{da}{dN}$ versus ΔK for baseline coupons and residual stress bearing coupons at different R ratios.

P_{min} of 1.75kN was applied and then P_{max} at 35kN in a following step. Boundary conditions prohibited sideways movement at the grip area. At the end of those two steps the J-integral was extracted over the first six contours. Modeling cyclic behaviour by first applying P_{max} and then P_{min} provided excactly the same outcomes for J_{min}. This extra step was thus not performed in the final solution.

It was found that the first contour gave a considerably lower value as compared to contours 2-6. Therefore this contour was disregarded; contours 2-6 were within 0.32% from the mean such that path independence was found. In the upcoming results the value of contour 3 was taken as this lied very close to the average of contours 2-6.

Because the average J value over the thickness was required, straight cracks were defined and only two elements were modeled over the thickness. By modeling four elements over thickness, the average J value was increased by only 0.14%. If was found that J is maximum at mid-thickness and lower at the specimen edges. This effect was not further investigated.

The J-intrals were translated to K values by using $K = \sqrt{EJ}$. This can, however, only been done if the crack tip plastic zone effect is sufficiently small. Therefore an elastic and elastic-plastic model were employed to quantify this effect. The blue and black data points in Figure 6.18 show that both solutions match closely. As expected the (small) difference increased with increasing plastic zone size. The maximum difference was 0.32% at a crack length of 25mm ($K = 25.4MPa\sqrt{m}$). Because of this small difference it was valid to translate from J to K by the E-modulus.

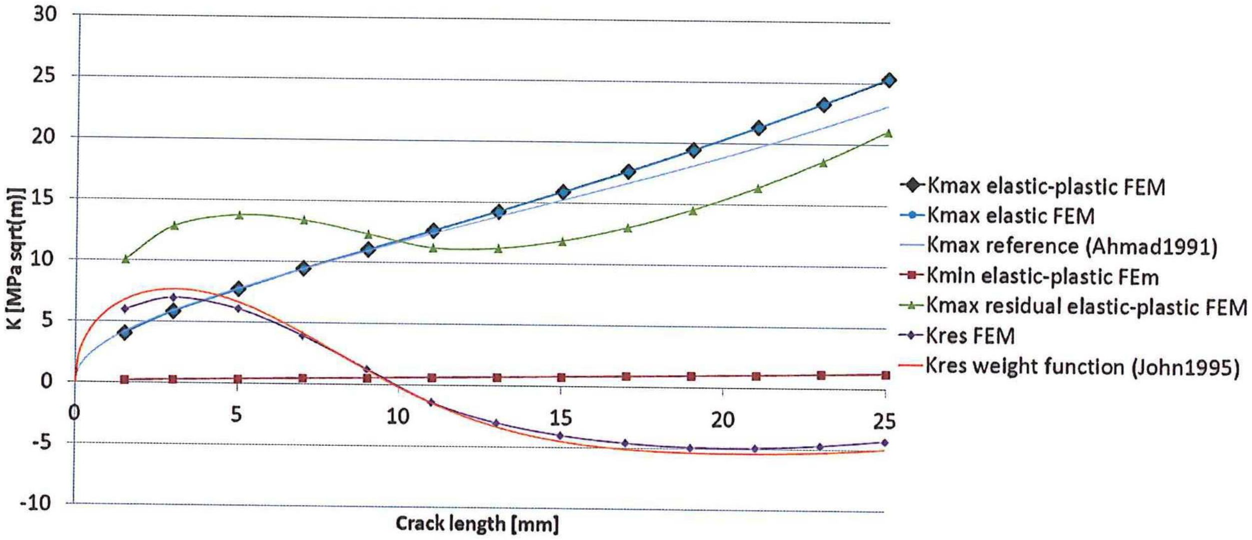

Figure 6.18: K solutions from FE analysis compared to reference solutions.

To varify the model, the solution by Ahmad et al. [107] that was used throughout this thesis is also plotted in Figure 6.18. As can be seen, up to a crack length of 10mm the solutions match very well. Beyond this crack length, however, the solutions converge. As Ahmad et al. used plane strain elements, it was expected that this solution would give slightly higher K values, while it gives lower K values. This discrepancy might be due to a fit error by Ahmad et al. as found earlier in this thesis. This could also explain the difference in crack growth rate between the baseline coupons and the MIL data (Figure 6.14).

The residual stress intensity factor was obtained by subtracting the baseline K_{max} solution from the residual stress bearing K_{max} solution. Both curves are plotted in Figure 6.14. It can be seen that K_{res} is initially positive (in tension) while after 10mm the solution goes negative (in compression). This result matches closely to the plotted weight function solution from John et al. [108] for the slitting residual stress. Any difference is mainly due to the difference in residual stress between the slitting results and FEM model.

It is noted that K_{res} can also be obtained by modeling crack extension through the residual stress field without applying loads. In the compressive residual stress zone, however, the J-integral does not go subzero but increases again after reaching zero. The correct J value is then obtained by multiplying the J value by -1. This method requires the crack tip element displacement to be monitored continuously to see whether the crack tip is in compression or tension, which is not very practical.

This section has shown that the finite element method is a convenient way to calculate residual stress intensity factors and is at least as accurate as classical weight function solutions. This has been shown for a well-defined and one dimensional residual stress field and if small scale yielding is obeyed. To obtain a solution, K_{max} has be found for the residual-stress-free configuration and for the residual-stress-bearing configuration. Superposition then provides the residual stress intensity factors. Crack growth predictions from slitting, strain history and FEM are presented in the next section.

6.2.2 Crack growth predictions

A flowchart of the prediction procedure is presented in Figure 6.19. For a given crack length a, K_{max} and K_{min} from applied loading are found and $K_{residual}$ is determined by the weight function. These values are superimposed to get ΔK_{tot} and R_{tot} from which the latter is input for the Harter-T interpolation. For this R_{tot} the crack growth curve is constructed and the accompanying $\frac{da}{dN}$ is found for the given ΔK_{tot}. Now this data point is plotted and crack length is increased by da to get the next data point.

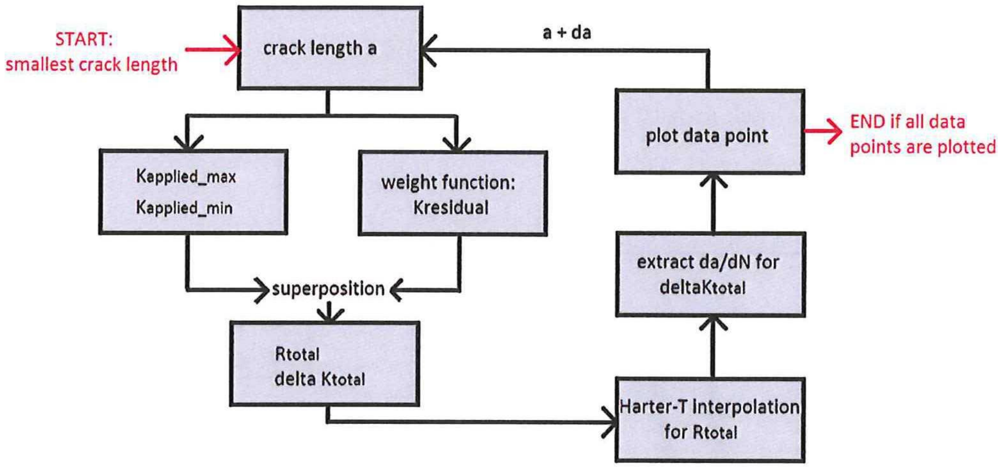

Figure 6.19: Flowchart of the crack growth predictions.

For each coupon two predictions have been made. For the first prediction the residual stress from the strain history method is used. The second prediction uses the slitting residual stress from coupon B4. The finite element prediction has only been made for R=0.05. Figure 6.20 shows the predicted crack growth rates. The red lines indacate the borders between interpolation and extrapolation. The extrapolated data is only shown for completeness but conclusions are not drawn from this data.

From the crack growth rates the crack length versus number of cycles is obtained by integration and presented in Figure 6.21. The FEM crack path has not been calculated because of the very large step size of 2mm that wa used.

It can be seen that the predicted crack length for C10 at R=-1 follows the test data well upto 5mm and then significantly slows down. This has to do with the underestimation of growth rate for R-values below zero. The slitting prediction matches better than the strain history prediction.

If we look at the data for coupon C5 at R=0.05 both predictions are conservative. This is due to an underestimation of growth rate for the first 5mm of crack length. For cracks longer than 5mm the strain history prediction is very good, while the slitting stress predicts too little growth retardation.

For coupon C11 at R=0.7 the predictions are also conservative because the growth rate exceeds the test data below $\Delta K = 3.5$. For K values above 3.5 the prediction follows the experimental data well.

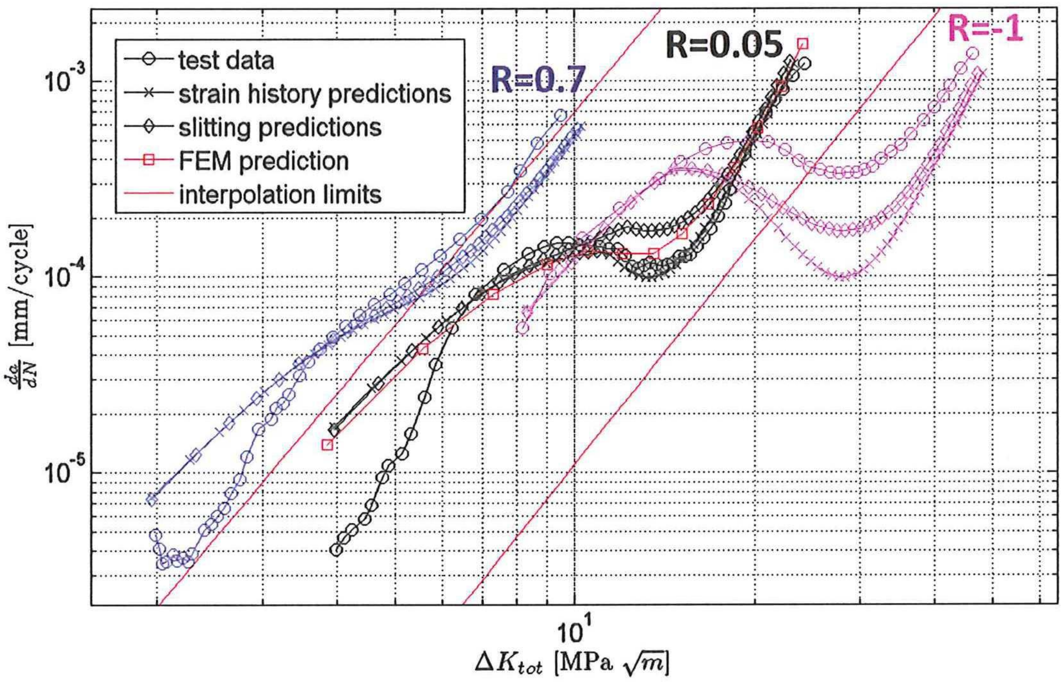

Figure 6.20: Crack growth rate predictions at different applied stress ratios.

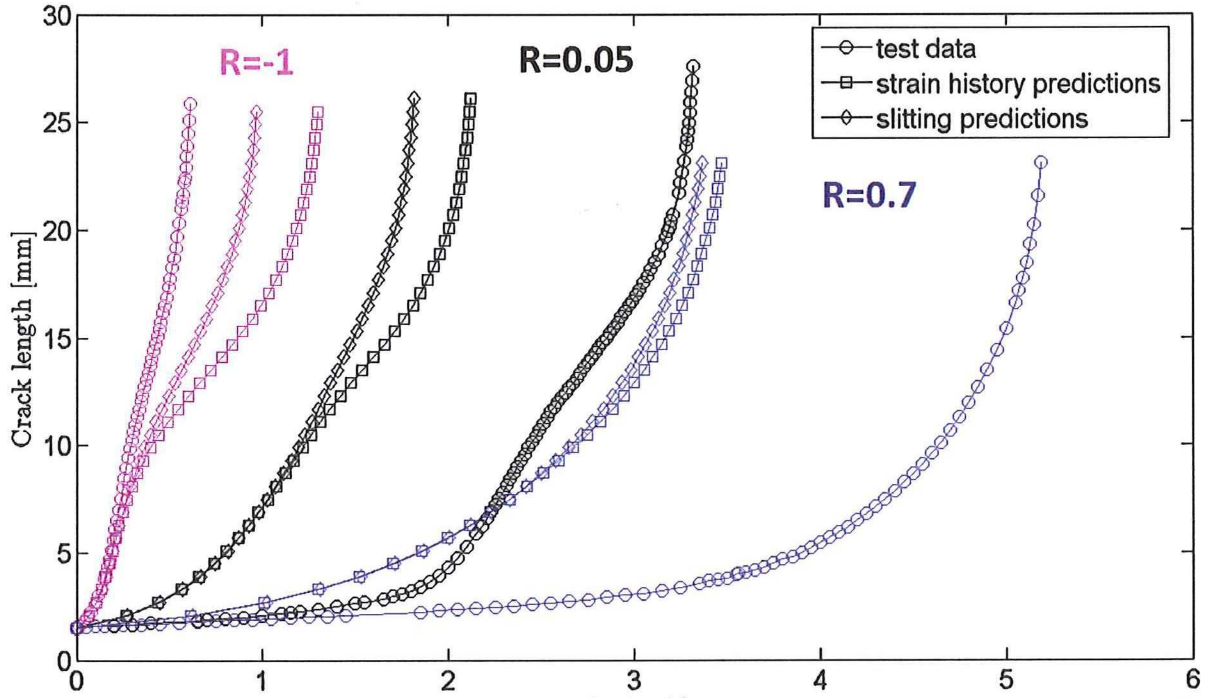

Figure 6.21: Crack length predictions at different applied stress ratios.

6.2.3 Discussion

All crack growth predictions are based on constant amplitude baseline data with increasing K values. Due to compressive residual stress, however, crack growth rates (and thus K) goes down with increasing crack length and prediction might be conservative. It can be seen from Figure 6.20 however that in the compressive residual stress zone five out of six growth rate predictions are non-conservative, instead of conservative. This indicates that the error from history effects is small and the change in residual stress is gradual enough to make predictions from CA tests.

The mismatch in prediction at short crack length is also partly due to residual stress relaxation from the starter notch. By cutting the starter notch, Eigenstrain is removed and thus residual stress relaxes; becasue this is not accounted for, predictions are made with a too high residual stress estimate. Especially at short crack lengths where K_{res} is large as compared to $K_{applied}$, crack growth rate predictions are very sensitive to the residual stress magnitude. This partly explains why the growth rate predictions are too high for short cracks. In finite element analysis this error can be avoided by explicitly modeling the starter notch.

The second reason why the predictions are too high for short cracks is the use of powerfits. Using powerfits reduces experimental scatter but it also removes intrinsic crack dependency on δK as well as crack retardation due to branching. Because crack growth data in MIL-HDBK-5H for 7050 aluminum averages out to a loglog-linear line it is assumed that intrinsic crack growth behaviour is close to loglog-linear. If the branching effects would not have been excluded from the baseline test at R=0.05, the crack growth prediction for short cracks at R=0.05 and R=0.7 would have been better.

A third and less obvious reason for increased crack growth rates can be the effect of plastic prestraining (see Section 2.3.4.1). Because the side with tensile residual stress is plastically compressed during four point bending, crack growth behaviour might be slower as compared to non-plasticized material. No data on this has been found in the literature unfortunately.

Next to this, an error is expected to come from the Harter-T interpolation. Because only three baseline results are used for the R-shift calculations, the R-shift is smeared out over a large range of R ratios. This is clearly visible by the sharp drop (kink) in the predictions at R=0. Here the R-shift parameter m is changed from the average between 0.7>R>0 to the average between 0>R>-1. Adding more baseline sets at intermediate R ratios would increase accuracy. Furthermore, it is advised by the AFGROW manual not to use the method below R=-0.5 because the R-shift would not captured accurately below this value.

From a crack closure point of view it was expected that at high R ratios the residual stress effect would be small since P_{min} is close to the crack opening load and subsequently ΔK_{eff} is little affected by residual stress. On the other hand, for intermediate and low R ratios a substantial part of the load cycle is fully closed and ΔK_{eff} is greatly largely by superimposed residual stress. This is confirmed by the test data. The finite element model can be employed to study the effect of residual stress on the crack opening load. Crack growth predictions by means of the effective stress intensity range can than be made and compared to superposition.

From an energy point of view it can be argued that residual stress will have an effect on crack growth, even if the load cycle is fully above crack opening. This is because as the crack grows, the internally stored elastic energy is partly reduced. In Appendix A a short discussion with some preliminary calculations is given.

Despite the above mentioned shortcomings, it is believed that the test results and the LEFM predictions provide a good estimate of residual stress effects on crack growth. It has proved the effect of relatively low residual stresses can be clearly seen in test results and that superposition of applied and residual stress intensity factors is able to follow the trend of the tests. The finite element model from which K_{min} and K_{max} values are obtained gives equally accurate results, but may be improved because of: 1) crack tip plasticity effects can be included, 2) remote crack closure can be simulated, 3) starter notch effects are taken into account 4) thickness effects are inherently included if a solid model is used, 5) 2D crack front shapes can be simulated and 6) residual stress redistribution from plastic strain accumulation can be accounted for by modeling cyclic loading.

Chapter 7

Conclusions

The general conclusions from this thesis are:
1.) LEFM and superposition can accurately account for residual stress in crack growth predictions if the stresses are well-defined and one dimensional.

2.) For thick aircraft sections with multidirectional residual stresses and loading conditions, this one directional method must be extended to predictions in 2D.

3.) The Finite Element method can be effectively employed to model crack growth by means of superpostition. For this, the residual stress field through the structure of interest must be measured accurately and introduced in the model either by modeling the stress introduction process or via Eigenstrains. The J-integral can be used if the crack tip plastic zone is small.

The conclusions that can be drawn from the material characterization tests are:

- The compressive E-modulus of aluminum 7050-T7451 is 72.4GPa while the tensile modulus is 70.2GPa. Taking the average value as material stiffness gives accurate residual stress predictions.
- Strain hardening in compression and tension differs significantly and should be taken into account to determine residual stresses.

The conclusions that can be drawn from the four point bending tests are:

- The strain distribution over the coupon height is linear up to at least 1% outer fiber strain.
- Even with steel blocks friction between loading noses and specimen is significant and no perfect bending moment is present.
- The four point bending test is highly consistent if care is taken to align the frames, position the coupon and keep loading rate constant. For a target strain of $10.000\mu\varepsilon$ an average difference from the mean of $49\mu\varepsilon$ can be obtained.
- The out-of-plane deflection can be as large as $\pm 150\mu\varepsilon$ with an average difference from mean of $\pm 74\mu\varepsilon$.

The conclusions that can be drawn from the slitting tests and data reduction are:

- The slitting method is consistent if an EDM machine is used.
- The residual stresses measurements in the elastic zone are very accurate, as validated by the strain history method.
- The computational effort for data reduction is small if compliance functions are available.
- The average of all stable Legendre orders should be taken to increase the stability of near-edge stresses.
- If slitting is started from the residual tensile side, no closure is present throughout the test if a 0.25mm wire is used. The wire thickness can be decreased to 0.15mm without closure.

The conclusions that can be drawn from the FE model are:

- The four point bending operation can be accurately modeled with moderate computational effort by using 20 node bricks, reduced integration and frictional contact.
- The residual stress field from an FE model is very accurate, as validated by slitting.
- A mesh size of 1mm at the symmetry plane is small enough to make accurate residual stress predictions.
- Isotropic hardening is more accurate than kinematic hardening and/or combined hardening as long as reversed yielding is absent.
- Remote crack closure can be predicted. Crack opening displacements agree good with the measured values.
- The simplification of a distinct yield point in Abaqus makes the residual stress prediction less accurate around the internal peaks.

The conclusions that can be drawn from the crack growth tests are:

- A relatively small residual stress field of 100MPa at the edges and 50MPa as internal peaks is sufficient to make residual stress effects visible.
- The SEN(T) configuration is not effective with a coupon thickness of 12.7mm because of significant non-symmetric crack growth. Non-symmetric crack growth is less significant at high and low stress ratios.
- Constant amplitude tests in the SEN(T) configuration are not effective to validate crack growth from the compressive residual stress side because of small scale yielding limits.
- Short coupons increase non-symmetric crack growth because of an increased bending moment from misalignments.
- Crack curvature is a function of coupon thickness, material characteristics, applied loading and residual stress.
- Overloads of 16MPa are sufficient to visualize the crack front in 7050 aluminum at a magnification of 5000x. At small crack lengths marker loads are difficult to reconstruct due to the coarse grain structure. A repetitive block of 5-3-2 overloads is helpful for visualization.
- Strong non-symmetric crack growth is likely to occur in a 3 point bending configuration because of the inherent non-stability.
- The effect of imperfect clamping is larger than the effect of non-symmetric residual stress on non-symmetric crack growth.

The conclusions that can be drawn from the crack growth analysis and predictions are:

- The effect of residual stress is very small if the applied loading is at R=0.7. At R=0.05 and R=-1 the effect is significant.
- Harter-T interpolation is an effective means to calculate R shifts for $R>0$ if insufficient baseline data is available. For $R<0$ interpolation between R=0 and R=-1 does not capture the R shift accurately.

Chapter 8

Recommendations and future work

Recommendations:
1.) Crack growth from the compressive residual stress side should be tested at higher stress, such that symmetric growth is stimulated. Earlier large scale yielding must be accepted. A second option would be to increase the depth of the starter notch or to reduce the residual stresses.

2.) Repeat slitting by now starting from the compressive residual side to reduce the uncertainty in residual stress and to complete the data.

3.) Quantify the reversed plastic behaviour of 7050-T7451 aluminum by testing the full stress-strain range curve up to different maximum strain levels. Reversed yielding (if any) can then be incorporated in the bending strain prediction. Also the most accurate hardening model in Abaqus can now be selected.

4.) For better residual stress predictions a material with equal modulus in tension and compression can be used in further experiments.

5.) Perform the crack growth tests in the eccentrally loaded single edge crack tension configuration with pin loaded holes. Coupon bending due to clamping is no issue in this configuration. FE calculations show that residual stresses do not redistribute due to hole drilling if the ASTM E647 dimensions are obeyed.

Future work:
1.) Perform more crack growth tests on identically prepared specimens to quantify the scatter in residual stress crack growth data.

2.) Study the effect of residual stress relaxation due to accumulation of plastic strain in the wake of the crack due to cyclic loading.

3.) Investigate the effect of multi directional residual stresses on (mode II) crack growth.

4.) Model and validate crack path predictions through more complex residual stress fields such as non-uniform through-thickness stresses.

5.) Complete the baseline data set with more tests at $R<0$ to make more accurate predictions. Validate similitude for $R<0$ data.

Appendix A

Crack growth from an energy point of view

By acknowledging that residual stresses arise from elastic strain energy induced by four point bending, which is partly released by crack extension, an effect on crack growth must be present for every loading ratio even if the complete load cycle is above the crack opening load. Nowadays such effects are named as 'K-max effects' but no explanation is given.

To make a qualitative description of this effect, during testing coupon C10 the crosshead displacement and applied force were monitored for three intermediate crack lengths, being 5mm, 16.23mm and 24.94mm. Figure A.1 shows the displacement-load curve on the left and the residual stress distribution with crack tip positions in the right graph.

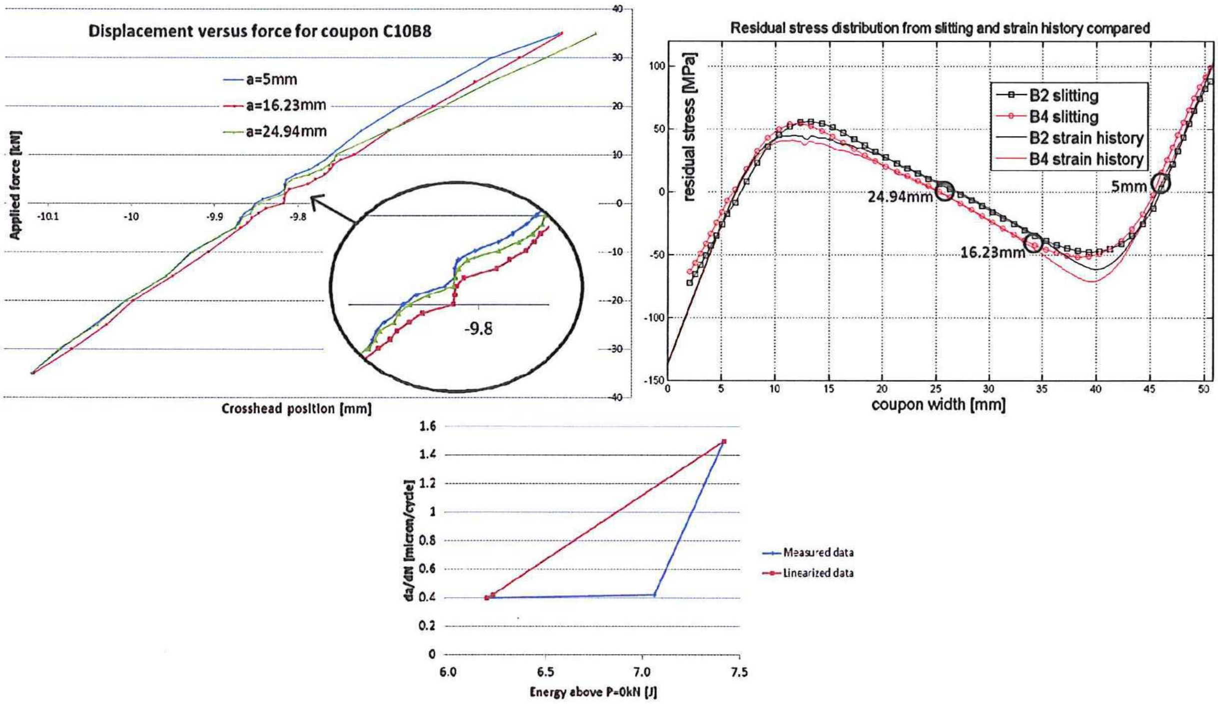

Figure A.1: Left: crosshead displacement versus applied load for coupon C10 at three crack lengths. Right: crack tip locations indicated on residual stress distribution (note that tensile residual stress starts at right side). Bottom: positive part of cyclic energy against crack growth rate for the three data points.

The first observation is that at -35kN all three data points overlap; this is expected since the crack is fully closed here. Close to maximum load the line from a=16.23 and a=24.94mm are linear. The line for a=5mm is however non-linear between 25kN and 35kN. This is probably an effect of slip under the grips.

It was found in subsequent tests that the uploading and unloading curves often do not match, whereas they should coincide at high forces.
If now the area under the positive force range (it is for now assumed that the compressive part does not contribute to crack growth) is plotted against crack growth rate at all three crack tip positions it is found that this relation is non-linear. If however the last data point for a=5 is adjusted such that the displacement-force line is linear at P=35kN, the energy versus crack growth point fall on one line (see Figure A.1 bottom). This would indicate that there is a linear relation between cyclic applied energy and crack growth rate, even if residual stresses are present. By looking at the magnification it can be seen that for a=5mm when the crack tip is in residual tension the force-displacement curve is shifted up. For a=16.23mm, where the crack tip is in residual compression, the curve is shifted down. In this way, residual stress changes the size of the area under the force-displacement curve.

No hard conclusions can be drawn from this cheated result, but there is a potential that positive cyclic energy can be a measure of crack growth. To make further investigation more accurate it is suggested to take middle tension specimens with firmly bolted clamping such that non-linearities in displacement-force curves are minimized. In this way, slip, grip plasticity and fretting do not add to the energy term.

Appendix B

Test program

This chapter contains a detailed description of the test procedure that will be carried out as experimental part of this thesis. The test plan is written such that each step can be repeated by third.

B.1 General procedure

The objective of this test plan is to describe a procedure to introduce well characterized residual stresses into a rectangular aluminum 7050-T7451 coupon by means of four-point-bending. The residual stress distribution resulting from the bending operation is measured by means of strain gauges, digital image correlation and slitting. Thereafter fatigue tests will be performed on both stress-free and stress carrying coupons to quantify residual stress effects on crack growth.

The material elastoplastic stress-strain curves will first be determined by a tensile and a compressive test and will serve as input to an FE model to calculate residual stresses from the strain gauge data. Furthermore, the bending operation will be modeled and validated against the experimental data. Once the material properties are known, a total of 16 specimens will be cut from a single plate. The coupons are used to obtain baseline crack growth data, slitting data and residual stress bearing crack growth data.

B.2 Tensile test

The tensile stress-strain properties are measured according to the ASTM-E8M test standard. The specimen layout is depicted in Figure B.1.

The specimen will be loaded in a static tensile test machine and will be tested until fracture. The loading rate is set to be 5MPa/s which is within the limit of 11.5MPa/s according to ASTM-E8M. With a grip length of 70mm and an stiffness of 71.1GPa [117] this gives a loading rate of about 0.005mm/s and a total extension at yielding of 0.46mm, which corresponds to a strain of 0.65%. With an estimated ultimate strength of 524MPa and cross sectional area of 158mm^2, the maximum estimated force that is required to break the specimen will be around 83kN. The test is performed on a Zwick 250kN static machine with internal force recording and the strain will be measured with a clip-on extensiometer over a gauge length of 50mm. The steps to be performed are:

1) Clean the specimen grip area and the fixture bearing blocks with acetone to remove all traces of grease and oil
2) Accurately measure the with and thickness of the specimen along the gauge section and determine the minimum gauge dimensions. All dimensions are measured to the nearest 0.02mm.
3) Mark the original gauge length (50mm) by making a small indent or using ink and measure this length to the nearest 0.05mm.
4) Place the specimen in the test fixture and ensure concentric loading.
5) Attach the extensometer on the specimen with a gauge length of 50mm at the center of the gauge area.
6) Set the extension controlled speed of the testing machine to 0.005mm/s or to the nearest value. The

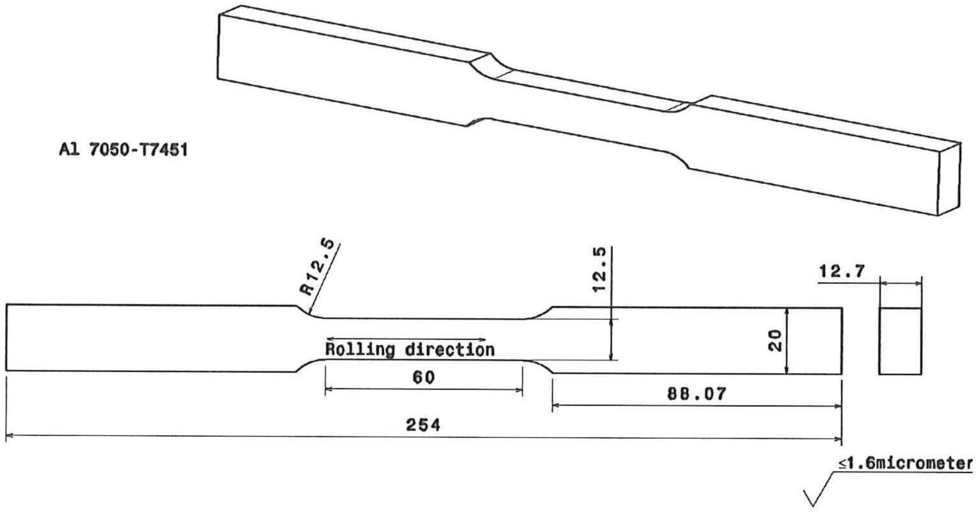

Figure B.1: Details of the tensile specimen. All dimensions in mm.

speed will be constant during the first part of the test up to a displacement of 0.7mm (1% strain).
7) After a displacement of 0.7mm has been reached and yielding is recorded, the strain rate can be increased to 0.05mm/s to strart the second part of the test.
8) At an elongation of 3.6mm (6% strain) the extensometer can be removed.
9) The test continues until failure, this is expected to be at 9% strain which comes down to a total displacement of about 7mm.

To determine the compressive properties with a sufficient confidence the test will be performed five times. An average of the results will be the final result.

B.3 Compression test

The compressive elastic-plastic properties of the 7050 aluminum are determined with a static compression test according to the ASTM-E9 [100] standard. Cylindrical specimen are used with a length/diameter of three. In this way premature buckling is avoided and the specimen is long enough to accurately determine the E-modulus and yield point. Details are found in Figure B.2.

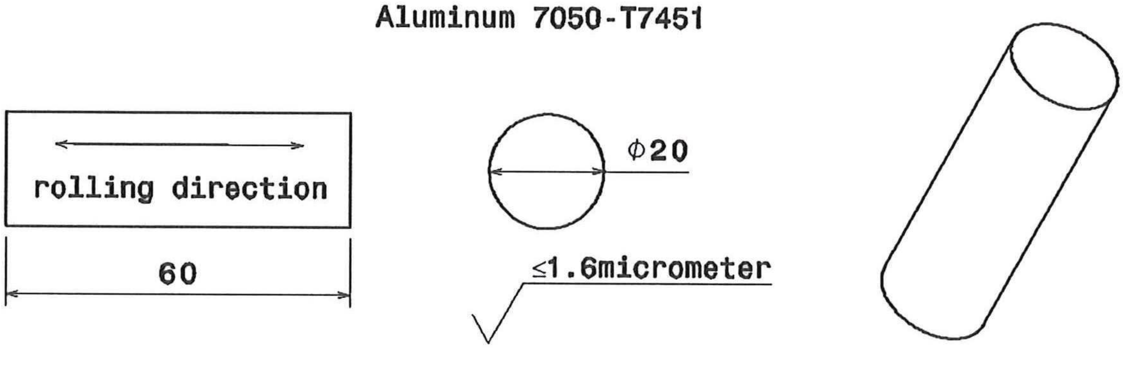

Figure B.2: Details of the compression specimen. All dimensions in mm.

The specimen will be positioned in a static Zwick 250kN servohydraulic machine with both flat ends between two flat loading blocks. The specimen will be compressed at constant displacement speed until a strain of at least 6% has been reached. The diameter of the specimen is 18mm and the length is 60mm. The ends are flat and parallel within 0.0005mm/mm. With a cross sectional area of $254.4mm^2$ and an estimated ultimate strength of 524MPa [117] the maximum loading force will be about 65kN.

The loading rate is set such that the specimen is tested at 10 millistrain per minute and is kept constrant throughout the test. While the specimen has a total length of 60mm the displacement of the test machine will be set at 0.6mm/min. The maximum displacement of the test machine will be about 3.6mm.

2 strain gauges are used to measure the strain since no extensiometer is available at the compression bench. The steps to be performed are:

1) Clean the specimen grip area and the fixture bearing blocks with acetone to remove all traces of grease and oil
2) Measure the specimen diameter over the gauge length to the nearest 0.02mm and calculate the average diameter.
3) Lubricate the bearing surfaces with TFE fluorcarbon sheet or available equivalent lubricant.
4) Place the specimen in the test fixture and **align** the specimen to ensure concentric loading.
5) Attach the Peekel strain amplifier to the strain gauges.
6) Set the test machine to a displacment controlled speed of 0.6mm/min.
7) The test ends if a total displacement of 6mm (10% strain) has been reached.

To determine the compressive properties with a sufficient confidence the test will be performed three times. An average of the results will be the final result.

B.4 Four point bend test

The bending specimen will be positioned in a 150kN compression machine according to ASTM-D6272 [118] as shown in Figure B.3.

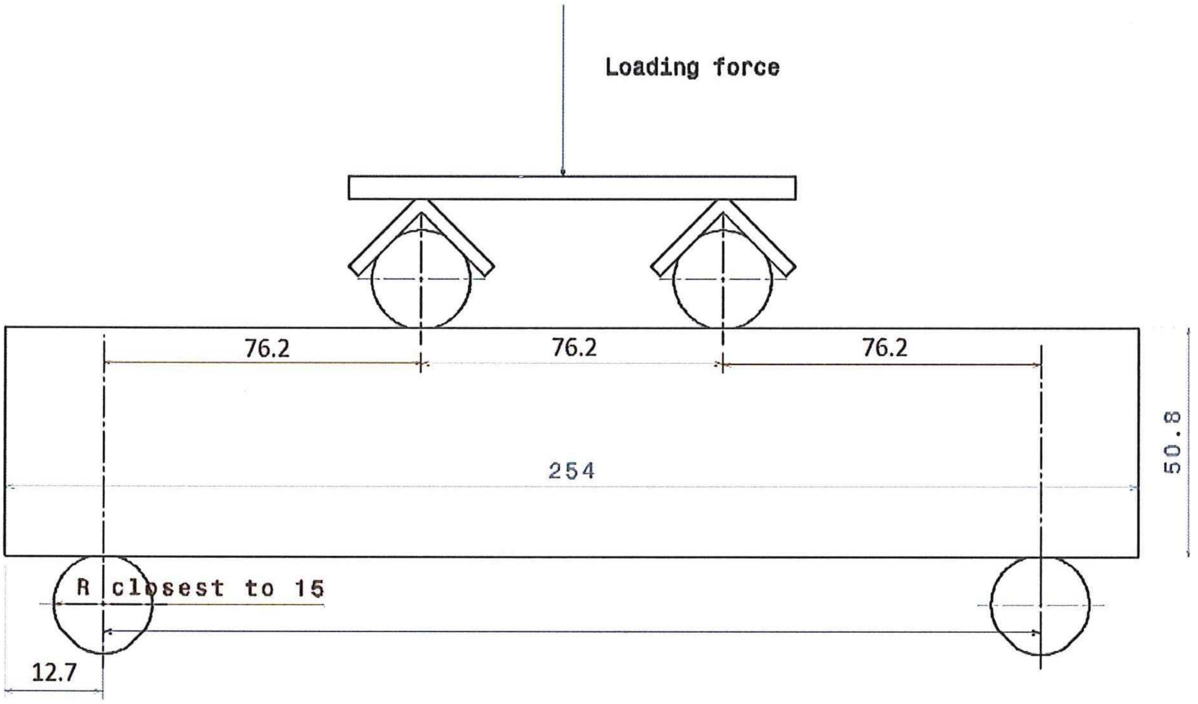

Figure B.3: Details of the bending set-up. All dimensions in mm.

The specimen is positioned between four fixed loading noses. The two upper noses are separated by 76.2mm; the two bottom noses are 228.6mm apart. The radius of the load noses is 30mm.

The test is manually performed under strain control up to a total outer fiber strain of 10.000$\mu\varepsilon$. After the maximum strain has been reached, the unloading starts directly untill a force of 0kN has been reached.

The DIC camera's (3D) are installed in front of the specimen and ensured is that the field of view is slightly larger than the area between the two inner loading noses. Pictures are taken every 2kN during the complete loading and unloading procedure.

Strain gauges of 5mm length are installed as depicted in Figure B.4. Gauge 1 is mounted exactly opposite to gauge 2 and gauge 3 is mounted exactly opposite to gauge 4 while gauge 5 is positioned at an equidistance from the vertical midline. The first two are measuring the top and bottom extreme fiber strain. The results of 3 and 4 should give equal results and indicate out of plane bending if differences are noted. Data from gauge 5 can be compared to the strains at postion 4 such that asymmetric loading can be identified.

Next to the strain gauges an extensometer and two optic fibers are mounted on the specimen. The extensometer is positioned against the bottom of the specimen next to strain gauge 1. The optic fiber is glued over the top and bottom surfaces over a length of approximately 60mm between the two inner contact points.

The experimental steps are:

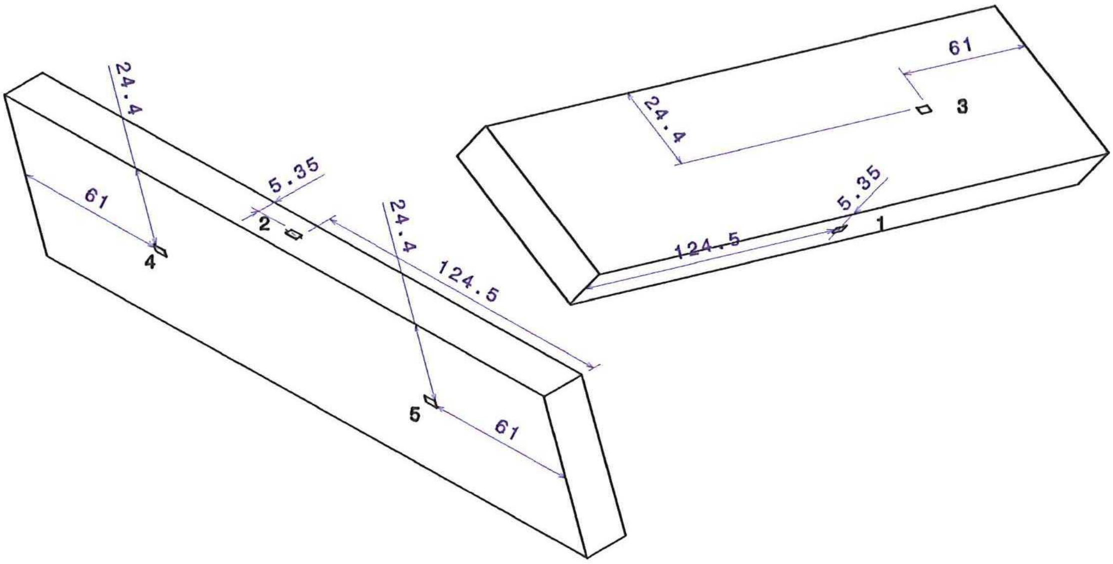

Figure B.4: Positions of the strain gauges during the bending test. All dimensions in mm.

1) Measure the specimen dimensions to the nearest 0.005mm before applying paint and/or strain gauges.
2) Set the bending fixture to the dimensions as given in Figure B.3.
3) Apply the speckle pattern and strain gauges on the specimen and highlight the positions of the loading nosed with a marker.
4) Mount the specimen in the bending fixture, ensure that it is centrally positioned and apply a preload of 5N.
5) Mount the deflectometer at the bottom midpoint and set to zero. Also zero the strain gauges and bending machine.
6) Position the DIC camera such that the area of interest (70mm width x 50.8mm height) is visible plus some space for deflection (about 3mm) and solder the strain gauges to the wires.
7) Start the DIC device at a speed of one photo per second.
8) Start the bending test at a load controlled constant rate of 500N/sec. This is equivalent to a midspan deflection of about 0.54mm/min. At a load of 93kN (after 3 minutes) the maximum load is reached and the deflection is hold still for about one minute (deflection controlled).
9) Unload the specimen at a constant rate of 500N/sec untill zero load is reached.
10) Carefully retrieve the specimen from the machine without damaging the surface.

B.5 Slitting

The slitting operation will be performed on coupons B1, B2 and B4 by EDM wire cutting. The slit (0.25mm) has to be cut from the tensile side of the coupon towards the other edge, up to a depth of 49mm, see Figure B.5.

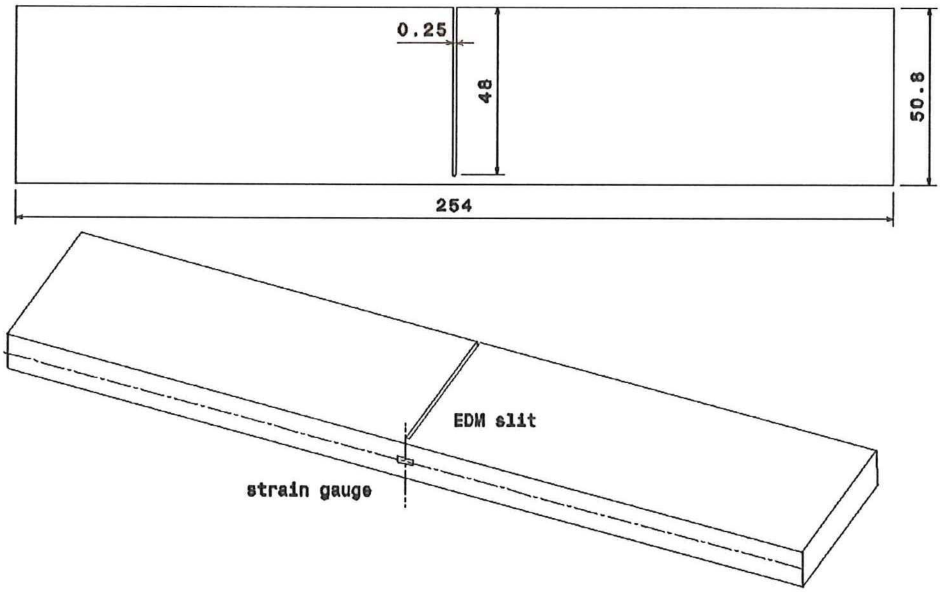

Figure B.5: Schematic of the slitting operation. All dimensions in mm.

The experimental steps are:

1) A Peekel strain amplifier is attached to the gauge.
2) Wiring and strain gauge are waterproofed by waxing.
3) Fix the coupon to the EDM machine and make sure that it has a 90° angle to the cutting direction.
4) EDM settings are such that a finishing quality is obtained.
5) After every 1mm cut increment the machine is turned off and a strain reading is done after stabilization.
6) After 5mm cutting, the width of the slit is checked to make sure that no slit closure has occured.
7) If the slit has closed, cut back to make the cut wider and continue from the last measurement point.
8) Repeat point 5-8 until a cut of 49mm is reached.

B.6 Matlab script for slitting reduction

The MATLAB™ script for data reduction of the slitting experiment. Thanks to Michael Prime for providing the script. The comments refer to equation numbers in [119].

```
% series.m, anything after a "%" is a comment
clear; clc; close all;
load epsilon_Tom.txt; % Text file with m strain data, 1 value each line
load a_Tom.txt; % Text file with m slit depths
load C_Tom.txt; % Text file with m x n C matrix
load P_Tom.txt; % Text file with m x n P matrix

m=length(epsilon_Tom);
N=size(C_Tom,2); % maximum value of n

for n=1:N; % loop over possible expansion orders
    Cn=C_Tom(:,1:n);  % Take submatrix of C for fit order < N
      Pn=P_Tom(:,1:n);  % Take submatrix of P for fit order < N
    A=pinv(Cn)*epsilon_Tom; % least squares fit using MATLAB functionality,
              %could use A=(((Cn'*Cn)^-1)*Cn')*epsilon  to look like Eq. 5
    sigma(:,n)=Pn*A;  % stresses per Eq. 3
    epsilon_fit=Cn*A; % fit strains per Eq. 4
    u_epsilon_bar(n)=norm(epsilon_fit-epsilon_Tom)/sqrt(m-n);  % avg strain uncert. & ...
        misfit per Eq. 13 (just for plotting)
      u_epsilon=sqrt(m/(m-n))*(epsilon_Tom-epsilon_fit);  % Individual strain ...
          uncertainties, Eq. 14
      B=pinv(Cn);  % Eq. 5. Again, could replace with B=(((Cn'*Cn)^-1)*Cn')
      V=B*diag(u_epsilon.^2)*B'; % Eq. 11
    s(:,n)=sqrt(diag(Pn*V*Pn')); % Eq. 8
end

for n=2:N-1;
     s_model(:,n)=std(sigma(:,n-1:n+1)')'; % Model error per Eq. 16
     s_total(:,n)=sqrt(s(:,n).^2+s_model(:,n).^2);
            % Total error per Eq. 17
     s_total_bar(n)=norm(s_total(:,n))/sqrt(m); % Avg total error
end

% select minimum total error :
[minimum_s_total_bar,ntemp]=min(s_total_bar(2:N-1));
n_star=ntemp+1 % Because   min   starts at 2

sprintf('%s','    x     stress     +-')
fprintf('%8.3f %8.2f %8.3f\n',[a_Tom sigma(:,n_star) s_total(:,n_star)]')

figure(1);
plot([2:N-1],s_total_bar(2:N-1),'-o')
title('uncertainty'),xlabel('n');

figure(2);
plot([1:N],u_epsilon_bar,'-o')
title('average strain misfit'),xlabel('n');

figure(3);
errorbar(a_Tom,sigma(:,n_star),s_total(:,n_star))
title(sprintf('n = %i',n_star)),xlabel('x'),ylabel('stress');

figure(4);
plot(a_Tom,epsilon_fit,'-o')
title('strain fit'),xlabel('cut depth'),ylabel('strain [micron]');
hold; plot(a_Tom,epsilon_Tom,'-x')
legend('strain fit', 'measured strain','Location','NorthWest')
```

Appendix C

Plasticity input data for finite element model

This appendix contains the tensile plastic stress-strain data which was used as input for the Abaqus model. Data from the dogbone tension test was converted to true stress and true strain data by assuming uniform deformation during the test. First column is stress [Pa], second column is plastic strain [-].

```
397026916 0
416960459 0.000377067
435762460 0.000801845
452235171 0.001322101
464170997 0.002152755
468447338 0.003275132
470837682 0.004884856
472612645 0.00660499
474336790 0.008339981
476118751 0.010060113
477989770 0.01176546
479927129 0.013414746
481928188 0.01501414
483980322 0.016599205
486022794 0.018158248
488092667 0.019714863
490128336 0.02126906
492140005 0.022820844
494145602 0.024346855
496061034 0.025847207
497933340 0.027368611
499765235 0.028916782
501521189 0.030427719
503207875 0.031959569
504869680 0.033489076
506438583 0.035027808
507946762 0.036564176
509352899 0.038103949
510716013 0.039641355
511976147 0.041187891
513202906 0.04274351
514347983 0.044313894
515428374 0.045887534
516417917 0.047447283
517341274 0.049021703
518177273 0.05060503
518975437 0.052208582
519710345 0.053798221
520374229 0.055413655
520970104 0.057049102
521542175 0.058687524
522023966 0.060311993
522458468 0.061950709
522834279 0.063603595
523176831 0.065253755
523434883 0.066934788
523670011 0.06861859
523821379 0.070316301
523955234 0.072011135
524038822 0.073703101
524061331 0.075414416
```

Bibliography

[1] S.J. Findlay and N.D. Harrison. Why aircraft fail. ISSN: 13697021 Elsevier Science Ltd., 2002.

[2] D.W. Hoeppner. Fretting fatigue considerations in holistic structural integrity based design processes (holsip)- a continuing evolution. Tribology International44 (2011) 13641370.

[3] P.J. Withers. Residual stress and its role in fatigue failure. Rep. Prog. Phys. 70, pp.2211-2264, 2007.

[4] L. Edwards. Influence of residual stress redistribution on fatigue crack growth and damage tolerant design. Materials Science Forum Vols. 524-525 (2006) pp 363-372.

[5] M.E. Fitzpatrick and L. Edwards. Fatigue crack residual stress fields interactions and their implications for damage tolerant design. JMEPEG (1998) 7:190-198.

[6] G. Glinka A.K. Vasudevan, K. Sadananda. Critical parameters for fatigue damage. International Journal of Fatigue 23 (2001) S39S53.

[7] J. Schijve. Fatigue of structures and materials. Springer media, ISBN-13: 978-1-4020-6807-2, 2009.

[8] M. Li G. Shi A. Beltempo R. Rutledge M. Yanishevsky M. Martinez, B. Rocha. Load monitoring of aerospace structures utilizing micro-electro-mechanical systems (mems). Proceedings of the ASME 2012 Conference on Smart Materials, Adaptive Structures and Intelligent Systems. September 19-21, 2012, Stone Mountain, Georgia, USA.

[9] J.C. Newman D.H. Stuart, M.R. Hill. Correlation of one-dimensional fatigue crack growth at cold-expanded holes using linear fracture mechanics and superposition. Engineering Fracture Mechanics 78 (2011) 13891406.

[10] C. J. Lammi and D. Lados. Effects of processing residual stresses on fatigue crack growth behavior of structural materials, experimental approaches and microstructural mechanisms. Metallurgical and Materials Transactions A-Physical Metallurgy and Materials Science, 43A(1), 87-107, 2012.

[11] W. Konig P. Leskover J. Peters H.K. Tonshoff E. Brinksmeier, J.T. Cammett. Residual stresses - measurement and causes in machining processes. Annals of the CIRP Vol. 31/2/1982.

[12] P.J. Withers and H.K.D.H. Bhadeshia. Residual stress part 2 - nature and origins. Materials Science and Technology, April 2001,Vol.17, 366-374.

[13] P.J. Withers and H.K.D.H. Bhadeshia. Residual stress part 1 - measurement techniques. Materials Science and Technology, April 2001,Vol.17, 355-365.

[14] William D. Callister Jr. Materials science and engineering an introduction. John Wiley and sons, New York, NY, ISBN-13: 978-0-471-73696-7, 2007.

[15] A.P. Berens P.D. Huber D.A. Skinn, J.P. Gallagher and J. Smith. Damage tolerance design handbook. Wright-patterson Air Force base, Ohio: University of Dayton Research institute, prepared for Air Force Wright Aeronautical Laboratories., 1994.

[16] D.V. Nelson. Effects of residual stress on fatigue crack propagation. ASTM STP 776, American Society for Testing and Materials, 1982, pp. 192-194.

[17] A.P. Parker. Stress intensity factors, crack profiles and fatigue crack growth rates in residual stress fields. STM STP 776, American Society for Testing and Materials, 1982, pp.13-31.

[18] R.C. Mcclung. A literature survey on the stability and significance of residual stresses during fatigue. Fatigue Fract Engng Mater Struct 30, 173205, 2007.

[19] D.W. Hammond and S.A.Meguid. Crack propagation in the presence of shot-peening residual stresses. Engineering Fracture Mechanics Vol. 37, No. 2, pp. 373-387, 1990.

[20] C. Woodward P.J. Withers A. King, A. Steuwer. Effects of fatigue and fretting on residual stresses introduced by laser shock peening. Materials Science and Engineering A 435-436, 12-18, 2006.

[21] Huimin Xie Bing Pan, Kemao Qian and Anand Asundi. Two-dimensional digital image correlation

for in-plane displacement and strain measurement: a review. Meas. Sci. Technol. 20 (2009) 062001 (17pp).

[22] M.B. Prime. Residual stress measurement by successive extension of a slot: The crack compliance method. Applied Mechanics Reviews Vol. 52, No. 2 pp. 75-96 1999.

[23] D.J. Smith M.J. Pavier, C.G.C. Poussard. Effect of residual stress around cold worked holes on fracture under superimposed mechanical load. Engineering Fracture Mechanics 63 (1999) 751-773.

[24] J. Kleiman Y. Kudryavtsev and H. Polezhayeva. Ultrasonic measurement of residual stresses in welded elements of ship structure. Applied Mechanics and Materials Vol. 70 (2011) pp 273-278.

[25] C. Noyan and J.B. Cohen. An x-ray diffraction study of the residual stress-strain distributions in shotpeened two-phase brass. Materials Science and Engineering, 75 (1985) 179-193.

[26] T. Mura. Micromechanics of defects in solids. Kluwer Academic Publishers, Dordrecht, The Netherlands, ISBN 90-247-3256-5, 1987.

[27] J.D. Eshelby. The determination of an elastic field of an ellipsoidal inclusion and related problems. Proc.R. Soc. A 241 376-396, 1957.

[28] Xu Song. Modelling residual stresses and deformation in metal at different scales. Doctoral thesis, Department of Engineering Science University of Oxford, 2010.

[29] P. Holdway F.A. Kandil J. Shackleton M.E. Fitzpatrick, A.T. Fry and L. Suominen. Determination of residual stresses by x-ray diffraction issue 2. Measurement Good Practice Guide No. 52, 2005.

[30] J. A. Nairn. Energy release rate analysis for adhesive and laminate double cantilever beam specimens emphasizing the e!ect of residual stresses. International Journal of Adhesion and Adhesives 20 59-70, 2000.

[31] D. Akbari R. Alderliesten M. Farahani, I Sattari-Far. Numerical and experimental investigations of effects of residual stresses on crack behavior in aluminum 6082-t6. J Mechanical Engineering Science 226(9) 2178-2191, 2012.

[32] R. Marissen. Lecture slides day 1 of the course advanced fracture mechanics, ae4634, tu delft. Blackboard, 2012.

[33] J. Pan Y.C. Hou. A fracture parameter for welded structures with residual stress. Computational Mechanics 22 (1998) 281288 Springer-Verlag 1998.

[34] G.R. Irwin. Linear fracture mechanics, fracture transition and fracture control. Engineering fracture mechanics, 1968 Vol.1. ppl 241-257.

[35] M.R. Ling and J. Schijve. Fractographic analysis of the crack growth rate and shear lip development of 2024t3 specimens under simple variable amplitude loading. Report LR-566, Delft University of Technology, Delft, 1988.

[36] J. R. Rice. A path independent integral and the approximate analysis of strain concentration by notches and cracks. Journal of Applied Mechanics, vol. 35, pp. 379-386, 1968.

[37] G.A. Webster Y. Lei, N. P. O'Dowd. Fracture mechanics analysis of a crack in a residual stress field. International Journal of Fracture 106: 195216, 2000.

[38] F. Erdogan P. Paris. A critical analysis of crack propagation laws. THE AMERICAN SOCIETY OF MECHANICAL ENGINEERS. April 11, 1962. Paper No. 62WA-234.

[39] R.G. Forman. Study of fatigue crack initiation from flaws using fracture mechanics theory. Engineering fracture mechanics, 1972. Vol.4. pp. 333-345.

[40] J.W. Cardinal L.C. Williams R.G. Forman, V. Shivakumar and P.C. McKeighan. Fatigue crack growth database for damage tolerance analysis. U.S. Department of Transportation Federal Aviation Administration. Report number: DOT/FAA/AR-05/15, 2005.

[41] W. Elber. The significance of fatigue crack closure. Damage tolerance in aircraft structures, ASTM STP 486, pp. 230-242, 1971.

[42] J. Schijve. Some formulas for the crack opening stress level. Engineering fracture mechanics, Vol 14. pp 461-465, 1981.

[43] J.C. Newman Jr. A crack-closure model for predicting fatigue crack growth under aircraft spectrum loading. ASTM STP 748, 1981, pp. 53-84.

[44] TAI SHAN KANG and H. W. LIU. The effect of pre-stress cycles on fatigue crack growth-an analysis of crack growth mechanism. Engineering fracture mechanics, 1974, Vol. 6, pp631-638.

[45] J. Schijve. The effect of prestrain on fatigue crack growth and crack closure. Report VTH-203, 1975.

[46] Leonardo B. Godefroid Kassim S. Al-Rubaie, Emerson K.L. Barroso. Fatigue crack growth analysis of pre-strained 7475t7351 aluminum alloy. International Journal of Fatigue 28 (2006) 934942.

[47] R. Sherman. The effect of residual stress on crack propagation in hy-80 steels. Interim report, N00014-70-C-0265, office of naval research, Washington D.C., 1971.

[48] J.K. Sharples J.H. Underwood, L.P. Pook. Fatigue crack propagation through a measured residual stress field in alloy steel. US Army armament research and development command, Watervliet, NY, AMCMS No. 36525000204, Pr.No. 579101900GR1, 1977.

[49] K. W. Jones and M. L. Dunn. Fatigue crack growth through a residual stress field introduced by plastic beam bending. Fatigue Fract Engng Mater Struct 31, 863875, 2008.

[50] S.R. Daniewicz J.C. Newman Jr. and J. LaRue. Fastran analyses of coupons with residual stresses due to overloads and cold-worked holes. 9th Joint FAA/DoD/NASA Aging Aircraft Conference, 2006.

[51] H.C. Choi and J.H. Song. Finite element analysis of closure behaviour of fatigue cracks in residual stress fields. Fatigue Fract. Engng Mater. Stnrct. Vol. 18, No. 1, pp. 105-117, 1995.

[52] G. Glinka. Effect of residual stresses on fatigue crack growth in steel weldments under constant and variable amplitude loads. Fracture mechanics, ASTM STP 667, 1979 pp. 198-214.

[53] Y.C. Lam. The effect of residual stress and its resdistribution on fatigue crack growth. Theoretical and Applied Fracture Mechanics 12 (1989) 59-66.

[54] M. Beghini and L. Bertini. Fatigue crack propagation through residual stress fields with closure phenomena. Engineering fracture mechanics, Vol.36, pp 379-387, 1990.

[55] H.F. Bueckner. The propagation of cracks and the energy of elastic deformation. Trans. ASME 80, 12251229, 1958.

[56] M.D. Heaton. On the calculation of stress intensity factors due to thermal and residual stress fields. CEGB Research Report NW/SSD/RR/158., 1976.

[57] X. Wu and R. Carlsson. Weight functions and stress intensity factor solutions. Pergamon Press, Oxford, (1991).

[58] James R. Rice. Some notes on elastic crack-tip stress fields. int. J. Solids Structures, 1972, Vol. 8. pp. 751 to 758. Pergamon Press.

[59] K.W. Jones. Predicting fatigue crack growth through residual stress fields. Doctoral Thesis, University of Colorado, Department of mechanical Engineering, 2009.

[60] T. Ghidini and C. Dalle Donne. Fatigue crack propagation assessment based on residual stresses obtained through cut-compliance technique. 2006 Blackwell Publishing Ltd. Fatigue Fract Engng Mater Struct 30, 214222.

[61] W. Jones and M.L. Dunn. Predicting fatiuge crack growth from a preyielded hole. International Journal of Fatigue 31 (2009) 223-230.

[62] J.M. de Freitas F.J. Romeiro, C.A Domingos. Measurement of fatigue crack closure for negative stress ratio. ASTM STP1343 pp321-336, 1999.

[63] P. Bompard S. Pommier, C. Prioul. Influence of a negative r ratio on the creep fatigue behaviour of the n18 nickel base superalloy. Fatigue Fract Eng Mater Struct, 20 (1) (1997), pp. 93107.

[64] S. Suruga Y.Z. Itoh and H. Kashiwaya. Prediction of fatigue crack growth rate in welding residual stress field. Engineering fracture mechanics Vol. 33, No. 3, pp. 397-407, 1989.

[65] A. Todoroki and H. Kobayashi. Prediction on fatigue crack growth rate in residual stress fields. Engineering Materials Vols. 51-52 (1991) pp 367-372.

[66] Yazhi Li Liang Wang and Hong Su. On the stress intensity factor of cracks in residual stress field. Key Engineering Materials Vols. 353-358 (2007) pp 1078-1081.

[67] A.F. Liu. Crack growth at a pre-yielded hole. Journal of engineering materials and technology, Transactions of ASME, Vol.104, 1982, pp. 153-154.

[68] J. LaRue. The effect of residual stresses on fatigue crack growth. M.S. Thesis, Mississippi State University, 2005.

[69] R.C. McClung and H. Sehitoglu. On the finite element analysis of fatigue crack closure-2. numerical results. Engineering Fracrure Mechanics Vol. 33, No. 2, pp. 253-272, 1989.

[70] H. Swenson P. Pagliaro, M.B. Prime and B. Zuccarello. G. johnson. Ph.D thesis, University of Manchester, Faculty of Engineering and Physical Science, UK, 2008.

[71] A. T. Fry F. A. Kandil, J. D. Lord and P. V. Grant. A review of residual stress measurement methods, a guide to technique selection. NPL Report MATC(A)O4, 2001.

[72] Michael R. Hill1 Matthew J. Lee. Effect of strain gage length when determining residual stress by slitting. Journal of Engineering Materials and Technology JANUARY 2007, Vol. 129.

[73] D. Ritchie and R.H. Leggatt. The measurement of the distribution of residual stresses through the thickness of a welded joint. Strain may 1987, pp.61-70.

[74] M.J. Lee and M.R. Hill. Intralaboratory repeatability of residual stress determined by the slitting method. Experimental Mechanics (2007) 47:745752.

[75] C. Lee M. Dutton N.A. Hoult, W. A. Take. Experimental accuracy of two dimensional strain measurements using dic. Engineering structures 46 (2013) 718-726.

[76] K.Y. Benyounis A.G. Olabi N.S. Rossini, M. Dassisti. Methods of measuring residual stresses in components. Materials and Design 35 (2012) 572588.

[77] D. J. Smith D. Stefanescu, C. E. Truman and P. S. Whiteheadi. Improvements in residual stress measurement by the incremental centre hole drilling technique. Experimental Mechanics (2006) 46: 417427.

[78] R. Oettel. The determination of uncertainties in residual stress measurement. Standards Measurement and Testing Project No. SMT4-CT97-2165, 2000.

[79] G.S. Schajer. Hole-drilling residual stress measurements at 75: Origins, advances, opportunities. Experimental Mechanics (2010) 50:245253.

[80] E Kingston D George and D J Smith. Measurement of through-thickness stresses using small holes. The Journal of Strain Analysis for Engineering Design 2002 37: 125.

[81] David Smithi Sayeed Hossain, Chris Truman. Benchmark measurement of residual stresses in a 7449 aluminium alloy using deep-hole and incremental centre-hole drilling methods. Engineering Applications of Residual Stress, Volume 8, 2011.

[82] C.E. Truman D.J. Smith A.H. Mahmoudi, S. Hossain and M.J. Pavier. A new procedure to measure near yield residual stresses using the deep hole drilling technique. Experimental Mechanics (2009) 49:595604.

[83] M.B. Prime. Cross-sectional mapping of residual stresses by measuring the surface contour after a cut. Journal of Engineering Materials and Technology Volume 123 April 2001 pp. 162-168.

[84] Michael E. Fitzpatrick Ying Zhang and Lyndon Edwards. Measurement of the residual stresses around a cold expanded hole in an en8 steel plate using the contour method. Materials Science Forum Vols. 404-407 (2002) pp 527-534.

[85] A.M. Dias J.P. Nobre and M. Kornmeier. An empirical methodology to estimate a local yield stress in work-hardened surface layers. Society for experimental mechanics, VoL 44, No. 1, February 2004.

[86] John M. Edwards Darren J. Hughes Peter J. Webster Michael B Primwe, Robert J. Sebring. Laser surface-contouring and spline data-smoothing for residual-stress measurement. Experimental Mechanics Volume 44, Number 2, April 2004, pp. 176-184.

[87] H. Swenson P. Pagliaro, M.B. Prime and B. Zuccarello. Measuring multiple residual-stress components using the contour method and multiple cuts. Experimental Mechanics (2010) 50:187194.

[88] P. S. Prevey. X-ray diffraction residual stress techniques. Metals Handbook, 10, Metals Park, OH: American Society for Metals, pp. 380-392, 1986.

[89] KU Leuven. X-ray diffraction bruker d8 discover. http://fys.kuleuven.be/iks/nvsf/experimental-facilities/x-ray-diffraction-2013-bruker-d8-discover, accessed on 12-2-2013, 2010.

[90] F. Convert M. Francois and S. Branchu. French round-robin test of x-ray stress determination on a shot-peened steel. Experimental mechanics, VoL 40, No. 4, December 2000 pp.361-368.

[91] Z. Chen H. Lombard D.G. Hattingh D. Asquith J.R. Yates M.N. James, D.J. Hughes and P.J. Webster. Residual stresses and fatigue performance. Engineering Failure Analysis 14 (2007) 384395.

[92] L. Wagner. Mechanical surface treatments on titanium, aluminum and magnesium alloys. Materials Science and Engineering A263 (1999) 210-216.

[93] H-J. Schindler and P. Bertschinger. Some steps towards automation of the crack compliance method to measure residual stress distributions. Proceedings of the 5th International Conference on Residual Stress, 1997.

[94] M.B. Prime. Residual stresses measured in quenched hsla-100 steel plate. ResProceedings of the 2005

SEM Annual Conference and Exposition on Experimental and Applied Mechanics June 7-9, 2005.

[95] R. Stone. Processing effects on residual stress. Unpublished, Unknown.

[96] Mark R. Daymond Terri G. Abeln Michael B. Prime, Partha Rangaswamy. Several methods applied to measuring residual stress in a known specimen. Submitted to: society for experimental mechanics, Spring conference, 1998.

[97] T. Ozdemir and L. Edwards. Measurement of the three-dimensional residual stress distribution around split-sleeve cold-expanded holes. The Journal of Strain Analysis for Engineering Design 1996 31: 413.

[98] Liu Jun Liu Yongshou, Shao Xiaojun and Yue Zhufeng. Finite element method and experimental investigation on the residual stress fields and fatigue performance of cold expansion hole. Materials and Design 31 (2010) 12081215.

[99] ASTM International. Standard test method of tension testing of metallic materials at room temperature. ASTM test standard E8M-04, 2004.

[100] ASTM International. Standard test method of compression testing of metallic materials at room temperature. ASTM test standard E9-89a(00), 1989.

[101] Dilermando N. Travessa Katia R. Cardoso Kassim S. Al-Rubaie, Marcio A. Del Grande. Effect of pre-strain on the fatigue life of 7050-t7451 aluminium alloy. Materials Science and Engineering A 464 (2007) 141150.

[102] Joel Schubbe. Fatigue crack growth in thick plate 7050 aluminum. 25th ICAF Symposium Rotterdam, 2729 May 2009.

[103] ASTM International. Standard test method for measurement of fatigue crack growth rates. ASTM test standard E647, 2000.

[104] K. Sadananda A.K. Vasudevan and K. Rajan. Role of microstructures on the growth of long fatigue cracks. Int. J. Fatigue Vol. 19, Supp. No. 1, pp. S151S159, 1997.

[105] Michael B. Prime and Alan L. Kastengren. The contour method cutting assumption: Error minimization and correction. Experimental and Applied Mechanics, Volume 6, T. Proulx, ed., Springer New York, pp. 233-250, 2010.

[106] George R. Irwin H. Tada, Paul C. Paris. The stress analysis of cracks handbook. American Society of Mechanical Engineers; 3 Sub edition (January 1, 2000), ISBN-10: 0791801535.

[107] V. Papaspyropoulos J. Ahmad and A.T. Hopper. Weight function for a single edge cracked geometry with clamped ends. International Journal of Fracture 72:145-158, 1995.

[108] D.A. Johnson R. John, S.G. Kaldon and D. Coker. Weight function for a single edge cracked geometry with clamped ends. International Journal of Fracture 72:145-158, 1995.

[109] R. John and B. Rigling. Effect of height to width ratio on k and cmod solutions for a single edge cracked geometry with clamped ends. Engineering Fracture Mechanics Vol. 60, No. 2, pp. 147156, 1998.

[110] C.C. Aydiner and M.B. Prime. Three-dimensional constraint effects on the slitting method for measuring residual stress. intended for Journal of Engineering Materials and Technology, 2013, Vol. 135.

[111] R. Branco and F.V. Antunes. Finite element modelling and analysis of crack shape evolution in mode-i fatigue middle cracked tension specimens. Engineering Fracture Mechanics 75 (2008) 30203037.

[112] N. Bridgford R. Jones M.D. Kuruppu, J.F. Williams and D.C. Stouffer. Constitutive modelling of the elastic-plastic behaviour of 7050-t7451 aluminium alloy. JOURNAL OF STRAIN ANALYSIS VOL 27 NO 2 1992.

[113] J. F. Durodola G. Urriolagoitia-Sosa and N. A. Fellows. Determination of residual stress in beams under bauschinger effect using surface strain measurements. Strain (2003) 39, 177185.

[114] M.J. Lee and M. R. Hill. Erratum: Effect of strain gage length when determining residual stress by slitting. Journal of Engineering Materials and Technology, 2007, 129(1), pp. 143150.

[115] M. Prime. Los alamos national laboratory. email: prime@lanl.gov.

[116] W. Cheng and I. Finnie. Residual stress measurement and the slitting method. ISBN 0-387-37065-X, Springer, USA, 2007.

[117] ASM International. Metals handbook, vol.2-properties and selection: Nonferrous alloys and special-purpose materials 10th ed., 1990.

[118] ASTM International. Standard test method for flexural properties of unreinforced and reinforced plastics and electrical insulation materials by four point bending. ASTM test standard D6272-02, 2002.

[119] M.B. Prime and M.R. Hill. Uncertainty, model error, and order selection for series-expanded, residual-stress inverse solutions. Journal of Engineering Materials and Technology 2006, Volume 128, Number 2, pp. 175-185.